University of Alberta

A Multi-Faceted Study of the Voltage Sensor in Voltage-Gated Potassium Channels

by

Rheanna Monique Sand

A thesis submitted to the Faculty of Graduate Studies and Research
in partial fulfillment of the requirements for the degree of

Doctor of Philosophy

in

Physiology, Cell, and Developmental Biology

Department of Biological Sciences

Spring 2012
Edmonton, Alberta

I would like to dedicate this body of work to my friends and family who walked so patiently beside me on this journey. To my mother Debbie Coulter, for unconditional love and support; to my brothers Blaze, Jarod, and Reese, for the same; to my Grandmother Thelma Chalifoux, for blazing the trail; to the rest of the Coulters, Logans, Morins, and Sands, there are too many of you to mention but I love and thank you all; to my self-made family, Elisha, Holland, Josie, Kate, Marcella, Michelle, and Michelle, for lifting me up when things felt low, and for not letting my head get too big; to my lab family, Warren, Donna, and Tara, for hiring me when I thought all was lost and giving me a future I couldn't have dreamed; to George, Brittany, and Torah, for the incredibly worthwhile distractions.

Most of all, I dedicate this thesis to Jennifer Foster, who stood by me through the best and the worst of it and helped me appreciate every single moment of this educational gauntlet known as graduate school. Partial derivatives or not, my eternal love and humble gratitude are yours.

Abstract

Voltage-gated potassium (K_v) channels regulate the flow of potassium ions across the cell membrane of nerves and muscles. Proper functioning of these and other voltage-gated ion channels is critical for an animal to sense the environment and respond quickly to stimuli. Dysfunctional K_v channels, whether inherited or induced by pharmacological agents, can be the root cause of disease or death. K_v proteins have a voltage sensing domain that physically moves across the cell membrane during activation, but a complete picture of this process is lacking. The work presented in this thesis addressed the structure-function relationships within the voltage sensing domain of K_v channels using three distinct approaches. First, a previously unknown jellyfish K_v channel was sequenced in order to diversify the pool of known channels, which is heavily biased toward mammalian sequences. The voltage-dependent properties of this new channel were compared to those of known, mammalian channels to better understand the processes of voltage-dependent gating. Secondly, a well-studied mammalian channel was altered in a way that allowed for an estimation of the atomic distance between two helices in the voltage sensing domain. Molecular dynamics simulations were used to calculate Gibbs free energy difference between two states, which was compared to experimental data to triangulate the most likely actual distance between the S3 and S4 helices. Lastly, several experiments were undertaken to locate the pharmacological receptor site on K_v channels for 6-bromo-2-mercaptotryptamine or BrMT. This gastropod toxin is a modulator of K_v channels that interferes with the gating process. Attempts to locate that binding site through mutagenesis and electrophysiological assay were not conclusive. In summary, the atypical behavior of the novel jellyfish channel demonstrated the utility of isolating and characterizing K_v sequences from basally-branching organisms; the comparison of free energy from molecular dynamics with that

of real-world data allowed us to estimate atomic distances in a K_v channel; and BrMT may represent a new mechanistic class of K_v channel blocker but more work is needed to determine the binding site.

Acknowledgements

I would like to acknowledge the following people who directly or indirectly assisted me in the completion of this work: Dr. Warren Gallin, Dr. Dennis Hall, Dr. Declan Ali, Dr. Peter Light, Donna Atherton, Dr. Tara Klassen, Dr. Andy Spencer, Ron Koss, Patrick Boutet, Carla Morgan, Alex Smith, Nazlee Sharmin, Brit Trogen, Daniel Brewster, Jeremy Jackman, Eric Pelletier, Blake Lazurko, Trevor Fay, Jeff Johnston, the staff at Bamfield Marine Science Center, and the staff in the University of Alberta Biological Sciences Department and Aquatics Facility.

Table of Contents

List of Tables

List of Figures

Figure 4-12 Mouse $K_v1.2$ F302L mutant channels are blocked by 100 µM BrMT. (p. 158)

List of Symbols and Abbreviations

Δ	change in
Δ23	first 23 amino acids removed (inactivation-removed)
ΔG	change in Gibbs free energy between closed and open states
τ	time constant
4AP	4-aminopyridine
AP	action potential
b	Boltzmann slope factor
BrMT	6-bromo-2-mercaptotryptamine
Ca_v	voltage-gated calcium channel
cDNA	reverse-transcribed deoxyribonucleic acid
DIDS	diisothiocyanatostilbene-2,2′-disulfonic acid
DMSO	dimethyl sulfoxide
I	current
IC_{50}	half inhibitory concentration
IUPHAR	International Union of Basic and Clinical Pharmacology
G	conductance
G-V	conductance-voltage
K^+	potassium ion
K_v	voltage-gated potassium channel
Na_v	voltage-gated sodium channel
ND96	*Xenopus laevis* physiological saline
NVP	moles, volume, pressure (isothermic-isobaric ensemble in MD)
NVT	moles, volume, temperature (canonical ensemble in MD)
MBM	modified Barth's medium
MD	molecular dynamics

mRNA	messenger ribonucleic acid
ORF	open reading frame
PCR	polymerase chain reaction
PD	pore domain
PDB	Protein Data Bank
QT	Q to T time interval during the heart action potential
S4	fourth transmembrane helix in K_v channels (voltage sensor)
T1	tetramerization domain
TEA	tetraethylammonium
TEV	tobacco etch virus (protease)
V	voltage (across the membrane)
V_{50}	half activation voltage
VKCDB	Voltage-gated Potassium Channel Database
V_{rev}	potassium reversal potential
VSD	voltage sensing domain

Chapter 1: Introduction

Animals stand apart from plants and fungi in their ability to sense and quickly respond to changes in the environment. This ability hinges on the presence of specialized excitable cells that generate electrical and chemical signals, such as neurons and muscle cells. Cellular excitability, in turn, depends on a wide array of membrane proteins, but the best characterized are voltage-gated ion channels (Hille, 2001). Of this group, voltage-gated calcium (Ca_v), sodium (Na_v), and potassium (K_v) channels play the most prominent roles in initiating and propagating action potentials. These channels share two basic functions: to sense voltage changes across the cell membrane, and selectively conduct calcium, sodium, or potassium ions in response to those changes. It was first shown in the squid giant axon that during an action potential Na_v channels open, allowing sodium ions to rush into the cell. This process depolarizes the electrical potential across the cell membrane, which causes K_v channels to open and conduct potassium ions out of the cell, thereby restoring the negative membrane potential (Hodgkin and Huxley, 1952).

Owing to their relative simplicity, collecting structural and functional information on K_v channels has been experimentally tractable compared to Na_v and Ca_v channels. Na_v and Ca_v channels contain a total of 24 transmembrane helices, grouped into four homologous domains of six helices each, whereas K_v channels are assembled from four separate subunits of six helices (Figure 1-1). Thus, K_v proteins are easier to clone and manipulate, and the wealth of knowledge that

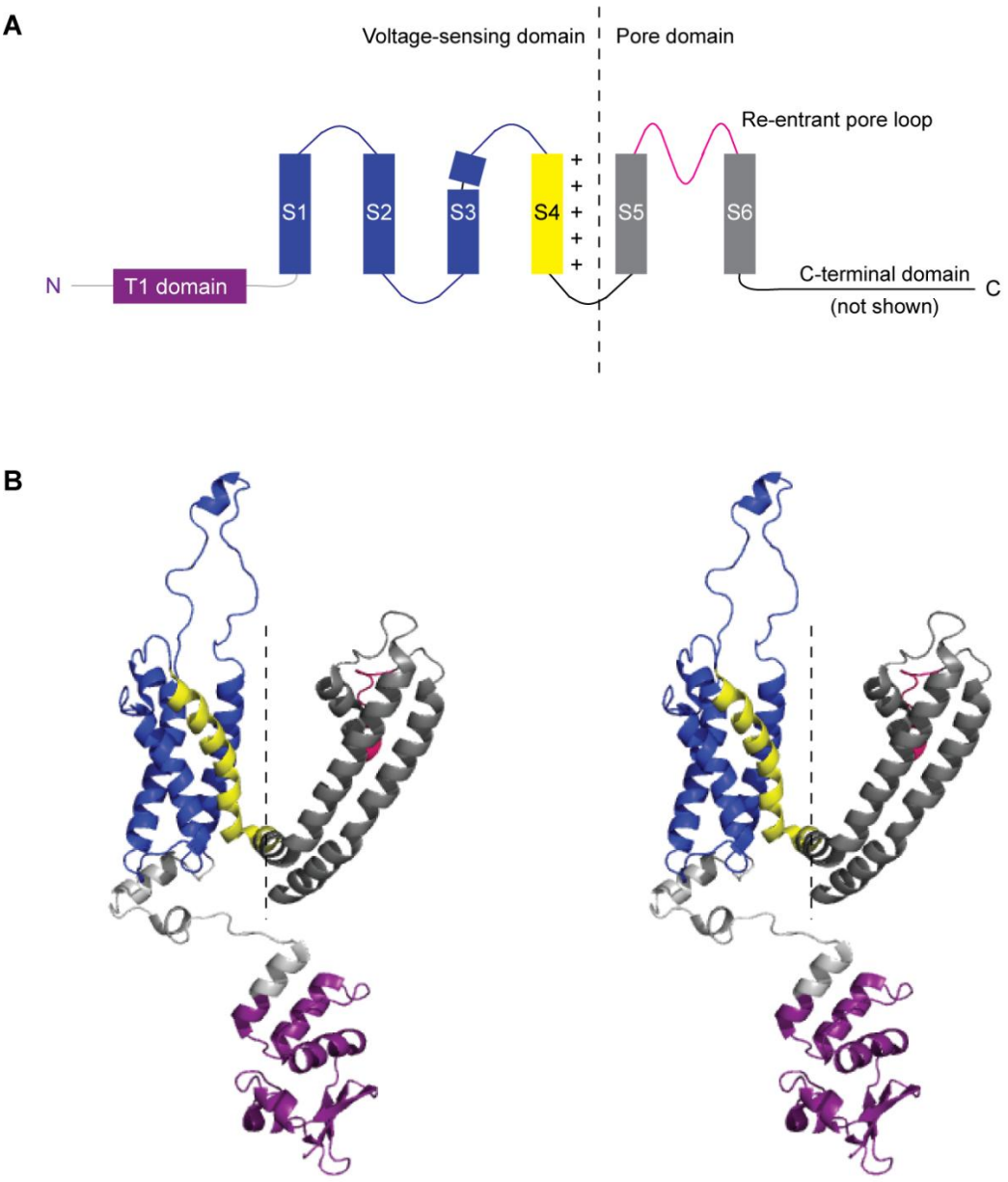

Figure 1-1. Structure of one K_v subunit. A, Schematic of a single K_v transcript, showing an intracellular N-terminus which sometimes contains an inactivation particle (not shown), a tetramerization (T1) domain, six trans-membrane helices (S1 through S6) and their linkers, a re-entrant loop between S5 and S6 that forms a filter region highly selective to dehydrated K^+ ions, and an intracellular C-terminus. Functionally, K_v subunits can be broken down into the voltage-sensing domain and the pore domain. The S4 helix carries four to seven positively charged residues at every third position, providing the primary electromotive force that drives pore opening and closing in response to changing membrane electrical potentials. B, Stereo cartoon representation of the schematic in panel A. Dotted line represents a rough division between functional domains. The 3-D model shown is that of rat Kv1.2 (3LUT; Chen et al., 2010). Molecular model images were made in PyMOL.

exists about voltage-gated proteins has come from work on a few model channels, like KcsA from the bacterium *Streptomyces lividans,* Shaker from the fruit fly *Drosophila melanogaster*, and K_v1.2 from the mouse *Mus musculus*. While these model channels are from diverse organisms, the sequencing of new K_v channels has largely been focused on human, mouse, and rat channels, as can be evidenced by browsing through ion channel databases like VKCDB (Gallin and Boutet, 2011) or the IUPHAR compendium of receptors and ion channels (Harmar et al., 2009).

K_v subunits range from about 400 to 800 amino acids in length and have specialized regions that contribute to proper assembly, to voltage sensing, and to pore opening and closing (Figure 1-1). K_v subunits are also commonly divided into two functional domains, the voltage-sensing domain (VSD), consisting of transmembrane helices S1 through S4 plus associated linkers, and the pore domain made up of S5 through S6. Four pore domains interlock centrally to create a functional pore while the VSDs reside on the periphery, in contact with membrane lipids but structurally independently of each other (Figure 1-2). Within the VSD, the S4 helix carries four to seven positively charged residues at every third position, and the four most extracellular are the "gating charges" that actively sense voltage changes and move some physical distance through the membrane electric field (Aggarwal and MacKinnon, 1996; Larsson et al., 1996; Seoh et al., 1996). The activation of all four VSDs ultimately causes the intracellular gates to open and K^+ to flow through the pore.

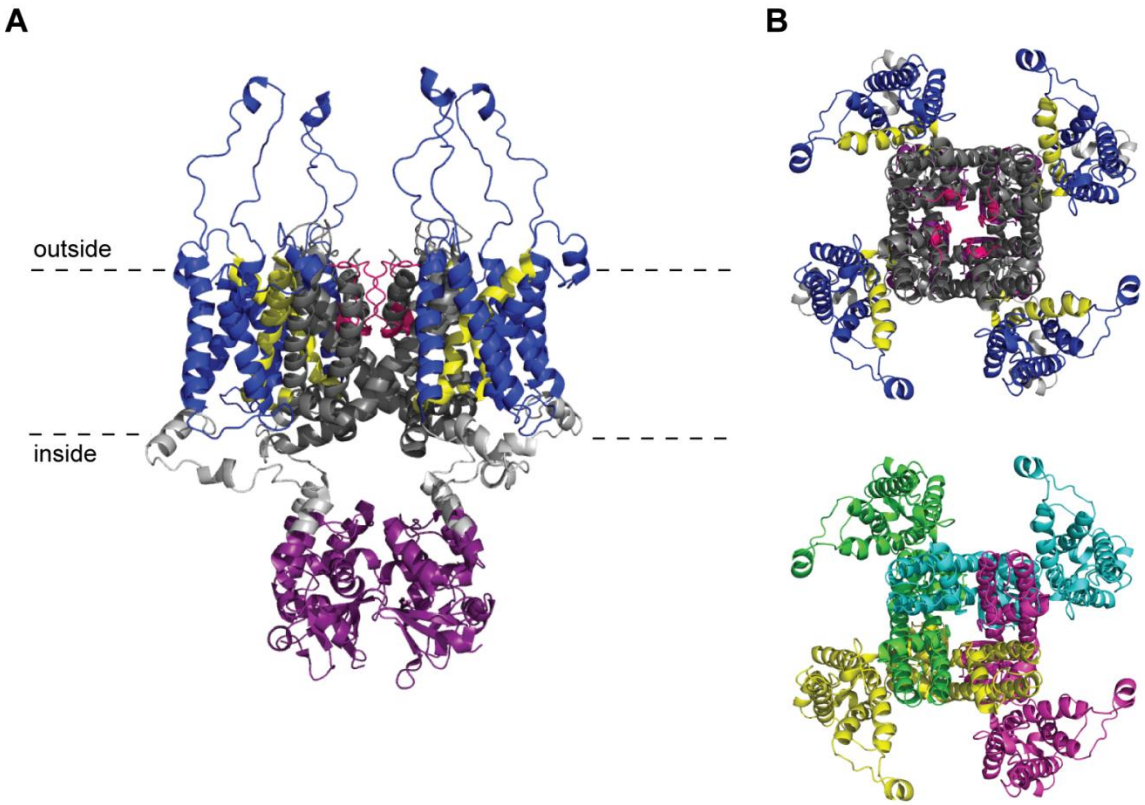

Figure 1-2. Presumed structure of a K_v tetramer. A, The rat K_v1.2 crystal structure (3LUT; Chen et al., 2010) as viewed from the side, with the extracellular environment up. Only the backbone is shown, and in ribbon representation. Each subunit has the same colour scheme, and it is the same as that presented in Figure 1-1. The S4 helix, or voltage sensor, is depicted in yellow. Dashed lines indicate the approximate boundaries of the lipid bilayer in a membrane-embedded channel. B, The rat K_v1.2 crystal structure rotated to peer down through the pore into the cell. The upper image is shaded the same as in panel A, and highlights the central assembly of the pore domains (grey) compared to the isolated VSDs (blue/yellow). The lower image shows each subunit shaded in a different colour to illustrate the interlocking of adjacent subunits in a counter-clockwise fashion. Molecular model images were made in PyMOL.

The mechanism by which K_v channels discriminately conduct ions through the pore domain is fairly established (Cordero-Morales et al., 2006; Gouaux and MacKinnon, 2005) although some debate still lingers on the precise origin of ion selectivity (Nimigean and Allen, 2011). In contrast, defining the structural rearrangements that occur in the VSD has been more challenging (Swartz, 2004; Tombola et al., 2006). This is to be expected in a region of the protein that responds dynamically to membrane voltage, which is itself influenced by the flow of ions across the membrane. The voltage clamp method (Cole and Moore, 1960; Marmont, 1949) solves one of these issues; holding cells at a constant membrane potential gives the channels time to reach equilibrium and allows the parameters of channel opening and closing to be determined at different voltages, and it is clear from voltage clamp experiments that voltage-dependent gating is a complex process that cannot be explained by a simple two state, open-and-closed model. Kinetic analysis of *D. melanogaster* Shaker currents suggested that upon membrane depolarization, at minimum each K_v subunit undergoes two voltage-dependent rearrangements to become fully activated (Bezanilla et al., 1994; Schoppa and Sigworth, 1998b; Zagotta et al., 1994a). Once all four subunits are activated, the channel pore opens in a final, concerted step (Ledwell and Aldrich, 1999; Yifrach and MacKinnon, 2002) producing a fast flow of ions into or out of the cell, down the electrochemical gradient of potassium. Allosteric models, like ones based on the Monod-Wyman-Changeax model, allow for channels to open with any number of subunits activated, including none, resulting in at least ten kinetically distinct states (Klemic et al., 1998). Refining these kinetic models and

relating them to actual structures within the VSD represents one of the major frontiers in K_v research.

The broad goal of the work presented here is to increase our knowledge about voltage-dependent gating in K_v channels through three distinct approaches. First, by characterizing new, unique invertebrate K_v proteins and comparing them to known channels; second, by comparing the free energy of molecular dynamics simulations to that derived from voltage clamp recordings of a mutated model channel; and third, by characterizing the interaction site of a K_v channel blocker that interferes with the voltage sensing domain. Utilizing voltage clamp analysis as the primary tool, these strategies are employed in Chapters 2, 3, and 4 of this thesis. In addition to providing a more complete view of K_v channel function, investigating the molecular determinants of voltage-dependent gating would shed light on the function of other proteins with voltage sensors, like Na_v and Ca_v channels, or the voltage-sensitive phosphatase Ci-VSP, from the ascidian *Ciona intestinalis* (Iwasaki et al., 2008; Villalba-Galea et al., 2009). Revealing the dynamics of the VSD would also serve to benefit medical research on inherited pathologies related to K_v channel dysfunction, like neonatal epilepsy, Long QT syndrome, or hypokaelemic periodic paralysis (Ashcroft, 2006; Vernino, 2007).

In studying K_v channels, the comparative approach is simple and informative, but remains underutilized as a research tool. As mentioned, the vast majority of K_v channels that have been isolated, sequenced, and functionally characterized belong to mammals, typically human, rat, and mouse, but the process of voltage-

dependent gating has been finely tuned across the animal kingdom through the evolution of a myriad of K_v subtypes and accessory subunits (Gallin and Boutet, 2011). Consequently, a thorough understanding of the VSD must take advantage of and explain the variation seen in the natural world. During millions of years of evolution, mutations in certain regions of the protein were passed on to the next generation because they provided some adaptive advantage or through genetic drift. Mutations that cause the channel to be non-functional or dysfunctional, however, would render the individual unable to survive or reproduce. Therefore, seeking out K_v sequences from wide-ranging branches on the evolutionary tree is one way in which to illuminate regions and positions of the protein that are crucial for function, versus those that are not. This concept forms the basis for the work presented in the second chapter.

The hydrozoan jellyfish *Polyorchis penicillatus*, like other members of the Phylum Cnidaria, lacks a central nervous system, but among other things, uses a diffuse nerve net to transmit photosensory information from ocelli in the bell margin to the swimming muscles lining the bell (Spencer, 1978; Spencer, 1979). Phylum Cnidaria is positioned far from mammals on the evolutionary tree, and is classified as a sister group to all bilaterally symmetrical animals. Yet, of the four main subfamilies of K_v, the K_v1 through K_v4 channels (also known as Shak, Shab, Shaw, and Shal channels in the *Drosophila melanogaster* gene nomenclature), the jellyfish *P. penicillatus* contains at least two K_v1 channels, jShak1 and jShak2 (Jegla et al., 1995) and a K_v4 with an associated gamma subunit (Jegla and Salkoff, 1997), plus has several positive leads from a preliminary transcriptome

analysis (W. Gallin, unpublished). The molecular cloning and expression of the first K_v3-type channel from the Phylum Cnidaria, jShaw1, is described in the second chapter with a side-by-side functional comparison with known mouse channels K_v3.1b and K_v3.2 (Sand et al., 2011). The unusual characteristics of channels isolated from *P. penicillatus* (Grigoriev et al., 1997; Grigoriev et al., 1999; Klassen et al., 2008a) and other marine invertebrates (Bouchard et al., 2006; Klassen et al., 2006; Klassen et al., 2008b) highlight the utility of continuing to sequence new channels from basally branching organisms.

Measuring populations of channels in real time under voltage clamp is the foundation of our functional knowledge of K_v and other voltage-gated ion channels. Combining voltage clamp electrophysiology with molecular genetics techniques, which permit channels to be altered at the gene level through site-directed mutagenesis, illuminates the role of specific residues in determining voltage-dependent properties. Such structure-function analyses uncovered many core elements of ion channel architecture, even before the development of structural techniques like x-ray diffraction from crystallized ion channel proteins. Once these structural techniques were utilized, crystallographic data revealed angstrom-level information on virtually complete K_v channels (Chen et al., 2010; Jiang et al., 2003a; Long et al., 2005; Long et al., 2007), confirming the general membrane topology and quaternary arrangement of K_v subunits suggested by previous structure-function studies.

While these 3-dimensional coordinates provide our best estimate yet of K_v structure, the technical limitations of crystallizing large, membrane-bound proteins like K_v channels may lead to biases in some aspects of the analysis. For example, channels that can be purified will necessarily be removed from the membrane, and therefore any information with respect to lipid interactions (Butterwick and MacKinnon, 2010; Hong and Miller, 2000; Lee et al., 2005) is lost. Furthermore, channels that undergo crystallization experience dense packing conditions with unnatural contacts between intra- and extracellular domains, reducing the likelihood that crystal structures represent a stable *in vivo* conformation. Therefore, K_v crystal structures should be considered a backbone on which to base experimental predictions and computational analyses, and should be complemented by functional studies whenever possible. The third chapter of this thesis is a functional study that attempts to assess the current models of VSD structure. Specifically, the atomic distance between the S3 and S4 helices during activation was estimated using voltage clamp recordings and theoretical molecular dynamics simulations. This approach provides a view of K_v channel structure that is not biased by the aforementioned issues with data collected from protein crystals.

Investigating the distance between S3 and S4 sheds light on the various structural models of voltage-dependent gating, which have coalesced into three main types, based on their predictions of how the S4 helix moves in relation to surrounding helices (Catterall, 2010; Swartz, 2004). Generally agreed upon is the counter-clockwise arrangement of the four helices in the activated VSD (Figure 1-3), but

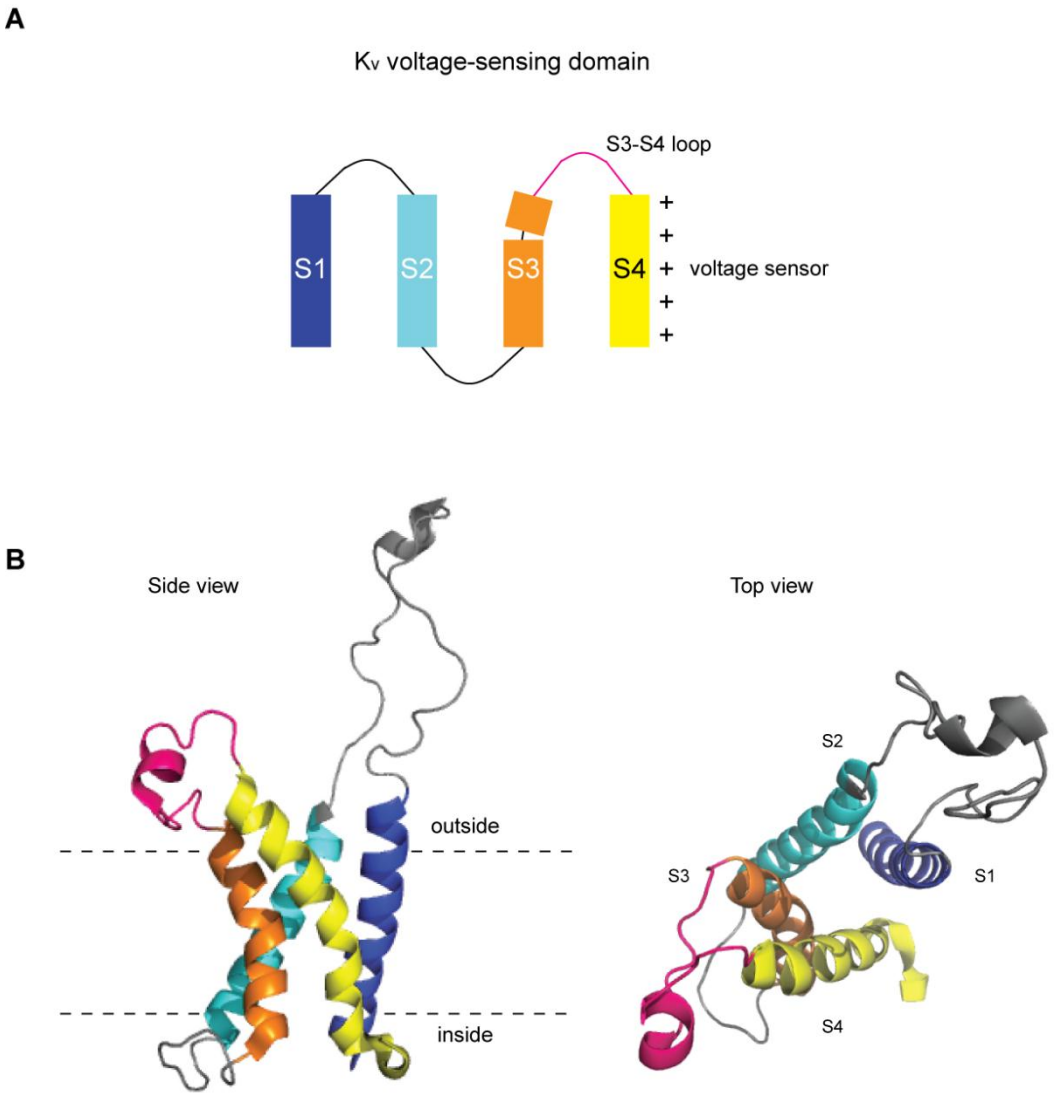

Figure 1-3. The voltage sensing domain of K_v channels. A, Schematic of the four helices that make up the voltage sensing domain. The S4 carries four to seven positively charged residues and senses changes in the normally negative membrane potential, moving from a resting state to an activated state. Activation of all four voltage sensors leads to channel opening. The nature of the resting-to-activated transitions (or closed-to-open transitions when considering whole channels) is not known. B, Voltage sensing domain of crystallized rat $K_v1.2$ (3LUT; Chen et al., 2010), shown in side view (left) and top view (right) in ribbon with no side chains. Helices S1 through S4 are shaded as in the schematic drawing. In this 3-D model, the VSD helices are in a transmembrane orientation and bundled together in a counter-clockwise direction going from S1 to S4. This structure is presumed to represent the activated state of the VSD since the crystallized rat $K_v1.2$ channels had an open pore. Molecular model images were made in PyMOL.

what is not agreed upon is how they arrive at that conformation. Each of the three main structural models addresses the problem of moving a large amount of electrical charge through the hydrophobic lipid bilayer in different ways, and each has supporting functional evidence.

The paddle model posits that helices S3 and S4 form a voltage sensing "paddle motif" that is exposed to the lipid bilayer and lies parallel to the membrane in the resting conformation (Figure 1-4A). During activation, the paddle motif translocates as a unit through the membrane and reaches a transmembrane orientation. This scheme was developed after the first crystal structure of KvAP was released (Jiang et al., 2003a). This model showed the S3 and S4 helices to be in a position that would place them parallel to the membrane *in vivo*. Experiments with biotin and avidin, agents that bind with extremely high affinity within a distance of 1 nm, also pointed to a near intracellular position of S4 in the resting conformation (Jiang et al., 2003b). However, there were early signs that this structure of KvAP was distorted by the co-crystallized antibody fragment. The most obvious inconsistency was that the voltage sensors were in a supposedly resting position, but the pore was open. K_v channels have extremely low open probabilities ($\sim 10^{-9}$) when the voltage sensors are not activated (Soler-Llavina et al., 2003). The S1-S2 linker was also shown to be extracellular in functional studies, but was not in the KvAP structure, and the packing of helices in the voltage sensing domain was not as predicted (Hong and Miller, 2000; Li-Smerin et al., 2000). Later, more functional evidence came to light that refuted the paddle

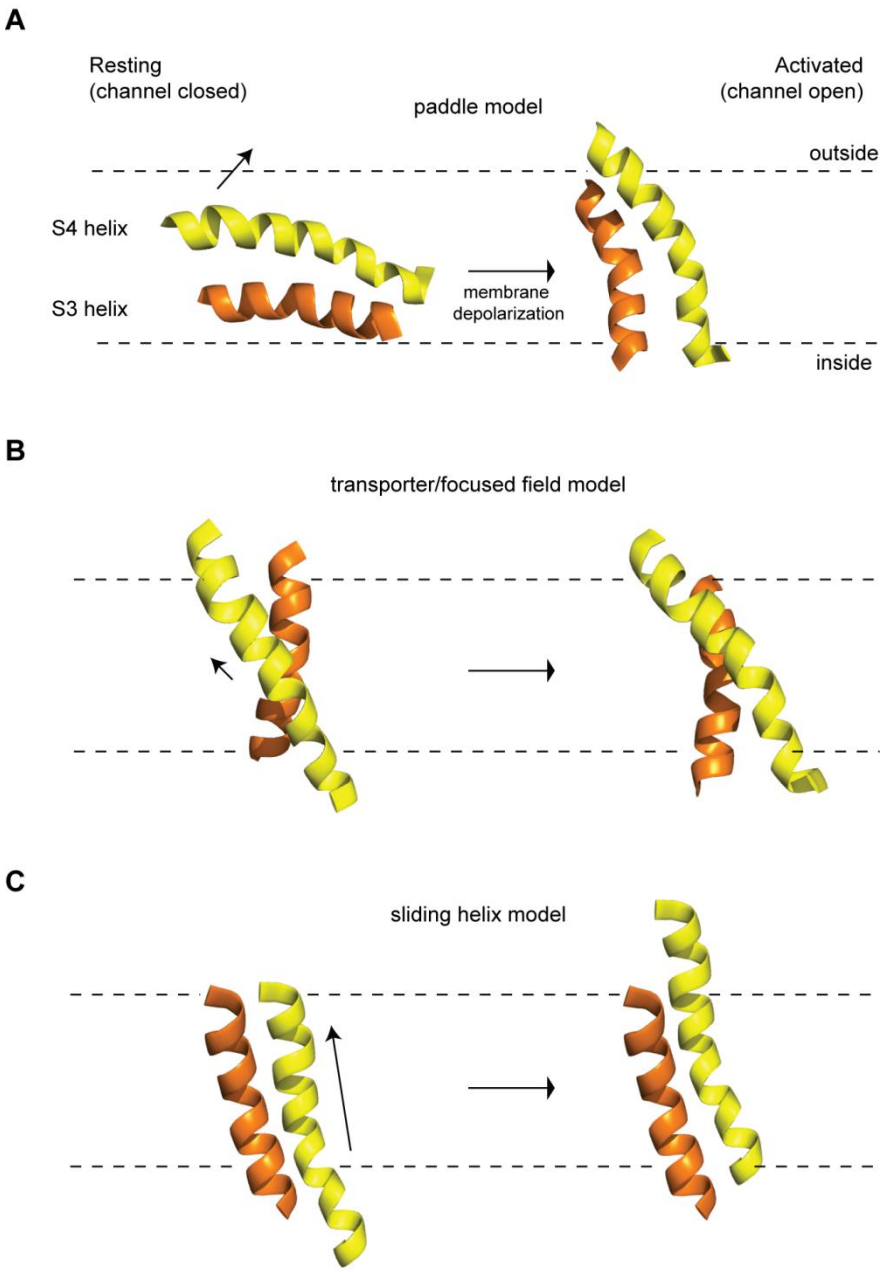

Figure 1-4. The three generalized structural models of voltage-dependent gating in K_v channels. Only the S3 and S4 helices are shown for simplicity. A, The paddle model of gating supports a large degree of motion of S4 through the bilayer, which is locked to S3 to form the so-called "paddle motif." At rest, the paddle is accessible from the intracellular compartment. Fully activated, the paddle adopts a transmembrane orientation. B, The transporter model predicts a very modest upward motion of the S4 helix, and is also called the focused field model for the narrowing of the membrane electric field in water-filled crevices between S4 and the surrounding VSD helices. C, The sliding helix model originally saw the S4 moving as a rigid body upward through the membrane, shielded by the other helices in the VSD. In more recent descriptions of the model, the stepwise stabilization of positive gating charges by nearby negative or aromatic residues has become a more of a defining feature.

model. Experiments that placed reactive cysteine residues in S3 and S4 suggested that these helices were near the extracellular surface in resting and activated states (Carter et al., 2004). Also, the spider venom peptide hanatoxin (Swartz and Mackinnon, 1995) was found to bind to the S3-S4 linker and trap it in the resting conformation (Lee et al., 2003; Li-Smerin and Swartz, 2000; Swartz and MacKinnon, 1997). Given the energetic costs of this peptide plunging into the lipid bilayer, these results suggest that the S3-S4 linker is extracellular when the voltage sensors are at rest.

The transporter model, also known as the focused field model, favours the idea that the charged S4 helix only has to travel a small physical distance if the electric field is focused into a narrower region of the bilayer (Figure 1-4B). This scheme predicts that the positively-charged S4 helix does not encounter the lipid bilayer directly, but moves between water-filled crevices and is stabilized by negative charges in surrounding helices. When fluorescence-emitting probes are attached to the N-terminal end of the S4 helix, the emission spectrum suggests that the probe is only exposed to aqueous and not hydrophobic conditions (Cha and Bezanilla, 1997). Unlike the paddle model, the transporter model predicts that the S4 helix sits perpendicular to the plane of the membrane when in the resting and activated states. Mutating two pairs of residues in S4 and S5 of the Shaker channel demonstrated that disulfide and metallic bridges formed between the S4 and S5 of adjacent subunits in the tetramer (Laine et al., 2003). This and other functional evidence suggests (Broomand et al., 2003; Larsson et al., 1996; Seoh et al., 1996) that S4-S5 inter-subunit interactions occur in the resting and activated

conformations, supporting a transmembrane orientation of S4 in both states. Fluorescence resonance energy transfer experiments indicated only a small overall movement, likely tilting or rotation of the S4 helix a total distance less than 5 angstroms (Blunck et al., 2004; Cha et al., 1999). The discovery of a proton pore through the Shaker voltage sensing domain in the resting conformation also supports a transmembrane position for S4 at rest (Starace and Bezanilla, 2004), as well as the "omega current" passed through Shaker channel voltage sensors when the most extracellular basic residue is mutated to histidine (Tombola et al, 2007). A natural omega current was later observed in the flatworm channel NatK_v3.2 (Klassen et al., 2008b), lending further credence to the transporter or focused field model of gating.

The third proposed mechanism for voltage sensing is the sliding helix model (Catterall, 1986), also called the helical screw model (Guy and Seetharamulu, 1986). In this paradigm, the S4 helix moves upward as a rigid body, stabilized by negative charges in nearby S2 and S3 (Figure 1-4C). This model has been updated to reflect the findings that the middle portion of the S4 helix may be in an extended 3_{10} helical conformation (Khalili-Araghi et al., 2010). The screw-like motion would be restricted to the ends of the S4 helix, with the positive residues stretching out in the center to contact the stabilizing residues in S2 and S3 (Catterall, 2010). The sliding helix model has been recently supported by the discovery of a charge transfer center in S3 which provides a stable interaction point for the positive charges on S4 as they "slide" from the intracellular to extracellular environment (Tao et al., 2010). Relative to nearby helices, S4 is

predicted to move more in this model than in the other two, although there is a great deal of overlap between this and the transporter/focused field model.

In light of these three structural models of voltage sensing, examining the atomic distance between S3 and S4 in the resting and active conformations is a way to distinguish which one more accurately describes the true behaviour of the VSD in membrane-bound channels. If the data suggests that the helices do not move relative to each other, this would support the paddle model. On the other hand, a large degree of relative motion between the two helices would support the helical screw model, while the transporter model would lie somewhere in between. Chapter 3 of this thesis describes the estimation of this distance through a free energy comparison stemming from electrophysiological data and molecular dynamic simulations on versions of mouse $K_v1.2$ that had been mutated in the S3-S4 linker. The data produced by this novel method suggested a 1nm, or 10 angstrom movement between the two helices in mutated channels that had favored open states, matching the sliding helix model more closely than the transporter or paddle models.

A common way to explore ion channel structure-function relationships is to perturb them with pharmacological agents, typically small peptides or small organic molecules that hinder the passage of potassium ions through the pore. There are agents known to augment channel function, like retigabine (Lange et al., 2009), but the vast majority of molecules that interfere with channel function do so in an inhibitory fashion. Molecules that act by physically occluding the ion

conduction pathway, so-called "pore blockers," have been prolific in mapping the structural features of K_v pore domains (Armstrong, 1971; Mackinnon and Yellen, 1990), and, as previously mentioned, the peptide hanatoxin was useful in uncovering the orientation of the S4 helix at rest, since it binds to the S3-S4 linker while the channel is closed. Apart from hanatoxin and similar "inhibitory cysteine knot" peptides that share the same mode of action, there are few agents known to modify the voltage-sensing machinery. Gambierol is one, and the binding site has been localized to the S5-S6 region (Cuypers et al., 2008; Kopljar et al., 2009). The other is 6-bromo-2-mercaptotryptamine, or BrMT, isolated from the marine snail *Calliostoma canaliculatum* (Kelley et al., 2003). This small molecule has been shown to inhibit members of the K_v1 and K_v4 at an unknown site outside the pore, and to bind to closed channels. This compound slows activation ~10 fold (Kelley et al., 2003) and causes inter-subunit cooperativity in the Shaker channel (Sack and Aldrich, 2006; Sack et al., 2004), suggesting it is binding at the interface of two or more subunits.

Localizing the binding site is necessary to utilize BrMT in structure-function studies on K_v channel voltage sensors. Chapter 4 of this thesis details the testing of three hypothetical binding sites for this gating modifier toxin on mouse $K_v1.2$. The S3-S4 linker was the first putative site, followed by two binding pockets that tethered the S4 of one subunit to the S5 or S6 of the adjacent subunit. The third site was identified by virtually docking BrMT against a model of $K_v1.2$ in the closed state (Pathak et al., 2007). While the binding site was not conclusively

located, more experiments are needed to eliminate the binding site predicted through automated docking.

In the long run, identifying the molecular mode of action of BrMT on K_v1.2 would help validate the current models of the channel in the closed conformation. Finding the site of action on the K_v1 subfamily could also have benefits in medical research, as this is an important group of channels from a pharmacological standpoint. K_v1 channels are commonly found in the central nervous system but are also expressed in immune cells. Improperly functioning K_v1.3 channels can lead to T-cell activation and immune disorders like multiple sclerosis (Rangaraju et al., 2009) and specific blockers of this channel are highly sought for therapeutic use (Schmitz et al., 2005; Wulff and Pennington, 2007). While BrMT is not selective among the K_v1 subfamily, it is the only characterized K_v1 gating modifier, and could be used as a starting point for generating derivatives that may exhibit subtype-specificity. Gating modifiers in general are more suited to be selective because they target a region of the protein that is more variable between channel subtypes. Blockers that target the highly conserved pore, like tetraethylammonium or 4-aminopyridine, often do not discriminate greatly between K_v channels.

The general goal of the research presented in this thesis was to better understand the dynamics that occur in the K_v voltage sensing domain during channel opening. Clearly, voltage-dependent gating is a multi-faceted, intricate process that is best understood using a variety of techniques. The lack of sequences isolated from

non-mammalian organisms obscures the full range of function in the natural world. Here a new jellyfish K_v channel has been sequenced and characterized that behaves much differently than its mammalian counterparts. Regarding the lack of clarity around the positioning of S4 in various states, 3-dimensional crystal structures are informative but functional studies are required for a critical look at these models. Here, K_v channels have been manipulated through molecular, electrophysiological, and computational means, revealing useful information about the voltage sensor and providing meaningful paths forward to continued research in this area. Finally, data presented here will help constrain future attempts to locate the precise receptor site for the only known K_v1 gating modifier to be characterized to date.

Literature Cited

Aggarwal, S. K. and MacKinnon, R. (1996). Contribution of the S4 segment to gating charge in the Shaker K+ channel. *Neuron* **16**, 1169-1177.

Armstrong, C. M. (1971). Interaction of tetraethylammonium ion derivatives with potassium channels of giant axons. *Journal of General Physiology* **58**, 413-437.

Ashcroft, F. M. (2006). From molecule to malady. *Nature* **440**, 440-447.

Bezanilla, F., Perozo, E. and Stefani, E. (1994). Gating of Shaker K+ channels 2. The components of gating currents and a model of channel activation. *Biophysical Journal* **66**, 1011-1021.

Blunck, R., Starace, D. M., Correa, A. M. and Bezanilla, F. (2004). Detecting Rearrangements of Shaker and NaChBac in real-time with fluorescence spectroscopy in patch-clamped mammalian cells. *Biophysical Journal* **86**, 3966-3980.

Bouchard, C., Price, R. B., Moneypenny, C. G., Thompson, L. F., Zillhardt, M., Stalheim, L. and Anderson, P. A. V. (2006). Cloning and functional expression of voltage-gated ion channel subunits from cnidocytes of the Portuguese Man O'War *Physalia physalis*. *Journal of Experimental Biology* **209**, 2979-2989.

Broomand, A., Mannikko, R., Larsson, H. P. and Elinder, F. (2003). Molecular movement of the voltage sensor in a K channel. *Journal of General Physiology* **122**, 741-748.

Butterwick, J. A. and MacKinnon, R. (2010). Solution structure and phospholipid interactions of the isolated voltage-sensor domain from KvAP. *Journal of Molecular Biology* **403**, 591-606.

Carter, A. I., Ketty, V. and Blaustein, R. O. (2004). State-dependent reactivity of cysteines substituted into Shaker's gating module. *Biophysical Journal* **86**, 24A-24A.

Catterall, W. A. (1986). Molecular properties of voltage-sensitive sodium-channels. *Annual Review of Biochemistry* **55**, 953-985.

Catterall, W. A. (2010). Ion channel voltage sensors: structure, function, and pathophysiology. *Neuron* **67**, 915-928.

Cha, A. and Bezanilla, F. (1997). Characterizing voltage-dependent conformational changes in the Shaker K+ channel with fluorescence. *Neuron* **19**, 1127-1140.

Cha, A., Snyder, G. E., Selvin, P. R. and Bezanilla, F. (1999). Atomic scale movement of the voltage-sensing region in a potassium channel measured via spectroscopy. *Nature* **402**, 809-813.

Chen, X. R., Wang, Q. H., Ni, F. Y. and Ma, J. P. (2010). Structure of the full-length Shaker potassium channel Kv1.2 by normal-mode-based X-ray crystallographic refinement. *Proceedings of the National Academy of Sciences of the United States of America* **107**, 11352-11357.

Cole, K. S. and Moore, J. W. (1960). Ionic current measurements in the squid giant axon membrane. *Journal of General Physiology* **44**, 123-167.

Cordero-Morales, J. F., Cuello, L. G., Zhao, Y. X., Jogini, V., Cortes, D. M., Roux, B. and Perozo, E. (2006). Molecular determinants of gating at the potassium-channel selectivity filter. *Nature Structural & Molecular Biology* **13**, 311-318.

Cuypers, E., Abdel-Mottaleb, Y., Kopljar, I., Rainier, J. D., Raes, A. L., Snyders, D. J. and Tytgat, J. (2008). Gambierol, a toxin produced by the dinoflagellate Gambierdiscus toxicus, is a potent blocker of voltage-gated potassium channels. *Toxicon* **51**, 974-983.

Gallin, W. J. and Boutet, P. A. (2011). VKCDB: voltage-gated K(+) channel database updated and upgraded. *Nucleic Acids Research* **39**, D362-D366.

Gouaux, E. and MacKinnon, R. (2005). Principles of selective ion transport in channels and pumps. *Science* **310**, 1461-1465.

Grigoriev, N. G., Spafford, J. D., Gallin, W. J. and Spencer, A. N. (1997). Voltage sensing in jellyfish Shaker K+ channels. *Journal of Experimental Biology* **200**, 2919-2926.

Grigoriev, N. G., Spafford, J. D. and Spencer, A. N. (1999). Modulation of jellyfish potassium channels by external potassium ions. *Journal of Neurophysiology* **82**, 1728-1739.

Guy, H. R. and Seetharamulu, P. (1986). Molecular model of the action potential sodium channel. *Proceedings of the National Academy of Sciences of the United States of America* **83**, 508-512.

Harmar, A., Hills, R., Rosser, E., Jones, M., Buneman, O., Dunbar, D., Greenhill, S., Hale, V., Sharman, J., Bonner, T. et al. (2009). IUPHAR-DB: the IUPHAR database of G protein-coupled receptors and ion channels., vol. 37 (Database Issue), pp. D680-D685: Nucleic Acids Research.

Hille, B. (2001). Ion Channels of Excitable Membranes. Sunderland, MA, USA: Sinauer Associates, Inc.

Hodgkin, A. L. and Huxley, A. F. (1952). A quantitative description of membrane current and its application to conduction and excitation in nerve. *Journal of Physiology-London* **117**, 500-544.

Hong, K. H. and Miller, C. (2000). The lipid-protein interface of a Shaker K+ channel. *Journal of General Physiology* **115**, 51-58.

Iwasaki, H., Murata, Y., Kim, Y. J., Hossain, M. I., Worby, C. A., Dixon, J. E., McCormack, T., Sasaki, T. and Okamura, Y. (2008). A voltage-sensing phosphatase, Ci-VSP, which shares sequence identity with PTEN, dephosphorylates phosphatidylinositol 4,5-bisphosphate. *Proceedings of the National Academy of Sciences of the United States of America* **105**, 7970-7975.

Jegla, T., Grigoriev, N., Gallin, W. J., Salkoff, L. and Spencer, A. N. (1995). Multiple Shaker potassium channels in a primitive metazoan. *Journal of Neuroscience* **15**, 7989-7999.

Jegla, T. and Salkoff, L. (1997). A novel subunit for Shal K+ channels radically alters activation and inactivation. *Journal of Neuroscience* **17**, 32-44.

Jiang, Y. X., Lee, A., Chen, J. Y., Ruta, V., Cadene, M., Chait, B. T. and MacKinnon, R. (2003a). X-ray structure of a voltage-dependent K+ channel. *Nature* **423**, 33-41.

Jiang, Y. X., Ruta, V., Chen, J. Y., Lee, A. and MacKinnon, R. (2003b). The principle of gating charge movement in a voltage-dependent K+ channel. *Nature* **423**, 42-48.

Kelley, W. P., Wolters, A. M., Sack, J. T., Jockusch, R. A., Jurchen, J. C., Williams, E. R., Sweedler, J. V. and Gilly, W. F. (2003). Characterization of a novel gastropod toxin (6-bromo-2-mercaptotryptamine) that inhibits shaker K channel activity. *Journal of Biological Chemistry* **278**, 34934-34942.

Khalili-Araghi, F., Jogini, V., Yarov-Yarovoy, V., Tajkhorshid, E., Roux, B. and Schulten, K. (2010). Calculation of the Gating Charge for the Kv1.2 Voltage-Activated Potassium Channel. *Biophysical Journal* **98**, 2189-2198.

Klassen, T. L., Buckingham, S. D., Atherton, D. M., Dacks, J. B., Gallin, W. J. and Spencer, A. N. (2006). Atypical phenotypes from flatworm Kv3 channels. *Journal of Neurophysiology* **95**, 3035-3046.

Klassen, T. L., O'Mara, M. L., Redstone, M., Spencer, A. N. and Gallin, W. J. (2008a). Non-linear intramolecular interactions and voltage sensitivity of a Kv1 family potassium channel from *Polyorchis penicillatus* (Eschscholtz 1829). *Journal of Experimental Biology* **211**, 3442-3453.

Klassen, T. L., Spencer, A. N. and Gallin, W. J. (2008b). A naturally occurring omega current in a Kv3 family potassium channel from a platyhelminth. *BMC Neuroscience* **9**.

Klemic, K. G., Durand, D. M. and Jones, S. W. (1998). Activation kinetics of the delayed rectifier potassium current of bullfrog sympathetic neurons. *Journal of Neurophysiology* **79**, 2345-2357.

Kopljar, I., Labro, A. J., Cuypers, E., Johnson, H. W. B., Rainier, J. D., Tytgat, J. and Snyders, D. J. (2009). A polyether biotoxin binding site on the lipid-exposed face of the pore domain of Kv channels revealed by the marine toxin gambierol. *Proceedings of the National Academy of Sciences of the United States of America* **106**, 9896-9901.

Laine, M., Lin, M. C. A., Bannister, J. P. A., Silverman, W. R., Mock, A. F., Roux, B. and Papazian, D. M. (2003). Atomic proximity between S4 segment and pore domain in shaker potassium channels. *Neuron* **39**, 467-481.

Lange, W., Geissendorfer, J., Schenzer, A., Grotzinger, J., Seebohm, G., Friedrich, T. and Schwake, M. (2009). Refinement of the binding site and mode of

action of the anticonvulsant retigabine on KCNQ K+ channels. *Molecular Pharmacology* **75**, 272-280.

Larsson, H. P., Baker, O. S., Dhillon, D. S. and Isacoff, E. Y. (1996). Transmembrane movement of the Shaker K+ channel S4. *Neuron* **16**, 387-397.

Ledwell, J. L. and Aldrich, R. W. (1999). Mutations in the S4 region isolate the final voltage-dependent cooperative step in potassium channel activation. *Journal of General Physiology* **113**, 389-414.

Lee, H. C., Wang, J. M. and Swartz, K. J. (2003). Interaction between extracellular hanatoxin and the resting conformation of the voltage-sensor paddle in K_v channels. *Neuron* **40**, 527-536.

Lee, S. Y., Lee, A., Chen, J. Y. and MacKinnon, R. (2005). Structure of the KvAP voltage-dependent K+ channel and its dependence on the lipid membrane. *Proceedings of the National Academy of Sciences of the United States of America* **102**, 15441-15446.

Li-Smerin, Y. and Swartz, K. J. (2000). Localization and molecular determinants of the hanatoxin receptors on the voltage-sensing domains of a K+ channel. *Journal of General Physiology* **115**, 673-684.

Li-Smerin, Y. Y., Hackos, D. H. and Swartz, K. J. (2000). alpha-helical structural elements within the voltage-sensing domains of a K+ channel. *Journal of General Physiology* **115**, 33-49.

Long, S. B., Campbell, E. B. and MacKinnon, R. (2005). Crystal structure of a mammalian voltage-dependent Shaker family K+ channel. *Science* **309**, 897-903.

Long, S. B., Tao, X., Campbell, E. B. and MacKinnon, R. (2007). Atomic structure of a voltage-dependent K+ channel in a lipid membrane-like environment. *Nature* **450**, 376-U3.

Mackinnon, R. and Yellen, G. (1990). Mutations affecting TEA blockade and ion permeation in voltage-activated K+ channels. *Science* **250**, 276-279.

Marmont, G. (1949). Studies on the axon membrane I. A new method. *Journal of Cellular and Comparative Physiology* **34**, 351-382.

Nimigean, C. M. and Allen, T. W. (2011). Origins of ion selectivity in potassium channels from the perspective of channel block. *Journal of General Physiology* **137**, 405-413.

Pathak, M. M., Yarov-Yarovoy, V., Agarwal, G., Roux, B., Barth, P., Kohout, S., Tombola, F. and Isacoff, E. Y. (2007). Closing in on the resting state of the shaker K+ channel. *Neuron* **56**, 124-140.

Rangaraju, S., Chi, V., Pennington, M. W. and Chandy, K. G. (2009). Kv1.3 potassium channels as a therapeutic target in multiple sclerosis. *Expert Opinion on Therapeutic Targets* **13**, 909-924.

Sack, J. T. and Aldrich, R. W. (2006). Binding of a gating modifier toxin induces intersubunit cooperativity early in the Shaker K channel's activation pathway. *Journal of General Physiology* **128**, 119-132.

Sack, J. T., Aldrich, R. W. and Gilly, W. F. (2004). A gastropod toxin selectively slows early transitions in the Shaker K channel's activation pathway. *Journal of General Physiology* **123**, 685-696.

Sand, R. M., Atherton, D. M., Spencer, A. N. and Gallin, W. J. (2011). jShaw1, a low-threshold, fast-activating Kv3 from the hydrozoan jellyfish Polyorchis penicillatus. *Journal of Experimental Biology* **214**, 3124-3137.

Schmitz, A., Sankaranarayanan, A., Azam, P., Schmidt-Lassen, K., Homerick, D., Hansel, W. and Wulff, H. (2005). Design of PAP-1, a selective small molecule Kv1.3 blocker, for the suppression of effector memory T cells in autoimmune diseases. *Molecular Pharmacology* **68**, 1254-1270.

Schoppa, N. E. and Sigworth, F. J. (1998). Activation of Shaker potassium channels III. An activation gating model for wild-type and V2 mutant channels. *Journal of General Physiology* **111**, 313-342.

Seoh, S. A., Sigg, D., Papazian, D. M. and Bezanilla, F. (1996). Voltage-sensing residues in the S2 and S4 segments of the Shaker K+ channel. *Neuron* **16**, 1159-1167.

Soler-Llavina, G. J., Holmgren, M. and Swartz, K. J. (2003). Defining the conductance of the closed state in a voltage-gated K+ channel. *Neuron* **38**, 61-67.

Spencer, A. N. (1978). Neurobiology of *Polyorchis* I. Function of effector systems. *Journal of Neurobiology* **9**, 143-157.

Spencer, A. N. (1979). Neurobiology of *Polyorchis* II. Structure of effector systems. *Journal of Neurobiology* **10**, 95-117.

Starace, D. M. and Bezanilla, F. (2004). A proton pore in a potassium channel voltage sensor reveals a focused electric field. *Nature* **427**, 548-553.

Swartz, K. J. (2004). Towards a structural view of gating in potassium channels. *Nature Reviews Neuroscience* **5**, 905-916.

Swartz, K. J. and Mackinnon, R. (1995). An inhibitor of the Kv2.1 potassium channel isolated from the venom of a chilean tarantula. *Neuron* **15**, 941-949.

Swartz, K. J. and MacKinnon, R. (1997). Hanatoxin modifies the gating of a voltage-dependent K+ channel through multiple binding sites. *Neuron* **18**, 665-673.

Tao, X., Lee, A., Limapichat, W., Dougherty, D. A. and MacKinnon, R. (2010). A gating charge transfer center in voltage sensors. *Science* **328**, 67-73.

Tombola, F., Pathak, M. M. and Isacoff, E. Y. (2006). How does voltage open an ion channel? *Annual Review of Cell and Developmental Biology* **22**, 23-52.

Tombola, F., Pathak, M.M., Gorostiza, P., and Isacoff, E.Y. (2007). The twisted ion-permeation pathway of a resting voltage-sensing domain. *Nature* **445**, 546-549

Vernino, S. (2007). Autoimmune and paraneoplastic channelopathies. *Neurotherapeutics* **4**, 305-314.

Villalba-Galea, C. A., Miceli, F., Taglialatela, M. and Bezanilla, F. (2009). Coupling between the voltage-sensing and phosphatase domains of Ci-VSP. *Journal of General Physiology* **134**, 5-14.

Wulff, H. and Pennington, M. (2007). Targeting effector memory T-cells with Kv1.3 blockers. *Current Opinion in Drug Discovery & Development* **10**, 438-445.

Yifrach, O. and MacKinnon, R. (2002). Energetics of pore opening in a voltage-gated K+ channel. *Cell* **111**, 231-239.

Zagotta, W. N., Hoshi, T. and Aldrich, R. W. (1994). Shaker potassium channel gating III. Evaluation of kinetic-models for activation. *Journal of General Physiology* **103**, 321-362.

Chapter 2: Comparing a New Jellyfish Kv3 to Known Mouse Kv3 Channels[1]

Introduction

Voltage-gated potassium channels (K_v) are pore-forming membrane proteins essential to the electrical signaling of excitable cells like neurons and myocytes (Hille, 2001). A specific complement of various ion channel proteins is required to transmit action potentials (AP), and individual channel characteristics modulate AP threshold, amplitude, duration, and frequency. By selectively allowing positive potassium ions to flow out of the cell, K_v channels can prevent, prolong, or hasten an AP depending on intrinsic channel properties like voltage sensitivity, conductance, kinetics of activation, kinetics of deactivation, and kinetics of inactivation. Ultimately, variation in these properties is explained by variation in primary sequence of the channel protein; therefore, differences in K_v sequence are key contributors to the functional variation of excitability, both within and between species.

Structurally, K_v channels have four interlocking subunits each containing a cytoplasmic N-terminal tetramerization domain (T1), six trans-membrane helices (S1 to S6) connected by loop sequences, and a cytoplasmic C-terminal domain. Some K_v channels also contain an inactivation particle in the N-terminus. Functionally, residues from the start of S1 to the end of S4 constitute the voltage-sensing domain. Changes in membrane potential exert a force on positive amino

[1] This work has been published as: Sand, R. M., Atherton, D. M., Spencer, A. N. and Gallin, W. J. (2011). jShaw1, a low-threshold, fast-activating K_v3 from the hydrozoan jellyfish *Polyorchis penicillatus*. Journal of Experimental Biology 214, 3124-3137.

acids in S4, providing the primary electromotive force to open the intracellular gates of S6. The S5, pore loop, S6 region forms the pore domain, which consists of a re-entrant pore loop that acts as a potassium-selective filter supported by the S5 and S6 helices (Long et al., 2007).

In humans, 40 distinct K_v genes have been identified (Harmar et al., 2009), with 17 of these belonging to the K_v1 through K_v4 subfamilies. In *Drosophila melanogaster* alternative splicing produces at least 16 different K_v subunits from four genes: the Shaker (K_v1) gene gives rise to seven mRNAs, Shab (K_v2) to four, Shaw (K_v3) to three, and Shal (K_v4) to two (Tweedie et al., 2009). Regardless of the mechanism by which it arises, the diversity of K_v sequences in both flies and humans contributes significantly to the functional complexities of their respective nervous systems.

Shaker-type (K_v1) channels are the most varied and well-characterized K_v subtype. They tend to mediate fast-activating currents and generally manifest hyperpolarized threshold potentials, which makes them suited to set the resting membrane potential and modulate excitability. In contrast, characterized mammalian Shaw-type (K_v3) channels generally open with large depolarizations, with V_{50} values ranging from -1 to +19 mV (Gutman et al., 2005) and display both inactivating (or A-type) and non-inactivating currents. The latter phenotype appears to be optimal for shortening the inter-spike interval of repetitively firing cells (Rudy and McBain, 2001). Much less is known about K_v3 channels from invertebrates, but those that have been profiled generally display slower kinetics

than mammalian K_v3 channels. *D. melanogaster* Shaw, often considered the archetypal K_v3 channel, has an extremely negative threshold voltage of -70 mV and a 95% rise time of 102 ms at 0 mV (Wei et al., 1990). Two other characterized invertebrate K_v3 channels have slower opening kinetics than *D. melanogaster* Shaw, but open at more positive potentials. *Notoplana atomata* (a platyhelminth) $K_v3.1$ appears to take up to 100 ms to fully activate and has a V_{50} of +9.3 mV (Klassen et al., 2006), while *C. elegans* egl-36 channels open over a period of 800 ms and half-activate at +63 mV (Johnstone et al., 1997).

The molecular basis of such disparate phenotypes can be better understood by comparison with Shaw channels from organisms that diverged from other metazoans early in evolutionary history, like cnidarians. This approach has been successful in understanding other K_v subtypes. Probing cDNA from the hydrozoan jellyfish *Polyorchis penicillatus* by degenerate PCR previously yielded two A-type Shaker transcripts, jShak1 and jShak2 (GenBank accession AAB02603 and AAB02604) (Jegla et al., 1995). The short S3-S4 loop and atypical amide residues in S2 of jShak1 proved useful in elucidating the interaction of S4 with other parts of the voltage-sensing domain during activation (Klassen et al., 2008). Two Shal channels have also been characterized from *P. penicillatus*, jShal-alpha-1 and jShal-gamma-1 (AAB39750 and AAB39749) (Jegla and Salkoff, 1997). jShal-gamma does not form functional homotetramers, but co-assembles with A-type jShal alpha subunits to drastically increase the rate of inactivation (Jegla and Salkoff, 1997).

Here, we report the cloning and characterization of jShaw1, isolated from *P. penicillatus* and the first K_v3 channel reported from outside the bilateria. Using two-electrode voltage clamp analysis of *Xenopus laevis* oocytes injected with *in vitro* transcribed mRNA we compared steady state and kinetic properties and pharmacological sensitivities of macroscopic jShaw1, mouse $K_v3.1$ and $K_v3.2$ currents. Characterization of jShaw1 will help us to understand the general process of activation and inactivation in the K_v3 subfamily, and the diverse roles fast-activating channels play in evolutionarily distant species.

Materials and Methods

jShaw1 Cloning

Novel K_v genes were found using degenerate PCR primers designed to target conserved sequences in the pore (MTTVGYGD) and S6 (G-VL (T/V) IAL) to amplify from genomic DNA isolated from gonad tissue of *P. penicillatus* medusae (Jegla et al., 1995). One of the amplified sequences was the starting point for isolating the cDNA of jShaw1.

Total RNA was isolated from *P. penicillatus* medusae collected at the Bamfield Marine Sciences Center using the RNAeasy Midiprep kit (Qiagen, Mississauga, ON, CAN) or by density gradient centrifugation using cesium trifluoroacetate (Okayama et al., 1987). The majority of the bell, which is rich in mesoglea but has few cells, was dissected away, approximately 2 mm above the marginal ring. The remaining material (~300 mg per organism) was then homogenized in 4 ml of homogenization buffer (Qiagen RLT buffer for the RNAeasy kit, guanidinium

thiocyanate solution for the density gradient centrifugation method) and processed according to the published instructions. The purified total RNA was stored at -80˚C.

cDNA for *P. penicillatus* was reverse transcribed from total RNA. Oligo-dT primed cDNA synthesis was carried out using a ThermoScriptRT or GeneRacer kit (Invitrogen, Burlington, ON, CAN). cDNA ends were amplified using the 5' RACE and 3' RACE method (Frohman, 1994) with nested primers as implemented in the GeneRacer kit (Invitrogen). The resulting PCR products were cloned and sequenced. Sequence data from PCR products were assembled into a consensus sequence using the Staden (v. 1.7.0) software (Staden et al., 2000). The sequence of jShaw1 has been deposited in GenBank (accession number GQ249160).

Alignments and Phylogenetic Analysis

A set of 173 K_v3 channel amino acid sequences was retrieved from the most recent update of the VKCDB database (Gallin and Boutet, 2010; Li and Gallin, 2004) and aligned using MUSCLE (Edgar, 2004). Removal of positions with more than 5% gaps yielded a data matrix of 235 characters. This matrix was used to infer a phylogenetic tree using MrBayes (Huelsenbeck and Ronquist, 2001; Ronquist and Huelsenbeck, 2003), with 4 independent runs each consisting of 4 chains run for 10^7 generations with sampling every 100^{th} generation, and with the temperature parameter set to 0.05. A consensus tree was generated from the four runs with a burn-in of the first 50001 trees. A more limited phylogenetic analysis

of only the 18 cnidarian K_v3 channels was performed with a 215-character dataset with the same conditions as above, except the temperature parameter was set to 0.2.

Homology Modeling

The homology model depicted in Figures 2B and 2C was created using the Swiss-Model web site (Arnold et al., 2006). The jShaw1 protein sequence was aligned with rat $K_v1.2$ protein sequence and the alignment was truncated to include just the core channel structure, missing both the N-terminal and C-terminal cytoplasmic domains, which have low similarity between the two sequences. The alignment was then used to model the jShaw1 structure on the structure recently generated by normal mode refinement of the original $K_v1.2$ crystal structure (Chen et al., 2010). The images were created using PyMol v1.4 (DeLano, 2002).

Expression Plasmid Construction

Full-length jShaw1 was amplified from cDNA using a sense primer containing an Xho I restriction site followed by the Kozak consensus sequence and the first 31 nucleotides of the open reading frame (ORF), and an antisense primer with an Spe I cut site and 38 bases of sequence including the natural stop codon. *Mus musculus* $K_v3.1$ (GenBank accession BC132439) and $K_v3.2$ (GenBank accession BC116290) cDNA clone ORFs (OpenBiosystems, Huntsville, AL, USA) were amplified with sense and antisense primers containing Xho I and Spe I sites, respectively. Amplicons were double digested and ligated into the vector pXT7 (Dominguez et al., 1995). After transformation into XL1-Blue *Escherichia coli*,

individual colonies were picked from ampicillin selection plates and inoculated into 5 ml overnight cultures (Terrific Broth (Ausubel et al., 1987) with 100 μg/ml ampicillin). Plasmid was purified from overnight cultures using a Wizard Miniprep Kit (Promega, Madison, Wisconsin, USA) and the full ORFs were sequenced to confirm that no errors had been introduced by PCR.

For preparation of mRNA from the cloned sequences for microinjection, plasmids were linearized with Xba I, resolved on agarose electrophoresis gels, and purified using the QiaQuick Gel Extraction Kit (Qiagen). Capped mRNAs were prepared by in vitro transcription of the linearized template using the mMessage mMachine (Ambion, Austin, Texas, USA) T7 polymerase kit, and stored at -80°C.

Expression in Xenopus laevis Oocytes

2-year old *X. laevis* females were anaesthetized in 0.17% ethyl 3-aminobenzoate methanesulfonate salt (MS-222; Sigma-Aldrich, Oakville, ON, CAN) for 40 minutes prior to ovarian lobectomy. To access the ovarian lobes, a small incision was made approximately 1 cm lateral to the ventral midline and 1 cm caudal to the pelvic girdle. Once removed, the lobes were manually pulled into half-centimeter clumps, rinsed three times, and treated with 2 mg/ml collagenase IA (Sigma-Aldrich) in modified Barth's medium (MBM; in mM: NaCl 88, KCl 1, $Ca(NO_3)_2$ 0.33, $CaCl_2$ 0.41, $MgSO_4$ 0.82, $NaHCO_3$ 2.4, HEPES 10, sodium pyruvate 2.4; supplemented with 0.1 g/L penicillin G and 0.05 g/L gentamicin sulfate; pH 7.5 with Tris base) (Huang et al., 1993) for two hours at room temperature on a rotating shaker. This was followed by a 20-40 minute treatment

under identical conditions in a hypertonic phosphate solution (100 mM K_2PO_4, pH 6.5 with HCl) for defolliculation. Mature stage V-VII oocytes were cultured in MBM at 18°C before and after microinjection. Oocytes were injected with 1 to 5 ng of mRNA in 20 nl or less using a Nanoject II injector (Drummond Scientific Company, Broomall, PA, USA). The amount of mRNA was adjusted for each channel to minimize artifacts introduced by high expression (> 20μA; (Grigoriev et al., 1999)). Each analysis in this paper is from three separately prepared batches of oocytes that were all injected with a single mRNA species, so the electrophysiological characteristics that are derived are for homotetramers with no additional accessory subunits. There was no significant variation between batches in any of the properties that were measured,

Two-electrode Voltage Clamp Electrophysiology

Recordings were made 1-2 days post-injection using a GeneClamp 500B amplifier (Molecular Devices, Sunnyvale, CA, USA) connected to a PC (Dell, Austin, TX, USA) running pClamp 9 software (Molecular Devices). Data were acquired through a 1322A analogue-to-digital converter and analyzed using Clampfit 9.2 (Molecular Devices) and SigmaPlot (Systat Software, Inc., Point Richmond, CA, USA). Data were filtered at 1 kHz through a 4-pole Bessel filter and sampled at 10 kHz. Pipettes were pulled from 1.5 mm outside diameter borosilicate filament capillary tubing using a PMP-102 automatic puller (MicroData Instrument, Inc., South Plainfield, NJ, USA) to resistances <1 MΩ. Oocytes were bathed in ND96 (in mM: NaCl 96, KCl 2, $CaCl_2$ 1.8, $MgCl_2$ 1, HEPES 5) at room temperature during all experiments. Measurements were

performed with leak subtraction (P/N = 4). Chloride currents native to *X. laevis* oocytes (Miledi and Parker, 1984) were blocked with 1 mM diisothiocyanatostilbene-2,2′-disulfonic acid (DIDS), present in the bath solution during steady-state and kinetic analysis protocols. As DIDS is known to interfere with jShak1 and jShak2 channels (Grigoriev et al., 1997), I-V graphs were compared before and after application of DIDS to look for reductions in current. DIDS had no visible effects on either the I-V curves or the kinetic behavior of the channels. To ensure the independence of recordings from each sweep, the duration of depolarization in voltage protocols were limited to 50 ms and at least 20 ms recovery time was provided between sweeps.

Steady-state opening of the channels was measured using an isochronal tail current protocol. Oocytes were held at -90 mV for 10 ms before a series of 50 ms depolarizing pulses from -80 mV to +80 mV in 2 mV steps, followed by a 50 ms step to -50 mV for outward tails and a 100 ms return to -90 mV. Activation kinetics were analyzed using traces from the isochronal tail current protocol, and also using a protocol which took the cell through incremental pre-depolarizing steps (Δ5 mV, 50 ms) immediately before a 50 ms depolarization to +60 mV. Deactivation kinetics were investigated by depolarizing oocytes to +60 mV for 50 ms, then immediately stepping to a range of tail voltages ranging from -70 to -10 mV in 5 mV steps. For experiments using tetraethyl ammonium (TEA) and 4-aminopyridine (4AP) (Sigma-Aldrich), oocytes were subjected to the isochronal tail current protocol and data from the +60 mV pulse were presented. During 4AP experiments a 10 ms pre-pulse to 40 mV was included to allow access to the

intracellular binding site (Shieh and Kirsch, 1994). TEA and 4AP were dissolved in ND96 and delivered by gravity-fed perfusion through Teflon tubing or manually using a Pasteur pipette.

Data Analysis

Steady-state voltage-conductance curves were obtained by fitting isochronal tail currents to the sum of two exponential decays:

$$I_{tail} = \left(A_1 e^{-t/\tau_1} + C_1\right) + \left(A_2 e^{-t/\tau_2} + C_2\right) \quad (2.1)$$

where I_{tail} is in μA, and t, τ_1, and τ_2 are in ms. The start of the fitting range was set at ~2 ms after the beginning of the tails. The parameters generated by fitting the remainder of the tails with equation (1) were used to calculate the predicted current at the beginning of the fitting range. Since the driving force is constant during each tail step, the current is proportional to conductance (G). G was normalized using:

$$G_{normal} = \frac{G}{G_{max}} = \frac{I}{I_{max}} \quad (2.2)$$

for each experiment. Sigmoid conductance-voltage curves were then fitted with a fourth-order Boltzmann relation (Hodgkin and Huxley, 1952):

$$G = y_0 + \frac{G_{max}}{\left[1 + e^{\frac{-(V - V_{50})}{b}}\right]^4} \quad (2.3)$$

where V and the half-activation voltage V_{50} are in mV, and b is the slope factor in mV. Since this function is raised to the fourth power, the values for V_{50} and b

represent one subunit only. V_{50} values for tetrameric channels were calculated by solving for V when $G/G_{max} = 0.5$.

The pre-opening, early, rising, and late phases of activation were analyzed separately. The pre-opening phase was described by the time to threshold, i.e. the time from the beginning of the depolarizing voltage step to the time when current exceeded three standard deviations of baseline and did not decrease afterward (to avoid the stimulus artifact). Baseline values were found by averaging the last ten data points during the -90 mV holding potential before the step change. The early phase was represented by the threshold-to-10% rise time, and the rising phase by the 10-to-90% rise time. All three parameters were plotted against voltage and fitted with single exponential decay functions:

$$Rise\ time = y0 + Ae^{-bV} \tag{2.4}$$

with rise times in ms, and V in mV. The late phase of activation, or current occurring after the half-maximal point, was isolated and fitted to either a single (for mouse $K_v3.1$) or the sum of two exponential equations (for jShaw1 and mouse $K_v3.2$):

$$I = A(1 - e^{-t/\tau}) \tag{2.5}$$

$$I = \left(A_1 e^{-t/\tau_1} + C_1\right) + \left(A_2 e^{-t/\tau_2} + C_2\right) \tag{2.6}$$

with I in μA, and t, τ, τ_1, and τ_2 in ms. Activation kinetics were also investigated by a pre-depolarization protocol, described above, and current starting 1 ms after

the rise to +60 mV was fitted with equation (5). Resulting time constants were plotted against voltage.

Deactivation kinetics were examined using a variable tail step protocol, described above. Since the holding potential for each of the deactivation steps was different, the resulting tail currents are a function of channel conductance and the driving force, $V-V_{rev}$, with V_{rev} being the reversal potential for potassium. To account for the different driving forces at the various tail steps, currents were divided by driving force to find conductance:

$$G = \frac{I}{V - V_{rev}} \tag{2.7}$$

We used a value of -80 mV for V_{rev} since in all our recordings the reversal potential for K^+ ions was around -80 mV and a 5 mV change in the estimated V_{rev} had little effect on the analysis. Tail conductance was fitted by equation (1), excluding the first 1 ms, producing a fast and slow time constant that were plotted against voltage. The fraction of total conductance described by the fast and slow time constants was also determined at each tail step.

Concentration-effect curves for TEA and 4AP were calculated from the fraction of current relative to no-drug control (I_{drug}) at the end of a +60 mV pulse, and plotting against concentration. Resulting curves were fitted with a 4-parameter logistic function:

$$G = y_0 + \frac{G_{max}}{\left[1 + e^{\frac{-(V - V_{50})}{b}}\right]^4} \tag{2.8}$$

with I_{max} in μA and [D] and IC_{50} in M.

Results

jShaw1 Sequence Analysis

Degenerate PCR performed on genomic *P. penicillatus* DNA produced several amplicons extending from the highly conserved K_v pore into the flanking S6 region. Gene-specific primers designed from one of these sequences were used in 5' and 3' RACE to obtain a full-length ORF. The jShaw1 mRNA contains an ORF 1935 base pairs in length (GenBank accession GQ249160), coding for a single K_v peptide of 644 residues (GenBank accession ACS91465).

BLASTP search (Camacho et al., 2009) of the NCBI non-redundant protein database demonstrates significant alignments with a number of predicted protein sequences from cnidarian genome sequencing projects. The most similar protein sequences from experimentally validated channel sequences are to Shaw (K_v3) channels from *Aplysia californica* (California sea hare; E value 7e-89), *Panulirus interruptus* (California spiny lobster; E value 4e-87), and *D. melanogaster* (E value 6e-87). Each share close to 40% identical and 60% conserved residues with jShaw1. Identification of this channel as a member of the K_v3 family was confirmed by alignment with profiles of different gene family protein sequences using HMMer (Eddy, 2010) and by a large-scale phylogenetic analysis that included sequences from all of the K_v families (not shown).

A phylogenetic tree was inferred with MrBayes ($_v$ 3.1.2) using a set of 173 K_v3 channel sequences (Figure 2-1). The jShaw1 channel is robustly included within a monophyletic group of cnidarian K_v3 paralogs, basal to a clade of four paralogs from *Hydra magnipapillata* (another hydrozoan). *N. vectensis* (an anthozoan) does not have paralogs within this group. The fact that there are four *H. magnipapillata* channels forming a clade as a sister group of jShaw1 is not due to duplications in the annotation of the *H. magnipapillata* genome, since each of the proteins is encoded on a distinct genomic sequence.

jShaw1 has the typical six trans-membrane domain architecture of K_v channels (Figure 2-2A). The N-terminus was identified as the first methionine residue after an in-frame stop codon, and the predicted N-terminal sequence aligns well with the N-termini of other K_v3 channels. Multiple alignment of the core jShaw1 peptide sequence (from the N-terminus of the first transmembrane helix to the C-terminus of the sixth transmembrane helix) with other K_v3 sequences and *D. melanogaster* Shaker revealed several notable differences (Figure 2-2A). jShaw1 has a relatively short S1-S2 linker for a K_v3 channel, 15 residues in length. Most K_v3 channels have S1-S2 loops in the range of 30-36 residues: mouse $K_v3.1$ has 34 and mouse $K_v3.2$ has 32. jShaw1 also lacks the N-glycosylation consensus sequence (N-X-S/T) found in the S1-S2 linker of the four other channels of the alignment and in many other K_v sequences. Rat $K_v1.1$, 1.2, and 1.4 are glycosylated at N-X-T sites (Shi and Trimmer, 1999) and rat $K_v3.1$ is modified at two N-X-T sites in the S1-S2 loop (Cartwright et al., 2007). Jellyfish K_v1 channels jShak1 and jShak2 (Jegla et al., 1995) as well as jShal (a K_v4 channel)

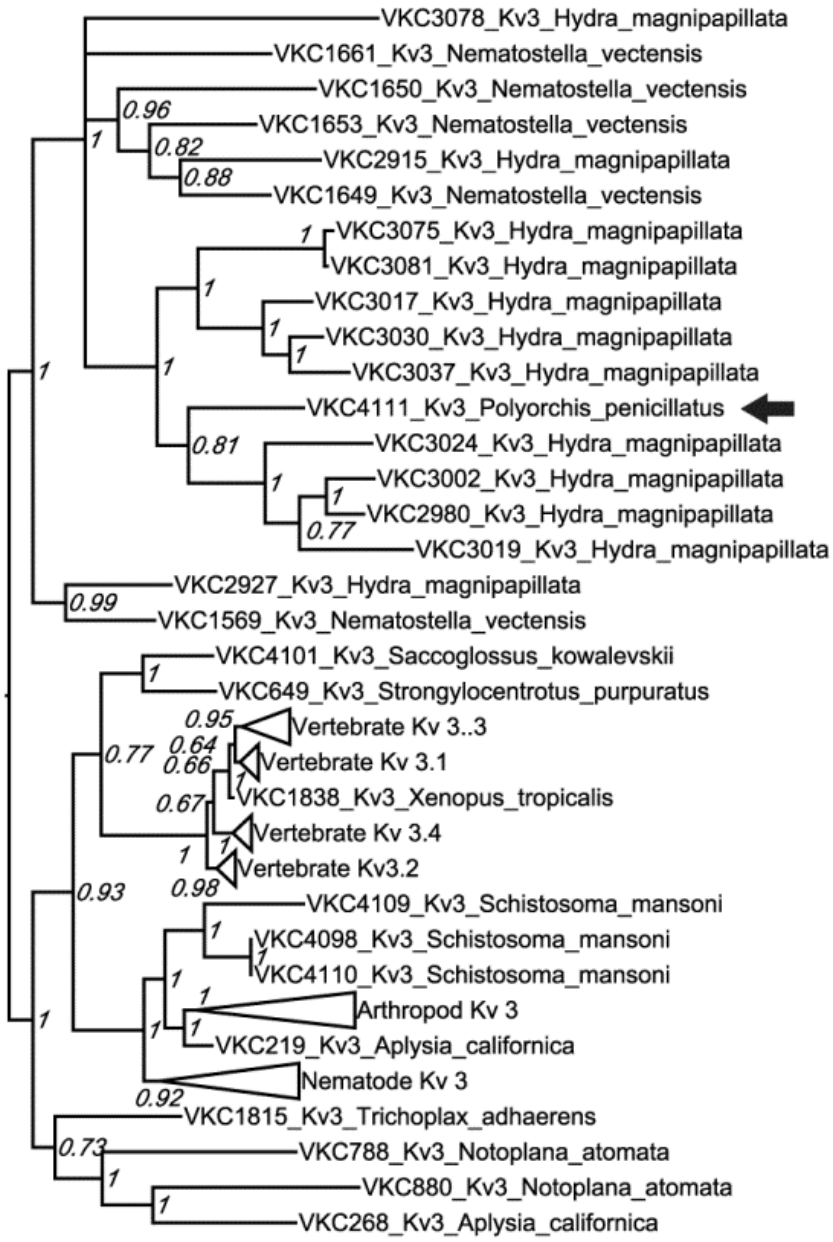

Figure 2-1. Phylogenetic tree of the relationships between K_v3 family channel proteins. This tree was inferred using 173 channel sequences. The four vertebrate subfamilies, the arthropod clade and the nematode clade have each been collapsed to a triangle to simplify the presentation. Three cnidarian organisms are included in this tree: the genomes of *Nematostella vectensis*, an anthozoan, and *Hydra magnipapillata*, a hydrozoan, have been sequenced and the channel protein sequences are derived from gene predictions, whereas *Polyorchis penicillatus*, a hydrozoan, is represented by the jShaw1 channel (indicated by a heavy arrow to the right of the tree).

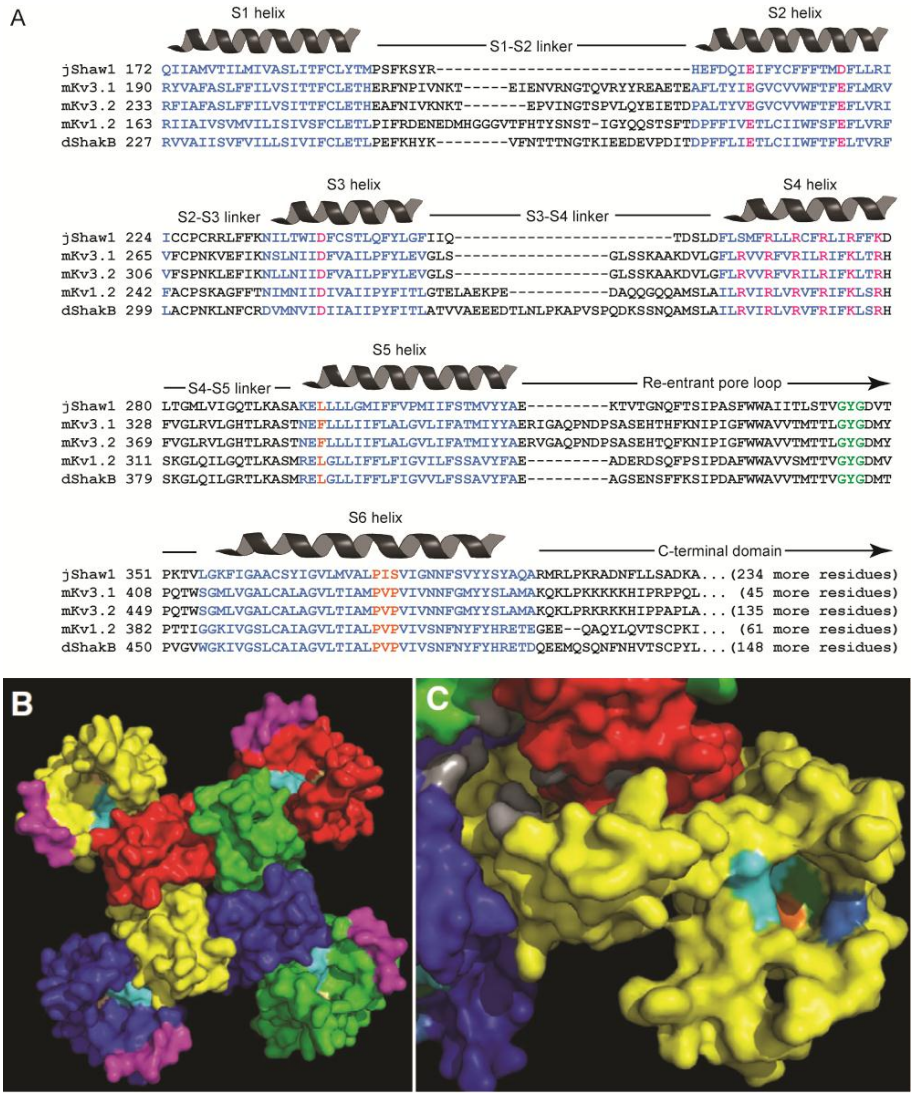

Figure 2-2. Structural features of jShaw1. A, MUSCLE alignment of the jShaw1 protein sequence with mouse K_v3.1 and K_v3.2, *D. melanogaster* Shaker B, and rat K_v1.2. The core structure of the channel, with N-terminal and C-terminal cytoplasmic domains trimmed off, is shown. Numbers indicate the residue number of the first residue shown in each line for each individual channel sequence. Helices are annotated based on alignment to homologous regions in rat K_v1.2 and he sequences are highlighted in blue. Residues of functional interest are highlighted in red as follows: S2 and S3 helices – acidic residues that form salt bridges with basic residues in S4; S4 helix – primary voltage-sensing residues; S5 region – residue involved in deactivation kinetics; pore loop – potassium selectivity filter (highlighted in green); S6 helix – conserved PVP hinge site. Channels originated from: jShaw1 – *Polyorchis penicillatus*; dShakB – Drosophila melanogaster; mK_v3.1 and mK_v3.2 – *Mus musculus*; rK_v1.2 – *Rattus norvegicus*. B, Homology model of jShaw1 created using Swiss Model (Arnold et al., 2006), based on a recently refined model of rat K_v1.2 (Chen et al., 2010), viewed from the extracellular direction. The subunits in the tetramer are colored red, green blue and yellow. The S3-S4 loop in each subunit is colored magenta. The basic residues in the S4 helix of each subunit are colored light blue. C, Same homology model as in panel B, magnified on the yellow subunit and viewed from the cytoplasmic aspect at an angle to give a single view of the residues associated with the voltage sensor. Basic residues in S4 are light blue, F214 is green, D218 is dark blue, D241 is orange, and the PIS motif residues are colored grey.

contain the N-glycosylation motif in their respective S1-S2 loops.

The S3-S4 loop is also shorter in jShaw1 than in either of the mouse K_v3 channels, 8 residues instead of 15. The S4 helix in the K_v3 channels is also apparently shorter than the S4 helix in the K_v1 family of channels, although since this analysis is based on a heuristic homology model it is also possible that the K_v3 S4 helices are as long as the K_v1 S4 helices. In this case the jShaw1 S3-S4 loop would be even shorter than indicated above.

jShaw1 also differs from the mouse and *D. melanogaster* K_v3 channels in that it has five positively charged residues in the S4 helix - one less than the mouse channels and one more than *D. melanogaster* Shaw. In most voltage-gated channels the basic residues in S4 can form stabilizing salt-bridges in both the open and closed states with acidic residues in S2 and S3 at positions equivalent to E283, E293, and D316 in *D. melanogaster* Shaker (Decaen et al., 2009; Papazian et al., 1995; Schow et al., 2010; Silverman et al., 2003). jShaw1 shares the same residues aligned with Shaker positions E283 and D316, but has a less bulky aspartate (D218) aligned with Shaker E293 (Figure 2-2A). In the cytoplasmic end of S5, jShaw1 differs from the mouse K_v3 channels at a position shown to influence the rate and voltage dependency of deactivation, equivalent to Shaker L396 (Shieh et al., 1997). Here, like both K_v1 channels in the alignment, jShaw1 contains a leucine whereas mouse $K_v3.1$ and $K_v3.2$ contain phenylalanine (Figure 2-2A).

The selectivity filter of the jShaw1 pore region is a typical TVGYG sequence. jShaw1 also has a threonine at the position aligned with Shaker T449, a residue linked to TEA sensitivity (MacKinnon and Yellen, 1990). In contrast, the highly conserved PVP hinge sequence in S6 is PIS in jShaw1.

jShaw1 also has a long C-terminus, 265 residues, whereas the mouse K_v3.1 C-terminal domain is 75 residues, that of K_v3.2 is 165, and that of *D. melanogaster* Shaw is 85. jShaw1 lacks an N-terminal inactivation particle as found in the B isoform of the *D. melanogaster* Shaker channel; the total N-terminal sequence prior to the T1 domain is only 18 amino acids in length for jShaw1, whereas the inactivation ball in Shaker B is 20 amino acids long, and is tethered to the end of the T1 domain by a further 41 amino acids. Characterized K_v3 channels do not generally exhibit fast N-type inactivation, with the exception of mammalian K_v3.4 (Schroter et al., 1991).

Electrophysiology

Steady-State Properties

Microinjection of jShaw1, mouse K_v3.1, and K_v3.2 mRNA yielded functional channels in *X. laevis* oocytes in as little as 18 hours, as evidenced by robust delayed rectifier currents (Figure 2-3A). Some oocytes had maximum currents as high as 40 μA, but to avoid the confounding effects of high channel expression (Grigoriev et al., 1999), we only considered those that yielded a maximum current between 4 and 18 μA. Slight C-type inactivation could be seen during the 50 ms depolarization in all three channels, especially in mouse K_v3.1 at higher voltages

(Figure 2-3A). When stimulated with a series of increasing voltages, jShaw1 channels started conducting at -45 mV, about 25 mV more negative than the threshold of the two mouse channels (Figure 2-3B; Table 2-1) but more positive than -70 mV, reported for *D. melanogaster* Shaw (Wei et al., 1990). Isochronal tail current analysis yielded sigmoid conductance-voltage curves that were fitted by a fourth-order Boltzmann relation, meaning the derived V_{50} and Boltzmann slope values represent that of a single subunit and not the whole channel. Channel V_{50} values were calculated by solving for voltage that induced conductance equal to half of maximum (see Materials and Methods).

jShaw1 had a single-subunit V_{50} (voltage at which half of the individual subunits in the tetrameric channel were active) of -54.4 ± 6.0 mV and a channel V_{50} (voltage at which half the channel tetramers were open) of -29.6 ± 1.2 mV (n = 9) (Figure 2-3B; Table 2-1), about 40 mV more negative than the mouse channels and significantly different (One-way ANOVA; $p<0.001$ for each). Mouse $K_v3.1$ had a channel V_{50} of +9.4 ± 1.9 mV (n = 9), which was significantly more negative than published results for this channel reporting a V_{50} of +16 mV in *X. laevis* oocytes (Yokoyama et al., 1989). We found a channel V_{50} of +11.3 ± 1.4 mV (n = 9) for mouse $K_v3.2$, and while there is a lack of published V_{50} values for this channel, our results agree well with those of rat $K_v3.2$, which has a V_{50} of +13 mV (McCormack et al., 1990). Mouse and rat $K_v3.2$ differ by three substitutions and a four-residue insertion in the N-terminal T1 domain and one substitution in the loop between S1 and S2.

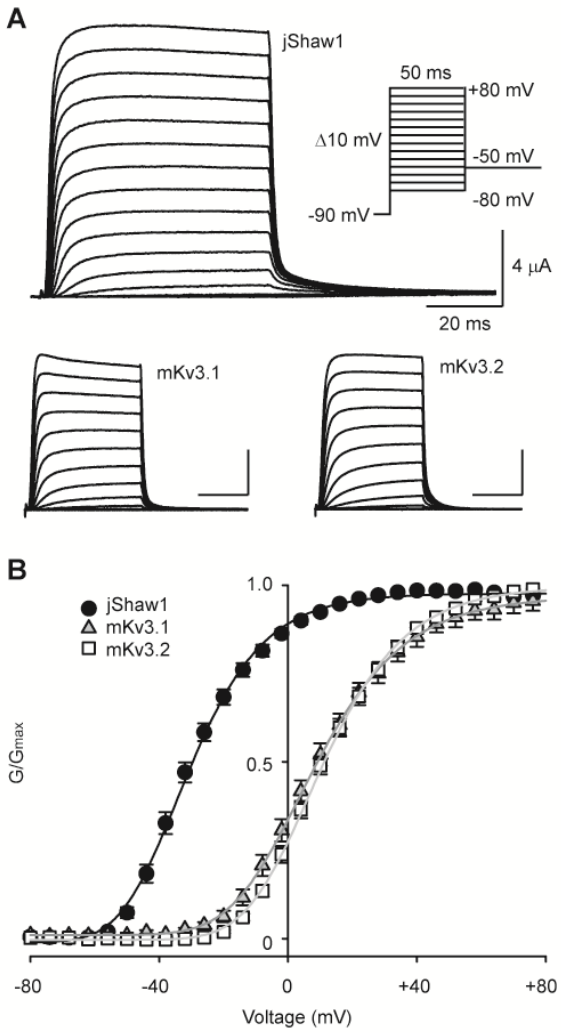

Figure 2-3. Steady-state current and conductance of jShaw1, mouse $K_v3.1$ and $K_v3.2$. A, Representative two-electrode voltage clamp traces from *X. laevis* oocytes expressing the channels. Currents were elicited via the depicted voltage protocol. Data are shown in 10 mV increments but were collected in 2 mV steps. Scale bars for $mK_v3.1$ and $mK_v3.2$ have the same values as those shown for jShaw1. B, Normalized conductance-voltage relationships derived from isochronal tail current analysis for jShaw1 (filled circles), $mK_v3.1$ (shaded triangles), and $mK_v3.2$ (open squares). Solid lines represent the best fit of a Boltzmann function raised to the fourth power. Channel V_{50} values were -29.6 mV for jShaw1, +9.3 for $mK_v3.1$ and +11.3 mV for $mK_v3.2$. The differences between the jellyfish and mouse V_{50} values were both statistically significant ($p < 0.001$), whereas the V_{50} values for the two mouse channels were not different ($p = 0.376$). Boltzmann slopes for single subunits were statistically different between jShaw1 (14.3 mV), $mK_v3.1$ (17.1 mV), and $mK_v3.2$ (15.8 mV) with p values ranging from <0.001 to 0.014 in pairwise comparisons, although the slopes of the full channels (the fourth order fit) are similar. Data were collected in 2 mV increments but are shown every 4 mV for clarity. Data shown are mean ± s.e.m. (n = 9 for each).

Steady-state Properties	**jShaw1**	**mK$_v$3.1**	**mK$_v$3.2**
Threshold of activation (mV)	-45	-20	-20
Whole-channel V_{50} (mV)	-29.6 ± 1.2 (9)	+9.3 ± 1.9 (9)	+11.3 ± 1.4 (9)
Single-subunit V_{50} (mV)	-54.3 ± 1.7 (9)	-20.0± 1.6 (9)	-15.2 ± 1.1 (9)
Single-subunit Boltzmann slope (mV/e)	+14.3 ± 0.9 (9)	+17.1 ± 0.5 (9)	+15.8 ± 0.4 (9)

Table 2-1. Steady-state properties of *Polyorchis penicillatus* jShaw1, *Mus musculus* K_v3.1 and K_v3.2 expressed in *X. laevis* oocytes. Analyses were performed on whole-cell currents collected by two-electrode voltage clamp. Threshold voltages were approximated from current-voltage graphs (not shown). Whole-channel V_{50} values were derived from the single-subunit V_{50} values as described in Materials and Methods. Data are reported ± s.e.m. with n values in parentheses, except for threshold voltages.

The conductance-voltage plot for jShaw1 had a steeper slope in the quasi-linear portion of the curve (Figure 2-3B). This was reflected in the Boltzmann slope factor, which indicated that for one jShaw1 subunit, 14.3 ± 0.9 mV were required for an e-fold change in conductance (n = 9). Mouse $K_v3.1$ and $K_v3.2$ required 17.1 and 15.8 mV per e-fold change, respectively (Table 2-1), and were statistically different from jShaw1 (One-way ANOVA; p = 0.012). The mouse channels were not significantly different from each other with respect to V_{50} (p = 0.376) but were with respect to single-subunit Boltzmann slope (p = 0.014).

Activation Kinetics

Activation kinetics were investigated using voltage clamp current traces. The time-to-threshold, early phase rise time (0-10%), and middle phase rise time (10-90%) were evaluated as measures of activation kinetics (Figure 2-4D-F). All activation time constants decreased exponentially with increasing voltage and were fit with equation (4), a single exponential decay function. To examine how rise times change with voltage, we looked at two parameters from the fit: the b value, or the change in rise time associated with incremental changes in voltage, and the A value, which determines how negatively or positively shifted the response is on the voltage axis.

Threshold times decreased exponentially approaching an asymptotic value near 1.5 ms for all three channels (Figure 2-4D, Table 2-2). This asymptote could represent either a lower limit to the latency of opening or a limitation of the recording equipment. Single exponential fits produced b values of 0.067, 0.069,

and 0.078 for jShaw1, mouse K_v3.1 and K_v3.2, respectively (Table 2-2), indicating that mouse K_v3.2 was more sensitive to changes in membrane potential than the other two channels. The A parameter values for the three channels were 0.047, 0.283, and 0.147 showing that jShaw1 voltage sensitivity was shifted to the most negative potentials, and the K_v3.2 channel sensitivity was shifted to a more negative potential than K_v3.1.

The time from threshold to 10% of maximum current was also compared across a range of voltages (Figure 2-4E). In this phase the relationships of rise time to voltage were less steep than those of the pre-opening kinetics. jShaw1 had faster 0-10% times overall with values ranging from 0.15 to 0.06 ms (Figure 2-4E). Mouse K_v3.2 was slowest, with values ranging from 0.25 to 0.12 ms. Single exponential decays described the voltage-sensitivities well, and produced b values (Table 2-2) that reveal jShaw1 to be most sensitive to incremental changes in membrane potential. However, the rise times of jShaw1 change the least in the range of voltages tested. This was reflected in the A parameter values (Table 2-2) which show that the absolute sensitivity of jShaw1 is shifted in the negative direction compared with K_v3.1, which is shifted more negative than K_v3.2.

Mouse K_v3.1 manifested the fastest 10-90% rise time, 2.09 ms at +80 mV compared to 4.01 ms for jShaw1 (Figure 2-4F). Single exponential fits to the 10-90% rise times against voltage indicate that mouse K_v3.2 was least sensitive to incremental changes in voltage. jShaw1 has the lowest absolute sensitivity to voltage because the curve is shifted to the negative (as evidenced by the small A

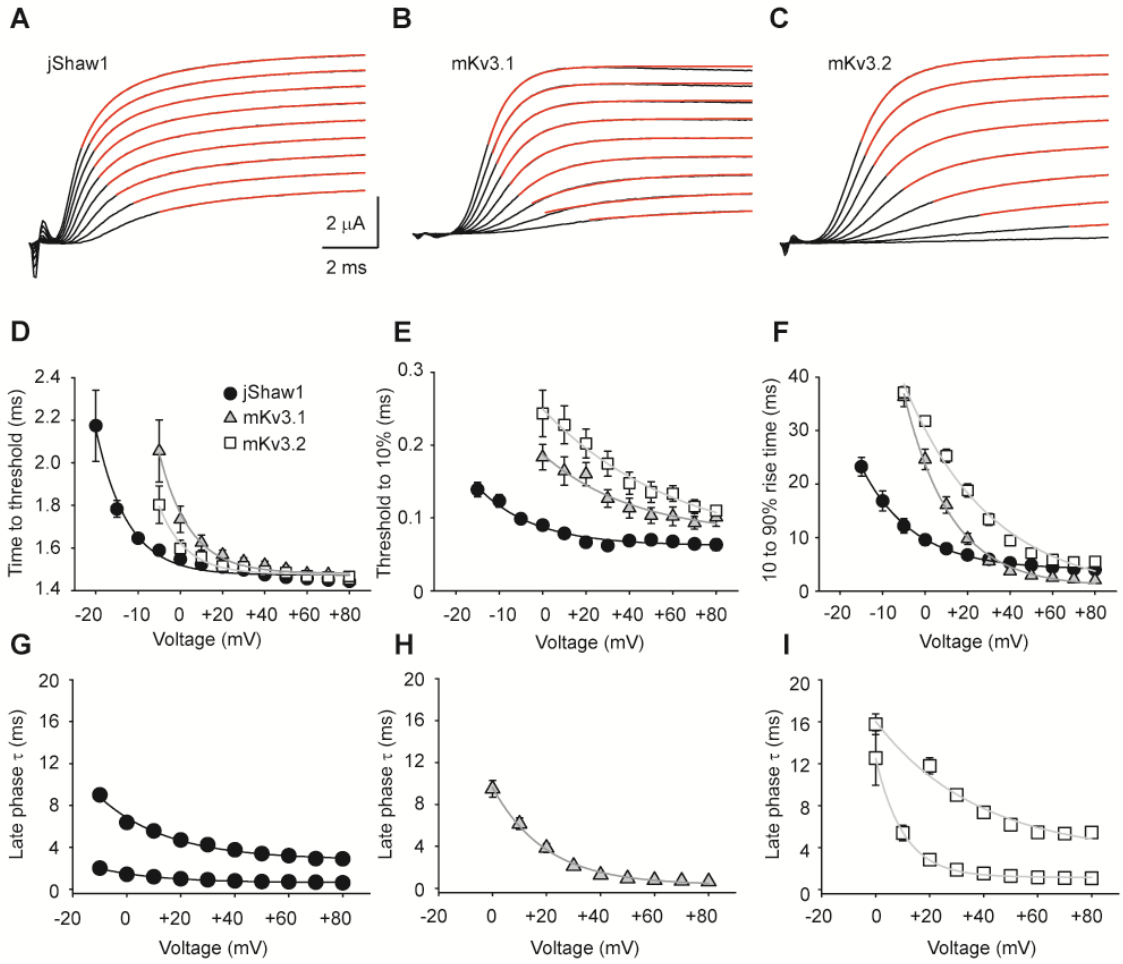

Figure 2-4. Activation kinetics of jShaw1, $mK_v3.1$, and $mK_v3.2$. A-C, The first 10 ms of voltage clamp currents elicited after stepping to a range of depolarizing voltages from a holding potential of -90 mV. Traces from -10 to +80 mV steps are shown in 10 mV increments. The late phase for each trace, defined as anything above half-maximal, was fitted to a single or a sum of two exponential equations (red lines). The scale bars for jShaw1 apply to all traces. D, Time to threshold at different activating voltages for jShaw1, $mK_v3.1$, and $mK_v3.2$. Data shown are the time from the beginning of the depolarizing voltage step to the time when current was at least three standard deviations above baseline (see Materials and Methods). The voltage sensitivity of time to threshold was fitted with single exponential decays for all three channels (solid lines). E, Threshold-to-10% rise time for jShaw1, $mK_v3.1$, and $mK_v3.2$. The voltage sensitivity of threshold-to-10% rise time was fitted with single exponential decays for all three channels (solid lines). F, 10-to-90% rise time for jShaw1, $mK_v3.1$, and $mK_v3.2$. The voltage sensitivity of 10-to-90% rise time was fitted with single exponential decays for all three channels (solid lines). G-I, Late phase time constants (τ) for jShaw1, $mK_v3.1$, and $mK_v3.2$. τ values were obtained by averaging the results of the exponential fits described in panels A-C. The voltage sensitivities of late phase τ were fitted with single exponential decays for all three channels (solid lines). For panels D-I, data shown are mean ± s.e.m. (n = 9 for each).

Kinetic Properties	**jShaw1**	**mK$_v$3.1**	**mK$_v$3.2**
Time to threshold	0.047/ 0.067/1.47	0.283/ 0.069/1.48	0.147/ 0.078/1.48
0-10% rise time	0.025/ 0.039/0.062	0.111/ 0.024/0.076	0.197/ 0.016/0.053
10-90% rise time	5.682/ 0.041/4.03	22.901/ 0.045/0.83	30.899/ 0.024/-0.68
Late phase of activation	5.025/ 0.040/3.52	11.626/ 0.051/0.39	15.990/ 0.026/4.06
	1.072/ 0.045/0.80		14.186/ 0.097/1.46
Deactivation (of conductance)	invariant	invariant	23.409/ 0.026/-0.71

Table 2-2. Voltage sensitivity of activation and deactivation kinetics for *Polyorchis penicillatus* jShaw1, *Mus musculus* K$_v$3.1, and K$_v$3.2 expressed in *X. laevis* oocytes. Kinetic analyses were performed on whole-cell currents collected by two-electrode voltage clamp. The time to threshold, 0-10% rise time, and 10-90% rise time were determined for each channel at a range of depolarizing voltages, and the resulting curves were fitted with single exponential functions. Table values separated by slashes are, in order, parameters A, b, and y0 from the fit results. The late phase of activation as well as deactivation were fitted with double exponential functions, and both sets of parameters are shown (except for the late phase of mK$_v$3.1 activation, which was fitted with a single exponential). n = 9 for all activation kinetics; n = 9 for jShaw1 and mK$_v$3.1, and n = 8 for mK$_v$3.2 deactivation kinetics.

value) but it has an incremental sensitivity to voltage comparable to $K_v3.1$, as indicated by the b parameter (0.041 compared to 0.045).

The late phase of activation for all three channels was fitted by exponential functions (Figure 2-4 A-C, red lines), producing time constants that decreased exponentially with increasing voltage (Figure 2-4 G-I). Mouse $K_v3.2$ had the longest late phase overall, while mouse $K_v3.1$ had the shortest (Figure 2-4 I). Voltage dependencies of the late phase time constants are listed in Table 2-2.

Pre-pulse Activation Kinetics

Delivering pre-pulses of increasing amplitude immediately before a step to +60 mV allowed us to compare the kinetics of the channels as they opened from initial states that occupy different points along their respective activation pathways. The C-type inactivation in jShaw1 and mouse $K_v3.1$ created a crossover in the current traces as the pre-pulse voltage was increased (Figure 2-5 A-B). Despite this, activation curves (excluding the first ms) were reasonably fitted by single exponential functions for all three channels (Figure 2-5B) that yielded time constants with differing degrees of voltage sensitivity (Figure 2-5C). The time constant for jShaw1 ranged from 1.5 to a maximum of 2.3 ms; after a small slowing in opening rate with pre-pulses between -40 and +10 mV, the opening kinetics of channels post-pulse became faster as voltage became more positive (Figure 2-5C). The opening kinetics of the mouse K_v3 channels, on the other hand, significantly slowed when the predepolarization exceeded 0 mV. The

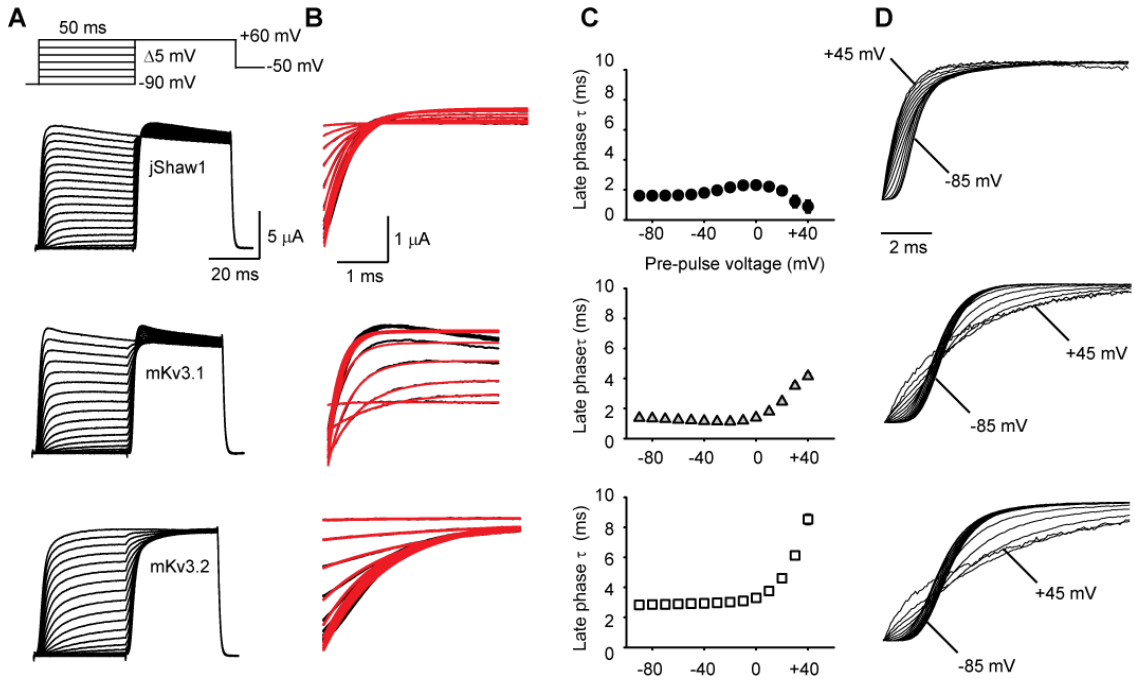

Figure 2-5. Kinetics under the influence of pre-activating pulses for jShaw1 compared to mK$_v$3.1 and mK$_v$3.2. A, The two-pulse protocol used to investigate the effects of pre-activation voltage on activation kinetics, with representative currents of the three channels expressed in *X. laevis* oocytes. The scale bars shown for jShaw1 apply to both mouse channels. B, Expanded view of currents in panel A, showing the late phase of activation during the +60 mV pulse (black lines) with single exponential fits (red lines). C, Time constants (τ) derived from single exponential fits to the late phase of activation for jShaw1 (filled circles; n = 9), mK$_v$3.1 (grey triangles; n = 9), and mK$_v$3.2 (open squares; n = 8) at various pre-depolarizing voltages. τ values above +40 mV were excluded for clarity. Data shown are mean ± s.e.m.. D, Representative full activation traces during the +60 mV pulse scaled and superimposed for jShaw1, mK$_v$3.1 and mK$_v$3.2. Traces collected after pre-depolarizations to -85 and +45 mV are indicated; traces collected above +45 mV were excluded for clarity.

rescaled traces in Figure 5D illustrate the difference between the late stages of opening kinetics in jShaw1 and the two mouse channels. Successively more positive depolarizations eliminated the delay phase in the jShaw1 traces, indicating that the later steps in channel activation are rapid, with time constants of less than 2 ms. However, for predepolarization greater than 0 mV in the mouse channels it appears that the residual activation upon depolarization to +60 mV involves a much slower transition, with time constants approaching 10 ms when the predepolarization is +45 mV.

Deactivation Kinetics

Deactivation kinetics were examined by maximally opening the channels at +60 mV then stepping to a series of more negative holding potentials, recording tail currents (Figure 2-6A), and converting them to conductance (Figure 2-6B) assuming a potassium reversal potential of -80 mV. Tail conductance traces were fitted with the sum of two exponential decays (Figure 2-6B, red lines). jShaw1 tail currents decayed more slowly than both mouse channels during the 50 ms tail step, reflected in the slow time constant that was larger than that of either mouse channel, averaging at 18.7 ms. Both jShaw1 deactivation time constants were weakly sensitive to voltage, as were those for mouse K_v3.1 (Figure 2-6C). This was not the case for mouse K_v3.2; the slow time constant for this channel rose steadily with more positive voltage, rising from 3.3 to 17.0 ms. The proportion of the two deactivation processes described by the two time constants also varied

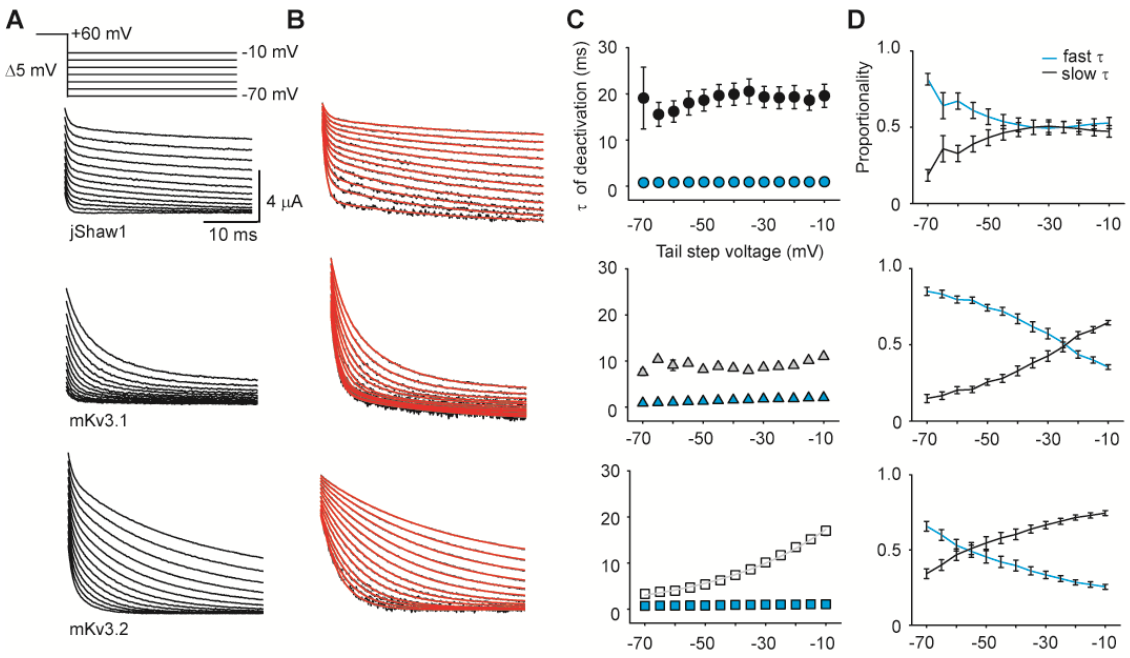

Figure 2-6. Deactivation kinetics of jShaw1, mK$_v$3.1, and mK$_v$3.2. A, Voltage protocol used to elicit tail currents from the three K$_v$3 channels expressed in *X. laevis* oocytes, with representative traces. Currents shown extend from 0.5 to 35 ms of the 50 ms tail step. Scale bars shown for jShaw1 apply to both mouse channels. B, Tail conductance, calculated by dividing current by V-V$_{RE}$V, with V equal to the tail voltage and an assumed V$_{RE}$V of -80 mV. The time course of conductance was fitted by double exponential decays for all three channels (red lines). C, Time constants (τ) of deactivation conductance at different tail step voltages for jShaw1 (circles), mK$_v$3.1 (triangles), and mK$_v$3.2 (squares). Fast τ values appear in cyan. τ values for all three channels were not fitted with exponential functions, with the exception of the mK$_v$3.2 slow tau (solid line). Axis labels for jShaw1 apply to both mouse channels. D, Proportion of conductance described by fast and slow τ values at different tail voltages. The lines connect data points and do not represent fitted functions. For panels C and D, data shown are mean s.e.m. (n = 9 for jShaw1 and mK$_v$3.1; n = 8 for mK$_v$3.2).

with voltage for all three channels (Figure 2-6D). jShaw1 deactivation conductance was dominated by the fast time constant when the tail step was between -70 and -50 mV, but at voltages positive to this, the fast and slow time constants contributed equally. Mouse K_v3.1 and K_v3.2 were each dominated by the fast time constant at the most negative tail step and dominated by the slow time constant at the most positive tail step, but the voltage at which the reversal happened was different for the two channels -25 mV for K_v3.1, -60 mV for K_v3.2.

Pharmacology

Unlike *D. melanogaster* Shaw (Wei et al., 1990), and similar to the mouse K_v3 channels tested here, jShaw1 was TEA-sensitive (Figure 2-7A). jShaw1 currents were half-blocked by 0.7 mM TEA, which was similar to the 0.3 mM and 0.7 mM of mouse K_v3.1 and K_v3.2, respectively (Figure 2-7B). For the three channels, Hill coefficients ranged from 1.0 to 1.2 (Table 2-3) suggesting a 1:1 stoichiometry of TEA to channel for each of the three channels. jShaw1 was less sensitive to 4AP, as it was only blocked by concentrations above 1 mM (Figure 2-7C). jShaw1 had a higher IC_{50} for 4AP than mouse K_v3.1 and K_v3.2, ~5 mM compared to 0.8 and 0.6 mM, respectively (Figure 2-7D). Hill coefficients ranged from 0.7 to 1.2 (Table 2-3). Our results for the mouse channels compare to previous findings as follows: we found a TEA IC_{50} for mouse K_v3.1 of 0.3 mM, 2 to 3-fold higher than the published values of 0.1 and 0.15 mM; we found a 4AP IC_{50} of 0.8 mM, 1.3 to 5-fold higher than the published values of 0.6 and 0.18 mM (Rettig et al., 1992; Yokoyama et al., 1989). For mouse K_v3.2, we found a

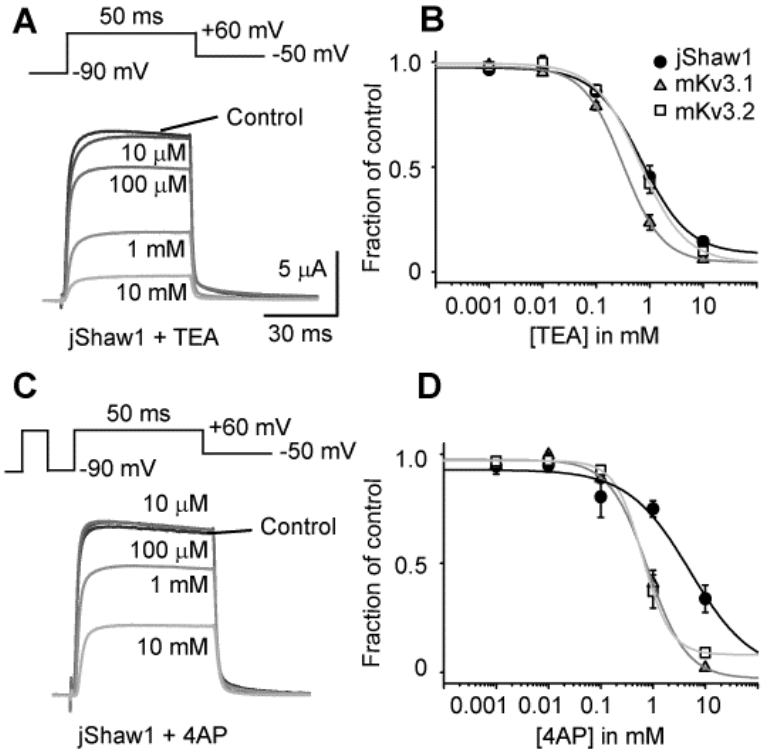

Figure 2-7. TEA- and 4AP sensitivity of jShaw1 currents. A, Concentration-dependent TEA blockade of jShaw1 currents elicited by the depicted voltage protocol, recorded from *X. laevis* oocytes expressing the channel. Traces from several cells were normalized to their own control trace and superimposed. B, Normalized concentration-effect relationship for TEA against jShaw1 compared to both mouse K_v3 channels. Lines represent the best fit of 4-parameter logistic function, and IC_{50} values were 0.7, 0.3, and 0.7 mM for jShaw1, $mK_v3.1$, and $mK_v3.2$, respectively. C, Same as A, but with 4AP. In this case, a 10 ms pre-pulse was given to open the channels and allow 4AP to access the intracellular binding site. D, Same as B, but with 4AP. IC_{50} values were 5.0. 0.8, and 0.6 mM for jShaw1, $mK_v3.1$, and $mK_v3.2$, respectively. For panels B and D, data shown are mean +/- s.e.m.. Scale bars shown apply for all traces.

Pharmacological Parameter	**jShaw1**	**Mouse K_v3.1**	**Mouse K_v3.2**
TEA IC_{50}, in mM	0.7 ± 0.1 (4-6)	0.3 ± 0.0 (5-7)	0.7 ± 0.1 (6)
TEA Hill coefficient	1.0 ± 0.1 (4-6)	1.2 ± 0.1 (5-7)	1.0 ± 0.1 (6)
4AP IC_{50}, in mM	5.0 ± 2.0 (7-15)	0.8 ± 0.1 (6)	0.6 ± 0.0 (4-6)
4AP Hill coefficient	0.7 ± 0.2 (7-15)	1.2 ± 0.3 (6)	1.6 ± 0.0 (4-6)

Table 2-3. Sensitivity of *Polyorchis penicillatus* jShaw1, *Mus musculus* K_v3.1, and K_v3.2 to TEA and 4AP. Analyses were performed on whole-cell currents collected via two-electrode voltage clamp of *X. laevis* oocytes expressing the channels. Oocytes were exposed to a single concentration of either TEA or 4AP, and data from several oocytes were averaged at each concentration. Concentration-effect curves were fitted with a logistic function to derive the IC_{50} values (the concentration at which blockage is half-maximal) and Hill coefficients (an estimate of the number of molecules binding per channel). Data are reported ± s.e.m., and numbers in parentheses represent the range of n values used to create the concentration-effect curves.

TEA IC_{50} of 0.7 mM, and the reported IC_{50} is ~1 mM; we found a 4AP IC_{50} of 0.6 mM and the published value is ~0.1 mM (Lien et al., 2002).

Discussion

Phylogenetic analysis clearly groups jShaw1 within the K_v3 family (Figure 2-1), but it has distinctions in sequence and function that help illuminate the generalized properties of K_v channels. Functionally, jShaw1 exhibits a mixture of characteristics from other K_v3 channels. The strongly negative activation threshold is reminiscent of *D. melanogaster* Shaw (Wei et al., 1990), but the fast activation is typical of mammalian K_v3 channels (Figure 2-3). Strikingly, the V_{50} values for the K_v3 channels are inversely related to the number of charges on the voltage sensor, demonstrating that the simple force generated by the interaction of the membrane potential with the charges on the voltage sensor is not the primary determinant of overall voltage sensitivity of conductance.

The specific kinetic (Figures. 4-6, Table 2-2) and pharmacological (Figure 2-7, Table 2-3) profiles of jShaw1 also differ between jShaw1, mouse $K_v3.1$ and $K_v3.2$. The characteristic times of the kinetics of jShaw1 respond differently to incremental changes in voltage, compared to the other channels, and are sensitive over a different range of absolute voltage values, indicating that the intra-molecular interactions that stabilize the kinetic intermediate conformations are substantially different between the K_v3 channels. Thus, the jShaw1 channel provides novel data on the structure/function relationships of K_v channels.

jShaw1 Activation Kinetics

The activation of jShaw1 is generally faster than mouse K_v3 channels, but the negative threshold voltage of jShaw1 complicates the interpretation of this result. Looking at panels D and E of Figure 2-4, jShaw1 appears to have faster pre-opening and early opening kinetics than the mouse channels, but since jShaw1 has such a negative threshold potential, it is possible that at the -90 mV holding potential there are more jShaw1 channels partitioned into later kinetic intermediate states than is the case for the mouse channels.

jShaw1 and the two mouse channels differ significantly in the late kinetic stages of opening. Comparison of Figure 4 panels G, H and I shows that the fast component of the late stage of jShaw1 activation is faster than that of either mouse K_v3 channel. It is possible to isolate the late stage kinetics by shifting the channels to intermediate stages of the pre-opening states with a graded set of predepolarization steps (Figure 2-5A,B). Predepolarization of jShaw1 acts to decrease the length of latency, indicating that there is a relatively slow step early in the kinetic scheme, but the traces of channel opening after the depolarizations have nearly identical shape when rescaled to a common amplitude (Figure 2-5D) and the characteristic time of opening of these late traces shows little change with increasing pre-pulse voltage. On the other hand, both of the mouse channels, when predepolarized above 0 mV, not only lack the latency, but also show a substantial change in the kinetics of the post-depolarization conductance, with the characteristic rise time increasing to ~10 ms at +45 mV predepolarization pulse.

This implies that the mouse K_v3 channels have a very slow kinetic step late in the opening process, while jShaw1 shows no sign of such a late slow step.

jShaw1 Deactivation Kinetics

All three K_v3 channels have deactivation kinetic behavior that is best modeled as the sum of two distinct exponential decays, with a rapid component that is voltage insensitive (Figure 2-6C). The slow components of jShaw1 and mouse $K_v3.1$ are also essentially voltage insensitive, so for these two channels, the voltage dependence of deactivation is a product of the relative contribution of the fast and slow processes, not the rates of the processes themselves. Mouse $K_v3.2$, however, has a voltage sensitive slow component with a characteristic time that increases with increased depolarization, so it displays substantially slower deactivation compared to the other two channels at more positive repolarization potentials (Figure 2-6B). In all three channels the contributions of the fast and slow kinetic components to the overall deactivation process are voltage sensitive (Figure 2-6D). Generally, the slow component makes a larger contribution to overall deactivation at more positive repolarization potentials. jShaw1 differs from the two mouse channels, in that the slow and fast components plateau at 50% contribution when the repolarization potential is more positive than -45 mV, whereas the slow component in both mouse channels increases continuously. These distinctive differences in the voltage sensitivity of the three different channels can be the basis for a comparative investigation of the mechanisms of channel deactivation.

jShaw1 Structure-Function Relationships

Comparing K_v channel protein sequences and electrophysiological characteristics from basal metazoans, in this case Cnidaria, to the bilateria is a useful approach for identifying regions and residues important for different elements of channel function. The quantitative and qualitative behavior of voltage-gated potassium channels is a complex function of their amino acid sequence and 3-dimensional structure. jShaw1 has sequence differences from other channels at several sites that have been proposed to play a role in specific electrophysiological behaviors.

As mentioned above, comparison of the V_{50} values (Figure 2-3; Table 2-1) for jShaw1, mouse K_v3.1, and K_v3.2 shows that in these channels the more positively charged residues in the S4 helix (Figure 2-2), the more positive the V_{50}. This counterintuitive finding indicates that the largest factor in setting the V_{50} value for the channels in this family is not the amount of charge on the voltage sensor, but rather the complex of intra-molecular interactions that determine the free energy difference between the open and closed conformations.

Both of the extracellular loops connecting core transmembrane helices (the S1-S2 loop and the S3-S4 loop) are short compared to other K_v channels, particularly the S3-S4 loop. The length of this loop has a significant effect on voltage sensitivity in the K_v1 channels (Gonzalez et al., 2000; Gonzalez et al., 2001; Mathur et al., 1997), HCN channels (Henrikson et al., 2003; Lesso and Li, 2003; Tsang et al., 2004) and L-type Ca^{++} channels (Nakai et al., 1994). It is possible that the shorter loop constrains the relative movement of the C-terminal end of the S3 helix and

the N-terminal end of the S4 helix in such a way that energetically favors an open conformation, contributing to the fact that jShaw1 has a more hyperpolarized activation curve that the two mouse K_v3 channels.

Another structural difference between jShaw1 and the mouse K_v3 channels is the presence of aspartate instead of glutamate near the C-terminal end of the S2 helix (Figure 2-2A). This residue is at one of three positions that are usually occupied by acidic residues and that form stabilizing salt bridges with the positive voltage-sensing residues of the S4 helix. In the case of jShaw1, the fact that the shorter aspartate side-chain is present at this site suggests that in the closed state the distance between the negative charge of the aspartate and positive charges of arginines in S4 will be greater than if the residue were the more typical glutamate. This would lead to less stabilization of the closed state, and thus the observed shift of equilibrium favouring the open state at less depolarizing voltages. This residue is one of those that have recently been reported to form a center for the transfer of gating charge (Tao et al., 2010). The other two residues involved in forming this complex in rat $K_v1.2$ are identical to those present in jShaw1 and form the same kind of seal around the S4 helix near the cytoplasmic surface (Figure 2-2C).

The PVP sequence that forms a hinge in the middle of the S6 helix of most K_v channels is replaced by a PIS motif in jShaw1 (Figure 2-2A). This motif is responsible for a transition between alpha-helical and 3-10 helical conformations in this region, which produces a twisting and bending motion that is required for full channel closing during inactivation (Choe and Grabe, 2009). Mutagenesis

studies on the human K_v1.1 channel have demonstrated that changing the valine residue in the PVP motif to isoleucine has large effects on both steady-state and kinetic properties of the channel (Imbrici et al., 2009), consistent with differences between the K_v1 and K_v2 family channels, which also differ at this site. The unusual replacement of PVP motif with PIS appears to be unique to the Cnidaria. Of the 180 annotated K_v3 channels in VKCDB, 9 have the PIS motif, all from cnidarians.

The slow, voltage-insensitive deactivation of jShaw1 (Figure 2-6) might be due in part to a leucine residue in the cytoplasmic end of S5 (Figure 2-2). Shieh and colleagues (Shieh et al., 1997) made chimeras of K_v2.1 and K_v3.1 and found that replacing the leucine equivalent to Shaker position L396 with phenylalanine caused faster, more voltage-dependent deactivation. jShaw1, which is slower to deactivate than both mouse channels, contains a leucine at this aligned position compared to phenylalanine in both mouse channels (Figure 2-6), supporting a role for this region in modulating deactivation kinetics.

The S4-S5 linker has also been implicated in deactivation kinetics, as it has been shown to interact with S6 residues in an adjacent subunit during the final, concerted channel opening step and the slow first step of deactivation (Batulan et al., 2010). Termed the "RELY" interaction, three residues in the S4-S5 linker (R, E, and L in Shaker) interact with a conserved Y in S6 to couple S4 movement to channel opening. In this region, jShaw1 contains a "KELY" interaction, with the arginine replaced by a similarly basic lysine. The two mouse K_v3 channels also lack the arginine but have a neutral asparagine in its place. Since the RELY

interaction stabilizes the open state, lacking this interaction may contribute to the faster deactivation kinetics and more positive activation threshold of both mouse K_v3 channels compared to jShaw1.

Our TEA inhibition data are consistent with existing structural models of blockade. MacKinnon and Yellen (MacKinnon and Yellen, 1990) pointed out Shaker residue T449 as important for external block. *D. melanogaster* Shaw has an alanine at this position and is insensitive to TEA (Wei et al., 1990). jShaw1 has a threonine here (Figure 2-2A), supporting a role for this residue in conferring sensitivity to quaternary ammonium ions. Additionally, mouse $K_v3.1$ and $K_v3.2$ contain a tyrosine at this position, and show a slightly higher TEA sensitivity than jShaw1. This is qualitatively consistent with the finding that a Shaker Y449 mutant was ~50 times more TEA-sensitive than wild-type (MacKinnon and Yellen, 1990).

Results from the 4AP experiments are consistent with sequence differences between jShaw1 and the mouse $K_v3.2$ channels. The position homologous to Shaker L396 was shown to be important in determining 4AP sensitivity (Shieh and Kirsch, 1994). Leucine was replaced with phenylalanine at this site in $K_v2.1$ and 4AP sensitivity was increased, which aligns with our result that the mouse channels contain phenylalanine and are more 4AP-sensitive than the leucine-containing jShaw1.

jShaw1 in P. penicillatus

P. penicillatus is a small hydrozoan medusa found in the near-shore areas off the entire west coast of North America. Like most jellyfish, it has three core behaviors – swimming, eating, and crumpling – that depend on the combined excitability of neurons, myocytes, and epithelial cells. The nervous system of *P. penicillatus* has been previously described (Lin et al., 2001; Spencer, 1979; Spencer and Arkett, 1984) and consists of several diffuse nerve nets coordinated by two nerve rings in the bell margin. The nerve rings are functionally divided into the inner motor center with radial projections to swimming motor neurons and an outer integrating center consisting of first- and second-order photosensory cells.

jShaw1 mRNA was isolated from bell margin tissue, but further localization methods (i.e. *in situ* hybridization and immunolocalization) will be needed to identify and quantify the expression in specific cells. However, previous electrophysiological studies on *P. penicillatus* indicate cell types that are more likely to express jShaw1 than others, with the *caveat* that our data were collected from exogenously expressed homomultimeric channels and may differ functionally from native channels, which may form heteromultimers with other subunits or interact with accessory proteins.

Taking those limitations into account, it is clear that two potassium currents isolated from cultured *P. penicillatus* swimming motor neurons do not match the biophysical characteristics of jShaw1: one was an A-type current, and the other

activated slowly (tau = 65-250 ms) with a threshold of -30 mV (Przysiezniak and Spencer, 1994). In the outer nerve ring, however, there are two types of neurons that could accommodate a channel like jShaw1. “Bursting” cells fire regular, spontaneous action potentials which increase to bursts of six when exposed to sudden darkness. Bursting neurons have a resting membrane potential of about -40 mV and action potentials lasting about 5 ms, so if jShaw1 were expressed here, a fraction of the channels would be open at all times, helping to set the membrane potential but also antagonizing incoming signals and preventing erroneous bursts. The “oscillating” system never fires action potentials, but displays a ~1 Hz fluctuation of membrane potential (Spencer and Arkett, 1984). A low-threshold channel like jShaw1 could contribute to this fluctuation, as it would be open at voltages where it could influence the resting membrane potential and prevent the cell from depolarizing to the action potential threshold.

Finally, it is possible that jShaw1 is expressed in myocytes. *P. penicillatus* muscle cells have a resting membrane potential of -70 mV, and during action potentials, the depolarization phase is 46 ms in length, while repolarization is twice as fast (Spencer, 1978). The slow AP upstroke and quick repolarization could be due to a fast non-inactivating potassium current that is active at hyperpolarized potentials – the most prominent features of jShaw1. The epithelial sheets of *P. penicillatus*, on the other hand, fire action potentials in the range of 10 ms, and have a resting membrane potential of -55 mV (Spencer, 1978). Given that jShaw1 activates faster than 10 ms, in these cells it would antagonize incoming signals or lengthen

the action potential. Thus, it is less likely that jShaw1 is expressed in epithelial sheets.

The clade to which jShaw1 belongs does not include any identified channels from *N. vectensis* (a sea anemone) (Figure 2-1), suggesting the ancestral gene from which jShaw1 is derived may be specific to the hydrozoa and absent from the anthozoa. Looking at the phylogenetic tree in its entirety, it is clear that paralogs in the K_v3 family have evolved independently in the phylum Cnidaria since the divergence from the bilateria. Moreover, our electrophysiological results demonstrate that different physiological roles for voltage-gated potassium channels have evolved independently in different phyla. In *P. penicillatus* the delayed rectifiers that activate at strongly negative membrane potentials appear to have evolved in the K_v3 lineage, whereas in the vertebrates the K_v1 family of channels have this property. Conversely, delayed rectifiers with positive thresholds evolved within the K_v1 family of *P. penicillatus* but in the K_v3 family of vertebrates. Further identification and characterization of cnidarian, along with other invertebrate and vertebrate K_v3 channels, will be needed to determine whether this role reversal is unique to *P. penicillatus* or applicable to cnidarians as a whole.

Conclusion

Of all the mammalian K_v channels, jShaw1 is evolutionarily most closely related to the K_v3 family, but has distinctively different biophysical and pharmacological properties. In mammalian neurons, high-threshold K_v3 channels are optimized to

repolarize a cell quickly after an action potential, priming the cell to fire repeatedly (Rudy et al., 1999; Shevchenko et al., 2004). K_v1 channels, on the other hand, open at more negative voltages and modulate resting membrane potential and thus excitability in general. The fact that jShaw1 is a fast-activating, low-threshold channel demonstrates clearly that the functional role of K_v channels has not been constrained to ancestral roles during evolution. Rather, in many cases, members from different phylogenetically related families have evolved to have similar functions.

Literature Cited

Arnold, K., Bordoli, L., Kopp, J. and Schwede, T. (2006). The SWISS-MODEL workspace: a web-based environment for protein structure homology modelling. *Bioinformatics* **22**, 195-201.

Ausubel, F. M., Brent, R., Kingston, R. E., Moore, D. D., Seidman, J. G., Smith, J. A. and Struhl, K. (1987). Current Protocols in Molecular Biology. New York: John Wiley & Sons.

Batulan, Z., Haddad, G. A. and Blunck, R. (2010). An intersubunit interaction between S4-S5 linker and S6 is responsible for the slow off-gating component in Shaker K channels. *The Journal of Biological Chemistry* **285**, 14005-14019.

Camacho, C., Coulouris, G., Avagyan, V., Ma, N., Papadopoulos, J., Bealer, K. and Madden, T. L. (2009). BLAST+: architecture and applications. *BMC Bioinformatics* **10**, 421.

Cartwright, T. A., Corey, M. J. and Schwalbe, R. A. (2007). Complex oligosaccharides are N-linked to Kv3 voltage-gated K+ channels in rat brain. *Biochimica et Biophysica Acta* **1770**, 666-71.

Chen, X., Wang, Q., Ni, F. and Ma, J. (2010). Structure of the full-length Shaker potassium channel Kv1.2 by normal-mode-based X-ray crystallographic refinement. *Proceedings of the National Academy of Sciences of the United States of America* **107**, 11352-7.

Choe, S. and Grabe, M. (2009). Conformational dynamics of the inner pore helix of voltage-gated potassium channels. *The Journal of Chemical Physics* **130**, 215103.

Decaen, P. G., Yarov-Yarovoy, V., Sharp, E. M., Scheuer, T. and Catterall, W. A. (2009). Sequential formation of ion pairs during activation of a sodium channel voltage sensor. *Proceedings of the National Academy of Sciences of the United States of America*. **92**, 22498-503

DeLano, W. L. (2002). The PyMol User's Manual. San Carlos, CA, USA: DeLano Scientific.

Dominguez, I., Itoh, K. and Sokol, S. Y. (1995). Role of glycogen synthase kinase 3 beta as a negative regulator of dorsoventral axis formation in Xenopus embryos. *Proceedings of the National Academy of Sciences of the United States of America* **92**, 8498-502.

Eddy, S. R. (2010). HMMER: biosequence analysis using profile hidden Markov models.

Edgar, R. C. (2004). MUSCLE: multiple sequence alignment with high accuracy and high throughput. *Nucleic Acids Research* **32**, 1792-7.

Frohman, M. A. (1994). On beyond classic RACE (rapid amplification of cDNA ends). *PCR Methods Applications* **4**, S40-58.

Gallin, W. J. and Boutet, P. A. (2010). VKCDB: voltage-gated K+ channel database updated and upgraded. *Nucleic Acids Research* **39**, D362-6.

Gonzalez, C., Rosenman, E., Bezanilla, F., Alvarez, O. and Latorre, R. (2000). Modulation of the Shaker K+ channel gating kinetics by the S3-S4 linker. *Journal of General Physiology* **115**, 193-208.

Gonzalez, C., Rosenman, E., Bezanilla, F., Alvarez, O. and Latorre, R. (2001). Periodic perturbations in Shaker K+ channel gating kinetics by deletions in the S3-S4 linker. *Proceedings of the National Academy of Sciences of the United States of America* **98**, 9617-23.

Grigoriev, N. G., Spafford, J. D., Gallin, W. J. and Spencer, A. N. (1997). Voltage sensing in jellyfish Shaker K+ channels. *Journal of Experimental Biology* **200**, 2919-26.

Grigoriev, N. G., Spafford, J. D. and Spencer, A. N. (1999). The effects of level of expression of a jellyfish Shaker potassium channel: a positive potassium feedback mechanism. *Journal of Physiology* **517 (Pt 1)**, 25-33.

Gutman, G. A., Chandy, K. G., Grissmer, S., Lazdunski, M., McKinnon, D., Pardo, L. A., Robertson, G. A., Rudy, B., Sanguinetti, M. C., Stuhmer, W. et al. (2005). International Union of Pharmacology. LIII. Nomenclature and molecular relationships of voltage-gated potassium channels. *Pharmacological Reviews* **57**, 473-508.

Harmar, A. J., Hills, R. A., Rosser, E. M., Jones, M., Buneman, O. P., Dunbar, D. R., Greenhill, S. D., Hale, V. A., Sharman, J. L., Bonner, T. I. et al. (2009). IUPHAR-DB: the IUPHAR database of G protein-coupled receptors and ion channels. *Nucleic Acids Research* **37**, D680-5.

Henrikson, C. A., Xue, T., Dong, P., Sang, D., Marban, E. and Li, R. A. (2003). Identification of a surface charged residue in the S3-S4 linker of the pacemaker (HCN) channel that influences activation gating. *Journal of Biological Chemistry* **278**, 13647-54.

Hille, B. (2001). Ionic Channels of Excitable Membranes. Sunderland, Mass.: Sinauer Associates Inc.

Huang, Q. Q., Harvey, C. M., Paterson, A. R., Cass, C. E. and Young, J. D. (1993). Functional expression of Na(+)-dependent nucleoside transport systems of rat intestine in isolated oocytes of *Xenopus laevis*. Demonstration that

rat jejunum expresses the purine-selective system N1 (cif) and a second, novel system N3 having broad specificity for purine and pyrimidine nucleosides. *Journal of Biological Chemistry* **268**, 20613-9.

Huelsenbeck, J. P. and Ronquist, F. (2001). MRBAYES: Bayesian inference of phylogenetic trees. *Bioinformatics* **17**, 754-5.

Imbrici, P., Grottesi, A., D'Adamo, M. C., Mannucci, R., Tucker, S. J. and Pessia, M. (2009). Contribution of the central hydrophobic residue in the PXP motif of voltage-dependent K+ channels to S6 flexibility and gating properties. *Channels* **3**, 39-45.

Jegla, T., Grigoriev, N., Gallin, W. J., Salkoff, L. and Spencer, A. N. (1995). Multiple Shaker potassium channels in a primitive metazoan. *Journal of Neuroscience* **15**, 7989-99.

Jegla, T. and Salkoff, L. (1997). A novel subunit for shal K+ channels radically alters activation and inactivation. *Journal of Neuroscience* **17**, 32-44.

Johnstone, D. B., Wei, A., Butler, A., Salkoff, L. and Thomas, J. H. (1997). Behavioral defects in *C. elegans* egl-36 mutants result from potassium channels shifted in voltage-dependence of activation. *Neuron* **19**, 151-64.

Klassen, T. L., Buckingham, S. D., Atherton, D. M., Dacks, J. B., Gallin, W. J. and Spencer, A. N. (2006). Atypical phenotypes from flatworm Kv3 channels. *Journal of Neurophysiology* **95**, 3035-46.

Klassen, T. L., O'Mara, M. L., Redstone, M., Spencer, A. N. and Gallin, W. J. (2008). Non-linear intramolecular interactions and voltage sensitivity of a Kv1 family potassium channel from *Polyorchis penicillatus* (Eschscholtz 1829). *Journal of Experimental Biology* **211**, 3442-53.

Lesso, H. and Li, R. A. (2003). Helical secondary structure of the external S3-S4 linker of pacemaker (HCN) channels revealed by site-dependent perturbations of activation phenotype. *Journal of Biological Chemistry* **278**, 22290-7.

Li, B. and Gallin, W. J. (2004). VKCDB: voltage-gated potassium channel database. *BMC Bioinformatics* **5**, 3.

Lin, Y.-C. J., Gallin, W. J. and Spencer, A. N. (2001). The anatomy of the nervous system of the hydrozoan jellyfish, Polyorchis penicillatus, as revealed by a monoclonal antibody. *Invertebrate Neuroscience* **4**, 65-75.

Long, S. B., Tao, X., Campbell, E. B. and Mackinnon, R. (2007). Atomic structure of a voltage-dependent K(+) channel in a lipid membrane-like environment. *Nature* **450**, 376-382.

MacKinnon, R. and Yellen, G. (1990). Mutations affecting TEA blockade and ion permeation in voltage-activated K+ channels. *Science* **250**, 276-9.

Mathur, R., Zheng, J., Yan, Y. and Sigworth, F. J. (1997). Role of the S3-S4 linker in Shaker potassium channel activation. *Journal of General Physiology* **109**, 191-9.

McCormack, T., Vega-Saenz de Miera, E. C. and Rudy, B. (1990). Molecular cloning of a member of a third class of Shaker-family K+ channel genes in mammals. *Proceedings of the National Academy of Sciences of the United States of America* **87**, 5227-31.

Miledi, R. and Parker, I. (1984). Chloride current induced by injection of calcium into *Xenopus* oocytes. *Journal of Physiology* **357**, 173-83.

Nakai, J., Adams, B. A., Imoto, K. and Beam, K. G. (1994). Critical roles of the S3 segment and S3-S4 linker of repeat I in activation of L-type calcium channels. *Proceedings of the National Academy of Sciences of the United States of America* **91**, 1014-8.

Okayama, H., Kawaichi, M., Brownstein, M., Lee, F., Yokota, T. and Arai, K. (1987). High efficiency cloning of full-length cDNA; construction and screening of cDNA expression libraries for mammalian cells. In *Methods in Enzymology*, vol. 154, pp. 3-28. New York: Academic Press.

Papazian, D. M., Shao, X. M., Seoh, S. A., Mock, A. F., Huang, Y. and Wainstock, D. H. (1995). Electrostatic interactions of S4 voltage sensor in Shaker K+ channel. *Neuron* **14**, 1293-301.

Przysiezniak, J. and Spencer, A. N. (1994). Voltage-activated potassium currents in isolated motor neurons from the jellyfish Polyorchis penicillatus. *Journal of Neurophysiology* **72**, 1010-9.

Ronquist, F. and Huelsenbeck, J. P. (2003). MrBayes 3: Bayesian phylogenetic inference under mixed models. *Bioinformatics* **19**, 1572-4.

Rudy, B., Chow, A., Lau, D., Amarillo, Y., Ozaita, A., Saganich, M., Moreno, H., Nadal, M. S., Hernandez-Pineda, R., Hernandez-Cruz, A. et al. (1999). Contributions of Kv3 channels to neuronal excitability. *Annals of the New York Academy of Sciences* **868**, 304-43.

Rudy, B. and McBain, C. J. (2001). Kv3 channels: voltage-gated K+ channels designed for high-frequency repetitive firing. *Trends in Neuroscience* **24**, 517-26.

Schow, E. V., Freites, J. A., Gogna, K., White, S. H. and Tobias, D. J. (2010). Down-state model of the voltage-sensing domain of a potassium channel. *Biophysical Journal* **98**, 2857-66.

Schroter, K. H., Ruppersberg, J. P., Wunder, F., Rettig, J., Stocker, M. and Pongs, O. (1991). Cloning and functional expression of a TEA-sensitive A-type potassium channel from rat brain. *FEBS Letters* **278**, 211-6.

Shevchenko, T., Teruyama, R. and Armstrong, W. E. (2004). High-threshold, Kv3-like potassium currents in magnocellular neurosecretory neurons and their role in spike repolarization. *Journal of Neurophysiology* **92**, 3043-3055.

Shi, G. and Trimmer, J. S. (1999). Differential asparagine-linked glycosylation of voltage-gated K+ channels in mammalian brain and in transfected cells. *Journal of Membrane Biology* **168**, 265-73.

Shieh, C. C. and Kirsch, G. E. (1994). Mutational analysis of ion conduction and drug binding sites in the inner mouth of voltage-gated K+ channels. *Biophysical Journal* **67**, 2316-25.

Shieh, C. C., Klemic, K. G. and Kirsch, G. E. (1997). Role of transmembrane segment S5 on gating of voltage-dependent K+ channels. *Journal of General Physiology* **109**, 767-78.

Silverman, W. R., Roux, B. and Papazian, D. M. (2003). Structural basis of two-stage voltage-dependent activation in K+ channels. *Proceedings of the National Academy of Sciences of the United States of America* **100**, 2935-40.

Spencer, A. N. (1978). Neurobiology of *Polyorchis*. I. Function of effector systems. *Journal of Neurobiology* **9**, 143-57.

Spencer, A. N. (1979). Neurobiology of *Polyorchis*. II. Structure of effector systems. *Journal of Neurobiology* **10**, 95-117.

Spencer, A. N. and Arkett, S. A. (1984). Radial symmetry and the organization of central neurons in a hydrozoan jellyfish. *Journal of Experimental Biology* **110**, 69-&.

Staden, R., Beal, K. F. and Bonfield, J. K. (2000). The Staden package, 1998. *Methods in Molecular Biology* **132**, 115-30.

Tao, X., Lee, A., Limapichat, W., Dougherty, D. A. and MacKinnon, R. (2010). A gating charge transfer center in voltage sensors. *Science* **328**, 67-73.

Tsang, S. Y., Lesso, H. and Li, R. A. (2004). Critical intra-linker interactions of HCN1-encoded pacemaker channels revealed by interchange of S3-S4 determinants. *Biochemical and Biophysical Research Communications* **322**, 652-8.

Tweedie, S., Ashburner, M., Falls, K., Leyland, P., McQuilton, P., Marygold, S., Millburn, G., Osumi-Sutherland, D., Schroeder, A., Seal, R. et al. (2009). FlyBase: enhancing Drosophila Gene Ontology annotations. *Nucleic Acids Research* **37**, D555-9.

Wei, A., Covarrubias, M., Butler, A., Baker, K., Pak, M. and Salkoff, L. (1990). K+ current diversity is produced by an extended gene family conserved in Drosophila and mouse. *Science* **248**, 599-603.

Yokoyama, S., Imoto, K., Kawamura, T., Higashida, H., Iwabe, N., Miyata, T. and Numa, S. (1989). Potassium channels from NG108-15 neuroblastoma-glioma hybrid cells. Primary structure and functional expression from cDNAs. *FEBS Letters* **259**, 37-42.

Chapter 3: Estimating the S3-S4 Distance in K_v1.2 with Gibbs Free Energy

Introduction

Voltage-gated potassium (K_v) channels are pore-forming, integral membrane proteins found primarily in excitable tissues like nerve and muscle (Hille, 2001). K_v channels, along with other voltage-gated proteins, are characterized by their ability to convert changes in membrane potential into useful work (Bezanilla, 2008); in the case of K_v channels, energy is transferred to open or close the ion permeation pore (Tombola et al., 2006). Understanding this process at the molecular level has been a central goal of ion channel research in the areas of neuroscience, structural biology, biophysics, and protein chemistry.

The two distinct functionalities of K_v channels, permeability and voltage-dependent gating, are reflected in their structure: each subunit has a voltage-sensing domain (VSD) which undergoes internal rearrangements in response to voltage change, and a pore domain (PD) which opens and closes under the influence of those VSD rearrangements. Four subunits assemble to form a functional channel, with the PD regions interlocking in the center to form the ion pathway and potassium selectivity filter. The surrounding VSDs each interact with the PD from an adjacent subunit (Laine et al., 2003), but are otherwise largely in contact with membrane lipids (Jiang et al., 2003b; Lee et al., 2005; Long et al., 2005). How the VSD responds to changes in voltage is the least understood aspect of K_v channels, and has been the subject of vigorous debate (Catterall, 2010; Swartz, 2004; Tombola et al., 2006).

Both K_v functional domains are comprised of multiple transmembrane helices and the linker sequences that connect them. Helices S1 through S4 define the VSD, and helices S5 through S6 make up the PD. The VSD derives its name from the S4 helix, or voltage sensor; it carries four to seven positive amino acids, depending on the particular K_v, and translocates through the electric field of the membrane to drive the opening of the channel, stabilized by negative residues in S1, S2, and S3 along the way (DeCaen et al., 2009; Papazian et al., 1995; Tao et al., 2010). Under depolarizing conditions, each VSD traverses through a number of pre-opening conformations before the whole channel undergoes a final, cooperative step which opens the pore (Hoshi et al., 1994; Schoppa and Sigworth, 1998a; Zagotta et al., 1994b). These hidden pre-opening steps have been investigated in a variety of ways, including through mathematical analysis and kinetic modeling of currents (Klemic et al., 1998; Schoppa and Sigworth, 1998a; Zagotta et al., 1994b), by the use of pharmacological agents that slow the final cooperative step (Sack and Aldrich, 2006; Sack et al., 2004), and through the strategic placement of mutations in the S4 helix (Gagnon and Bezanilla, 2010; Smith-Maxwell et al., 1998).

With the emergence of 3-dimensional maps of crystallized K_v proteins, like those of the archaebacterial channel KvAP (Jiang et al., 2003b; Lee et al., 2005) and rat K_v1.2 (Long et al., 2005), the general membrane topology of K_v channels was confirmed, and it became possible to link the multi-step kinetic models of activation to structural elements at the nanometer level. However, many of the fine atomic-level details remained unresolved in these crystal structures,

particularly in the highly mobile VSD and in the flexible inter-helical loop sequences. A normal-mode refinement of the original rat $K_v1.2$ crystal data (Chen et al., 2010) brought the loop sequences and helix residue side chains into focus, but given the unnatural conditions under which protein crystallization takes place, the question remains as to how closely the modeled loops depict a stable *in vivo* conformation and whether the transmembrane helices are in the same location as in membrane-bound channels. To address the same concerns about the VSD, various simulations have been run of the entire $K_v1.2$ crystal structure using molecular dynamics (MD) (Delemotte et al., 2011; Delemotte et al., 2010; Jogini and Roux, 2007; Khalili-Araghi et al., 2010; Treptow and Tarek, 2006; Treptow et al., 2009) and by combining MD with the ROSETTA *ab-initio* protein folding method (Bjelkmar et al., 2009; Pathak et al., 2007; Yarov-Yarovoy et al., 2006). Such models have attempted to reveal the true positioning of the S4 and surrounding helices in different functional states, but simulations of such large protein-lipid complexes are computationally expensive and thus temporally limited. Longer simulations can be achieved through steering, which restricts the freedom of certain atoms, but this adds an inherent bias to the data. The other compromise is simulating smaller regions, like isolated VSDs (Freites et al., 2006; Sands and Sansom, 2007; Schow et al., 2010; Schwaiger et al., 2011). These can be simulated for longer than half a microsecond, which is needed to fully account for the relevant protein-protein and protein-lipid interactions.

Despite these efforts, given the inherent flexibility of the VSD and the multitude of transient kinetic states suggested by mathematical models, it is still a matter of

debate which state crystallized K_v channels actually represent. Since the crystals are grown in the absence of an electrical potential and $K_v1.2$ is known to be activated and conducting at 0 mV, the published $K_v1.2$ crystal structures are assumed to represent fully activated open channels. However, a growing body of evidence suggests that, upon prolonged stimulation, K_v channel voltage sensors enter into a stable conformation that is separate from the activated and deactivated states, defined functionally as a "mode shift" and structurally as the "relaxed state" of the VSD (Haddad and Blunck, 2011; Horne et al., 2010; Villalba-Galea et al., 2008). Upon membrane depolarization, the four VSDs go from the deactivated to the activated state, followed soon after by channel opening. Data from these studies suggest that if the depolarizing signal is maintained (which generally does not occur *in vivo*), the VSD slips into a different conformation that is more energetically stable than the activated state but the channel remains open. If this is true for mouse $K_v1.2$, then the published crystal structure could represent the relaxed, rather than the activated state of the VSD.

Further evidence from inducing metallic bridges between the VSD and PD of $K_v1.2$ suggested that the position of S4 in the functional, open state may be shifted by 0.7 to 0.8 nm and rotated by 37 degrees counterclockwise compared to the S4 in the original $K_v1.2$ crystal structure (Lewis et al., 2008). In addition, MD and functional data have pointed to the S4 helix partially adopting a more extended "3_{10}" helical arrangement, rather than a typical alpha helix, during the normal activation-deactivation cycle, and collapsing into an alpha helix upon prolonged depolarization (Villalba-Galea et al., 2008). In light of this model, the

alpha-helical nature of S4 in the K_v1.2 crystal structure supports the idea that the VSD is in a relaxed, rather than fully active conformation. Interestingly, the recently published crystal structure of the bacterial sodium channel NaVAb shows the pore to be closed, and yet the voltage sensors are in a similar position as those in the K_v crystal structures (Payandeh et al., 2011). The authors suggest they have crystallized the channels at the point where all four voltage sensors are activated but the final concerted step has not yet occurred to open the pore, but a simpler explanation is that the voltage sensors in K_v crystal structures do not represent the fully active conformation, and are more akin to the real closed state or some post-activation relaxed state.

In the present study, we aimed to estimate the atomic distance between the S3 and S4 helices in K_v1.2 when it makes the transition from the resting, closed conformation to the fully activated, open state. We directly compared electrophysiological data collected on wild type K_v1.2 and versions mutated in the S3-S4 loop to MD simulations of the mutated loops in solution. We compared the changes in Gibbs free energy (ΔG), which was calculated for different conformations adopted by the loops during the simulation, and also derived experimentally from the thermodynamic properties measured from *Xenopus laevis* oocytes expressing the mutant channels. We examined the effects of loop length and character by replacing the majority of the linker with homopolymers of 2 to 10 amino acids, consisting of glutamate, glycine, proline, or serine. 33 of the planned 36 mutants expressed robust currents, providing a wide range of energetic data for comparison to MD simulations. To isolate the experimental free energies

of the loops, we engineered a TEV protease cleavage site into the K_v1.2 S3-S4 linker and cleaved the linker with the protease in channels expressed in oocytes. Calculating the free energy of the functional cleaved channel allowed us, through simple subtraction, to derive the free energy contributed by the S3-S4 linker in all other mutants. Comparing these energies to those produced by MD simulations suggested, in the end, that the relative motion of the S3 and S4 helices may be larger than that predicted by current models of the closed and open K_v1.2 channels. This supports the idea that the K_v1.2 crystal structure does not represent the fully, activated state of the VSD.

Materials and Methods

Molecular Cloning and Channel Expression

The full-length wild-type mouse K_v1.2 open reading frame (which is identical in sequence to rat K_v1.2) was amplified from a cloned mouse K_v1.2 plasmid (OpenBiosystems, Huntsville, AL, USA) with sense and antisense primers containing at least 15 base pairs of terminal K_v1.2 sequence and Xho I and Spe I sites, respectively, for restriction digestion and ligation into the *Xenopus laevis* oocyte expression vector pXT7 (Dominguez et al., 1995). After transformation into XL1-Blue *Escherichia coli*, individual colonies were picked from ampicillin selection plates and inoculated into 5 ml overnight cultures (Terrific Broth (Gannon et al., 1988) with 100 μg/ml ampicillin). Plasmid was purified from overnight cultures using a Qiagen Miniprep Kit (Qiagen, Mississauga, ON, CAN) and the full ORF was sequenced to ensure no errors were introduced by PCR. The mouse K_v1.2 plasmid was then linearized with Xba I and gel purified (Qiagen).

Capped mRNAs were transcribed *in vitro* using the mMessage mMachine T7 polymerase kit (Ambion, Austin, Texas, USA). mRNA quality was checked by gel electrophoresis and aliquots stored at -80°C.

Mutant channels were created by replacing residues A275 to A287 in the wild-type $K_v1.2$ channel with homopolymeric sequences of glutamate, glycine, proline, or serine, ranging from two to ten amino acids in length. A version of mouse $K_v1.2$ was also engineered to include a tobacco etch virus (TEV) protease recognition site (-ENLYFQ/G-) (Dougherty et al., 1989) near the C-terminal end of S3 and on the N-terminal end of the S3-S4 loop. Wild-type mouse $K_v1.2$ does not contain any TEV protease recognition sites. To add the unique TEV cut site, the loop region of wild-type mouse $K_v1.2$ was replaced with a stuffer sequence that contained two Bbs I restriction sites as inverted repeats. Digestion of the resulting plasmid with Bbs I yielded linearized plasmids with two incompatible overhang ends. Individual loop mutants were created by annealing pairs of complementary synthetic oligonucleotides to created double-stranded DNA fragments with overhanging ends that were compatible with the ends of the Bbs I-digested plasmid. The Bbs I-digested plasmid and the annealed oligonucleotide pair for each synthetic loop were ligated and transformed as described above. Plasmids were sequenced, linearized, and transcribed into mRNA as described above.

Two-Electrode Voltage Clamp Electrophysiology

Electrophysiological recordings were performed on *X. laevis* oocytes using two-electrode voltage clamp as previously described (Sand et al., 2011). Briefly, *X. laevis* ovarian lobes were surgically removed and treated with 2 mg/ml collagenase IA (Sigma-Aldrich) in modified Barth's medium (MBM; in mM: NaCl 88, KCl 1, $Ca(NO_3)_2$ 0.33, $CaCl_2$ 0.41, $MgSO_4$ 0.82, $NaHCO_3$ 2.4, HEPES 10, sodium pyruvate 2.4; supplemented with 0.1 g/L penicillin G and 0.05 g/L gentamicin sulfate; pH 7.5 with Tris base) (Huang et al., 1993) followed by a hypertonic phosphate solution (100 mM K_2PO_4, pH 6.5 with HCl) for defolliculation. Stage V-VII oocytes were cultured in MBM at 18°C before and after microinjection. Oocytes were injected with 2 to 18 nl of ~0.3 ng/nl mRNA dissolved in nuclease-free water using a Nanoject II injector (Drummond Scientific Company, Broomall, PA, USA). Injection volumes were optimized to produce between 4 and 18 μA maximal current one day post-injection, as currents larger than ~20 μA cause local distortions in membrane potential (Baumgartner et al., 1999) and because some channels have been shown to be sensitive to high extracellular [K+] (Grigoriev et al., 1999). Recordings were filtered at 1 kHz through a 4-pole Bessel filter and sampled at 10 kHz using a GeneClamp 500B amplifier (Molecular Devices, Sunnyvale, CA, USA). Pipettes had resistances ranging from 0.1 to 2 MΩ. Oocytes were bathed in ND96 (in mM: NaCl 96, KCl 2, $CaCl_2$ 1.8, $MgCl_2$ 1, HEPES 5) at room temperature during all experiments. Measurements were performed with leak subtraction using a standard P/4 protocol. Chloride currents native to *X. laevis* oocytes (Miledi and Parker, 1984) were blocked with 1 mM diisothiocyanatostilbene-2,2′-disulfonic acid (DIDS)

present in the bath solution. DIDS did not affect the amplitude or kinetics of wild-type mouse $K_v1.2$ currents or those produced by the $K_v1.2$ TEV mutant that had been treated with TEV protease (data not shown). The currents produced by the S4 mutation were also tested and were not affected by the application of DIDS to the bath solution.

Data Analysis

Steady-state opening of the channels was measured using an isochronal tail current protocol. Oocytes were held at -90 mV for 10 ms before a series of 50 ms depolarizing pulses from -80 mV to +80 mV in 2 mV steps, followed by a 50 ms step to -50 mV for outward tails and a 100 ms return to -90 mV. Tail currents were fitted with a double exponential decay function starting approximately 1 ms after the stimulus artifact:

$$I_{tail} = \left(A_1 e^{-t/\tau_1}\right) + \left(A_2 e^{-t/\tau_2}\right) + y_0 \quad (3.1)$$

where A is the maximal current (μA), t is time (ms), τ is the time constant (ms) in each of the two terms, and y_0 is a y-offset. Current values from the beginning of the fit were taken as conductance, and fitted with a fourth-order Boltzmann equation (Hodgkin and Huxley, 1952):

$$G = y_0 + \frac{G_{max}}{\left[1+e^{\frac{-(V-V_{50})}{b}}\right]^4} \quad (3.2)$$

where V is the stimulation voltage (mV), V_{50} is the half-activation voltage (mV), and b is the Boltzmann slope factor (mV). G-V curves from individual oocytes were normalized to a minimum of zero and a maximum of unity using the Boltzmann fit parameters, and re-fit with the same equation to find the half-activation voltage (V_{50}) and slope factor. Since this relation is fourth-order, the b and V_{50} values are that of single subunits. We were interested in the behavior of whole channels, so we derived the whole-channel V_{50} by solving for V in equation (3.2) when $G/G_{max} = 0.5$. For the slope factor, only the single subunit values are reported.

To compare the kinetics of activation, the 10 to 90% rise times were calculated for the step currents produced by the depolarization pulses in the isochronal tail current protocol described above. Rise times were determined using Clampfit 9.2 (Molecular Devices), ignoring the stimulus artifact.

Deactivation kinetics were investigated by first depolarizing oocytes to +60 mV for 50 ms, then immediately stepping to a range of tail voltages ranging from -70 to -10 mV (some from -120 to +40 mV) in 5 mV steps. To account for the different driving forces at the various tail steps, currents were divided by driving force, $V-V_{rev}$, to find conductance (with V_{rev} being the reversal potential for potassium). We used a value of -80 mV for V_{rev} since in all our recordings the reversal potential for K^+ ions was around -80 mV and a 5 mV change in the estimated V_{rev} had little effect on the analysis. Tail conductance excluding the

first 1 ms was fitted by the double exponential decay function in equation (3.1) above, where τ_1 and τ_2 were the time constants of each exponential term, A_1 and A_2 were their respective amplitudes, and y_0 was the y-offset.

Data were captured and analyzed using the pClamp9 suite (Molecular Devices, Sunnyvale, CA, USA) and SigmaPlot 12 (Systat Software, Inc., Point Richmond, CA, USA). Whenever possible, results from three different batches of oocytes were averaged. Statistical significance was determined when appropriate using a two-tailed Student's t-test ($\alpha = 0.05$).

Gibbs Free Energy Calculations

In reactions involving the transfer of electrical charge, like that which occurs within a K_v channel when going between closed and open conformations, the Gibbs free energy difference (in kJ/mol) is equal to $-nFV_{50}$, where n is the number of moles of electron charge, F is the Faraday constant (96458 C/mol = 96.458 (kJ/eV)/mol), and V is the electrical potential in volts at which half the channels are closed and half are open. Mouse $K_v1.2$ has a gating charge equivalent to ~13 electron charges per channel (Aggarwal and MacKinnon, 1996; Seoh et al., 1996); therefore, for those channels which did not deviate significantly in Boltzmann slope factor we found the free energy of channel opening (in kJ/mol) using the equation:

$$\Delta G_{closed \rightarrow open} = 13e_0 \cdot FV_{50} \quad (3.3)$$

where the V_{50} is the whole channel half-activation voltage (in volts) derived experimentally from equation (3.2) above. The Gibbs free energy contributions of the different S3-S4 loops during channel opening were calculated as:

$$\Delta G_{loops} = \Delta G_{closed \rightarrow open} - \Delta G_{TEV+} \quad (3.4)$$

where ΔG_{TEV+} is the difference in free energy between the open and closed states of mouse $K_v1.2$ engineered with a TEV protease cleavage site in the S3-S4 loop that has been treated with the enzyme. In using this formalism, we assumed that TEV digestion completely eliminated the energetic contribution of the loops during channel opening.

Molecular Dynamics Simulations

The free energy differences between loop conformations with various end-to-end distances were calculated from molecular dynamics simulations of the loop peptides using the Bennett acceptance ratio algorithm (Bennett, 1976), which allows for an unbiased evaluation of the free energy difference between two states of a system. Simulations were run using the GROMACS suite of programs (Hess et al., 2008). The AMBER99SB force-field was used because it has been recently shown to give better concordance with experimental measures of small peptide properties than the other commonly used force fields (Patapati and Glykos, 2011). The loop structures were solvated using the TIP4P water model in a box sufficiently large to avoid boundary effects. Sodium and chloride ions were then added to the box in amounts appropriate to a) neutralize any charges on the

peptide and b) to simulate a bulk NaCl concentration of 96 mM. The resulting system was then taken through energy minimization, and pre-equilibration in an NVT regime followed by an NPT regime. We then performed a 100 ns simulation of dynamics of each peptide in 2 fs time steps. The conformations at 10 ns intervals were recovered and used as starting points for free energy calculations. Each of the 10 starting conformations for each peptide was hydrated, neutralized and equilibrated as above, with the addition of a distance constraint between the nitrogen atom of the N-terminal residue of the peptide and carbon atom of the C-terminal residue of the peptide, with a harmonic force constant of 1000 kJ $mol^{-1}nm^{-2}$; the inter-atomic distance that is varied during the free energy simulation was varied from 0.5 to 2.6 nm in 21 even steps. Each of these models was taken through energy minimization, NVT equilibration and NPT equilibration. The resulting files were then taken through a 200 ps burn-in run before starting data collection. Each constrained version for each starting conformation was then simulated for 2 ns with dh/dl values being collected every 4 ps (this time interval was selected by performing preliminary simulations and doing an autocorrelation analysis to determine the shortest time interval that would yield independent energy results). The resulting 210 individual files containing the 501 data values for each simulation were then processed with the GROMACS g_bar (Bennett acceptance ratio) program to yield a set of values for the difference of Gibbs free energy between each of the distances simulated. These data were then summed over the distance range of 0.5 nm to 2.6 nm to yield the integrated versions of the results used in subsequent analysis. All curves were normalized to a free energy

value of zero at the minimum of each curve for the purposes of comparison. Given that K_v channels function as tetramers, the free energies and standard errors from the MD simulations were multiplied by four to directly compare them to the experimentally-derived whole channel ΔG values obtained through equation (3.3).

From the MD data, we constructed a table where every Y-value was subtracted from every other Y-value in order to determine every possible energy difference predicted by the simulation (ΔG_{MD}). From each of these values we subtracted ΔG_{loops} for that particular loop variant found through equation (3.4). We mapped the results in 3-dimensional space and extracted the contour at $\Delta G_{MD} - \Delta G_{loops} = 0$, and plotted them as a function of end-to-end distance to find the closed and open state distances that best correlated the MD and electrophysiological data. Standard errors were propagated through to the final 3-D plot, producing two semi-parallel surfaces. The two sets of contours therefore reflect the statistical boundaries of our data.

Results

In order to reach our goal of aligning the molecular dynamics simulation results with electrophysiological data, we had to first determine the energetic and kinetic changes the loops made to $K_v1.2$. All but three of the $K_v1.2$ mutated constructs expressed robust currents in *Xenopus laevis* oocytes (Figure 3-1). We were unable to produce a mutated $K_v1.2$ with ten glycine residues (G10) in place of the linker.

.Channels with S3-S4 linkers of two prolines did not produce any discernible currents, and those with five prolines conducted only at voltages above +60 mV and were excluded from further analysis. The successful 33 mutants displayed delayed-rectifier currents that varied in different respects from wild type in steady-state and kinetic properties, as described below.

Steady-State Activation

The steady-state properties of wild type mouse $K_v1.2$ and the various mutants were determined by subjecting the channels to a series of 50 ms depolarizing pulses, followed by a step to a common tail voltage of -50 mV (Figure 3-1). Using the tail current amplitude as a measure of conductance, we generated normalized conductance-voltage (G-V) curves for each channel and plotted them alongside wild type $K_v1.2$ (Figure 3-2). Changing the length and character of the S3-S4 loop shifted the midpoint of the G-V relationships left or right on the voltage axis but did not greatly affect the slope in the linear portion of the sigmoid curve.

This was confirmed by fitting the data to a fourth-order Boltzmann equation and determining the V_{50} and slope factor for each channel and performing pairwise comparisons with a Student's t-test (Figure 3-3; Table 3-1).

All loops consisting of only two residues (E2, G2, and S2) had extremely positive V_{50} values, showing shifts of +40 mV or more compared to wild type (Figure 3-3). Similarly, all of the channels with proline loops had depolarized V_{50} values,

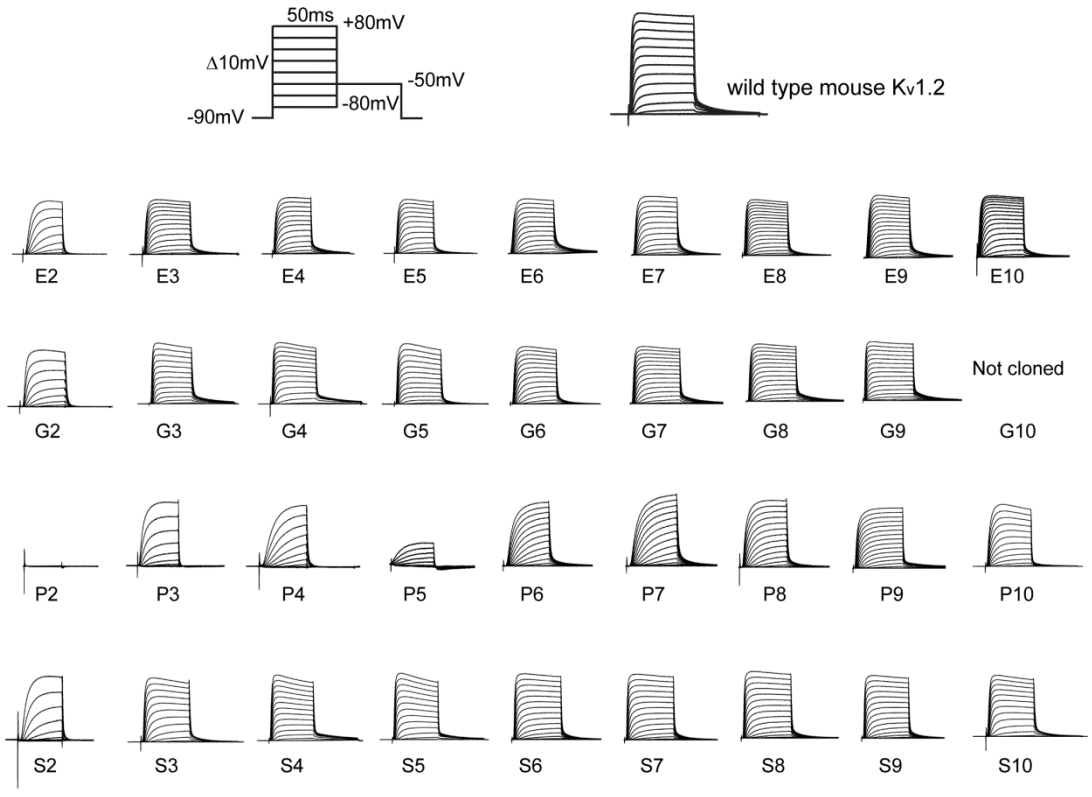

Figure 3-1. Representative two-electrode voltage clamp traces from *Xenopus laevis* oocytes expressing wild type mouse $K_v1.2$ and variants which had A275 to A287 in the S3-S4 linker replaced with stretches of 2 to 10 glutamate (E), glycine (G), proline (P), or serine (S) residues. All currents shown here except P2 and P5 reached 6 to 20 µA at the maximum stimulation voltage, and were scaled by eye to the same maximum current (wild type mouse $K_v1.2$ is enlarged for reference). The depicted voltage protocol describes what is shown, i.e. with depolarizing pulses in 10 mV increments, but pulses were actually delivered and analyzed in 2 mV steps.

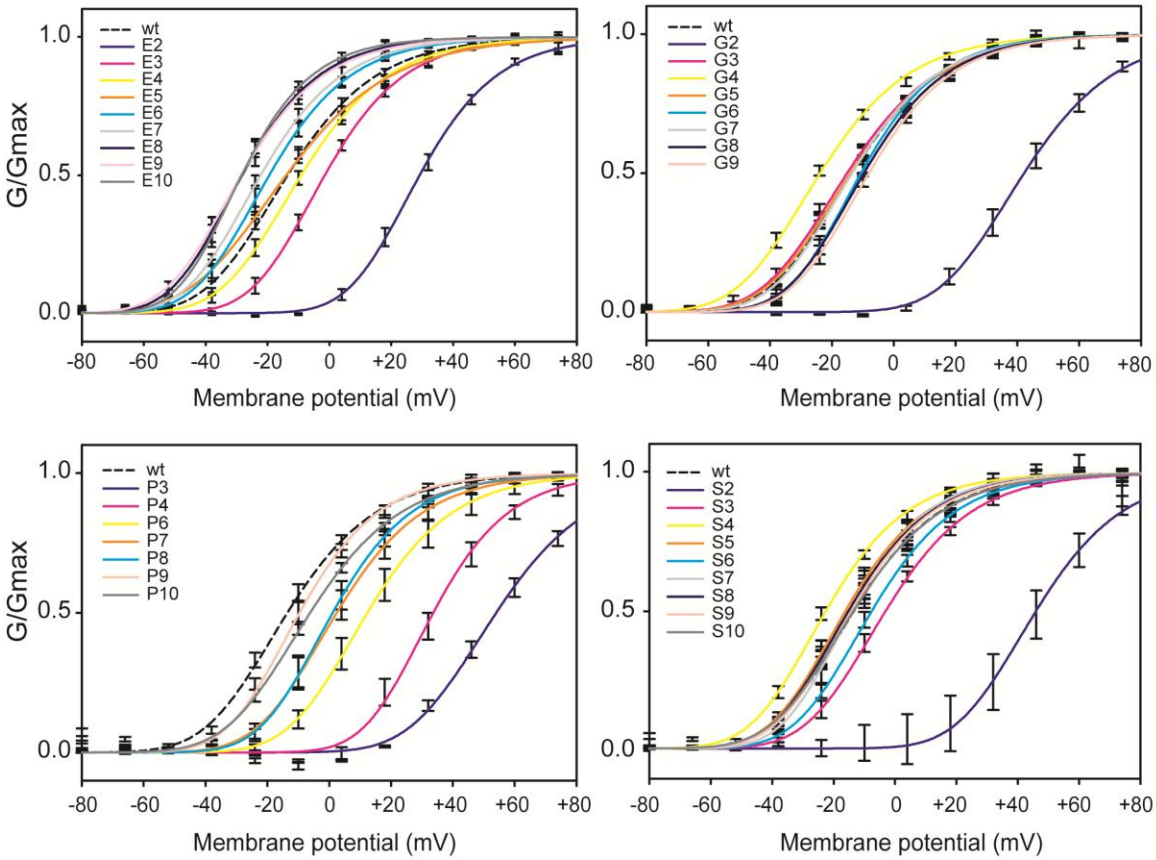

Figure 3-2. Normalized steady-state activation curves for wild type mouse $K_v1.2$ and the S3-S4 loop variants. Through Ohm's law, conductance (G) is proportional to the current divided by the driving force, which is the membrane potential minus the reversal potential for potassium. Repolarizing to a common tail voltage of -50 mV equalizes the driving force at different pulses, making G directly proportional to current. Conductance-voltage (G-V) relationships for channels with loops replaced with 2 to 10 glutamate residues are shown in the upper left; those with glycine in the upper right; those with proline in the lower left; and those with serine in the lower right. Mouse $K_v1.2$ wild type is included in every group for comparison (dashed line). For each individual experiment, G-V data were fitted to a fourth-order Boltzmann equation and normalized to the minimum (y-offset) and maximum conductance (G_{max}) for that oocyte. The resulting normalized curves were averaged across multiple oocytes, and the mean and standard error are shown here, fitted with the same fourth-order Boltzmann equation. Data were collected in 2 mV steps, but are presented every 15 mV for clarity.

although P9 was not significantly different from wild type. Of all channels, P3 had the most depolarized steady-state activation curve with a V_{50} of +54.3 +/-1.9 mV, a more than +60 mV shift compared to mouse $K_v1.2$ (Figure 3-3; Table 3-1).

There was a negative correlation between loop length and V_{50} in the glutamate and proline mutants, but to a lesser extent in glycine and serine mutants. Among all the channels, as the loops were lengthened V_{50} values became more negative, approaching and even surpassing that of the wild type channel. In particular, G4 and S4 manifested significantly hyperpolarized V_{50} values compared to wild type, around -24 and -22 mV, respectively (Figure 3-3; Table 3-1).

Of the four homopolymeric S3-S4 loop types, those consisting of glutamate produced the most negatively shifted V_{50} values, both in terms of number and magnitude. E6 through E10 had a significantly more negative V_{50} than wild type $K_v1.2$, and E8 had the most negative V_{50} of all mutants at -28.5 +/- 2.1 mV (Figure 3-3; Table 3-1).

The Boltzmann slope factor of the fitted G-V curves, a measure of the steepness of the voltage dependence, did not differ greatly between wild type and loop variants. Pairwise comparison showed that only E2, E10, P4, S2, and S7 were significantly different from mouse $K_v1.2$ (only at the 5% level, but not at the 1%). Each of these channels had a slightly reduced slope factor compared to wild type (Figure 3-3, inset).

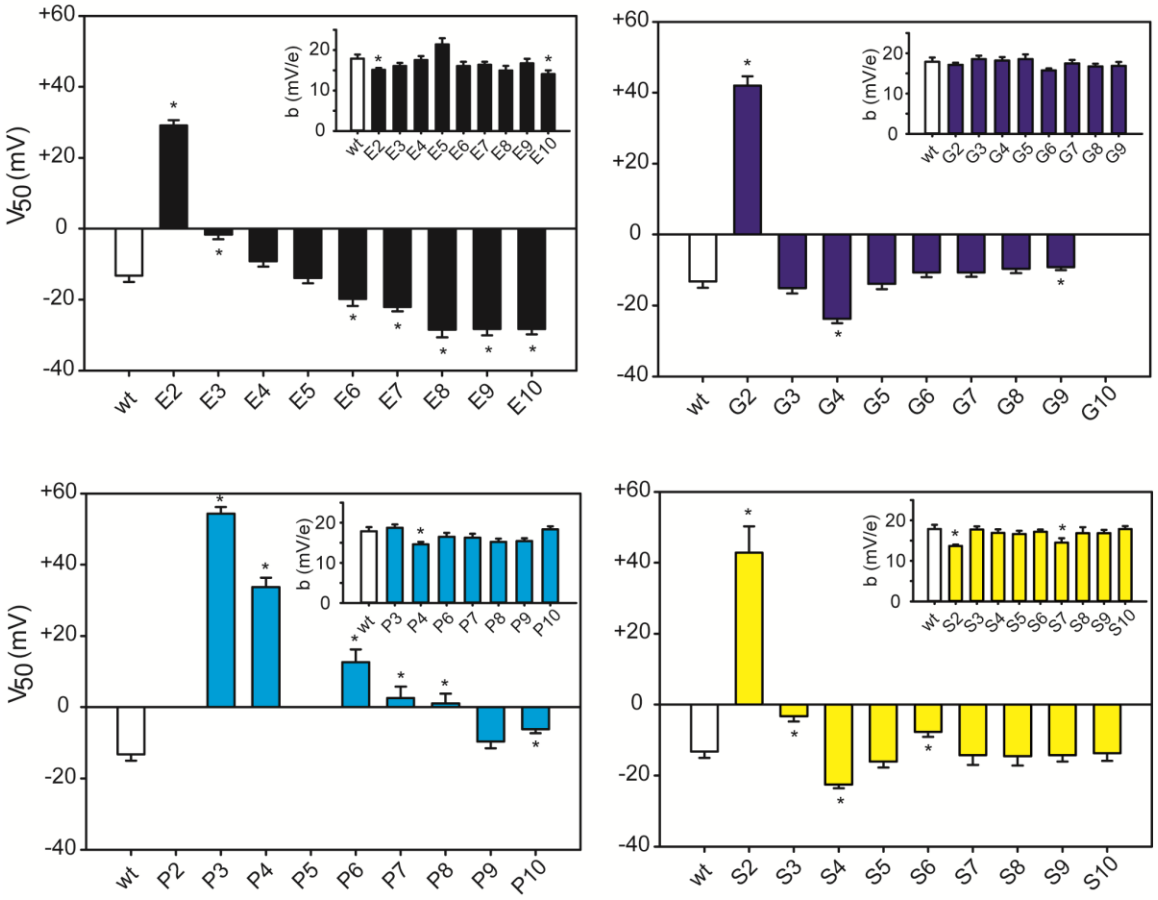

Figure 3-3. Steady-state activation parameters for wild type mouse $K_v1.2$ (white bars) and the S3-S4 loop variants. The loop was replaced with repeats of glutamate (black bars), glycine (blue bars), proline (cyan bars), or serine (yellow bars). Channels were expressed in *X. laevis* oocytes and subject to TEVC. To determine the half-activation voltage (V_{50}) and the Boltzmann slope factor (b) (inset), normalized G-V curves from tail currents were fitted to a fourth-order Boltzmann equation, as presented in Figure 3-2. V_{50} values presented here are for whole channels. All bars are shown mean + s.e.m., and asterisks denote statistical significance as determined by a two-tailed, pairwise Student's t-test (α=0.05) against wild type mouse $K_v1.2$.

	V_{50} (mV)	sem	n	p-value
Mmu1.2 wt	-13.3	1.8	8	
TEV -	-14.7	1.4	9	0.517
TEV+	-7.5	0.9	9	0.009
E2	29.1	1.5	12	0.000
E3	-1.6	1.4	9	0.000
E4	-9.2	1.5	8	0.102
E5	-13.9	1.5	7	0.783
E6	-19.8	2.0	9	0.029
E7	-22.1	1.2	9	0.001
E8	-28.5	2.1	9	0.000
E9	-28.3	1.8	5	0.000
E10	-28.3	1.5	7	0.000
G2	42.0	2.7	11	0.000
G3	-15.2	1.5	7	0.431
G4	-23.8	1.2	8	0.000
G5	-13.9	1.5	9	0.785
G6	-10.7	1.3	9	0.265
G7	-10.7	1.2	9	0.245
G8	-9.6	1.2	9	0.103
G9	-9.2	0.8	9	0.046
G10				
P2				
P3	54.3	1.9	9	0.000
P4	33.8	2.6	8	0.000
P5				
P6	12.6	3.7	6	0.000
P7	2.6	3.2	9	0.001
P8	1.1	2.8	6	0.001
P9	-9.7	1.9	9	0.189
P10	-6.1	1.1	10	0.003
S2	42.9	7.4	9	0.000
S3	-3.3	1.5	8	0.001
S4	-22.5	1.1	11	0.000
S5	-16.1	1.7	11	0.275
S6	-7.7	1.4	9	0.025
S7	-14.3	2.7	9	0.765
S8	-14.6	2.7	9	0.698
S9	-14.2	1.9	9	0.714
S10	-13.7	2.1	10	0.877

Table 3-1. Half-activation voltages (V_{50}) for wild type *Mus musculus* K_v1.2 and S3-S4 loop variants. V_{50} values (in mV) were determined from individual conductance-voltage relationships measured by TEVC on *X. laevis* oocytes expressing the channels. Normalized G-V relationships were determined by tail current analysis on individual cells. Data were fitted to a fourth-order Boltzmann equation and the V_{50} values for whole channels were calculated and averaged. Standard errors of the mean and n values are presented. To create the mutant channels, A275 to A287 of the native K_v1.2 S3-S4 linker was replaced with homopolymeric repeats of 2 to 10 glutamate (E2-E10), glycine (G2-G10), proline (P2-P10), and serine (S2-S10). G10 was not successfully cloned and P2 and P5 did not express robust currents. TEV mutants are versions of mouse K_v1.2 with an engineered TEV protease site in the S3-S4 linker. TEV- channels were not treated with the protease, while TEV+ channels were treated overnight. P-values are two-tailed, as determined by a Student's t-test.

Activation Kinetics

The time it took for currents to rise from 10 to 90% of maximum during a 50 ms depolarization served as our measure for activation kinetics. At -30 mV, just positive to the opening threshold of mouse $K_v1.2$, wild type currents took ~30 ms to rise from 10 to 90%. As the depolarizing voltage was increased, currents rose faster, with rise times decreasing exponentially. Rise times for the wild type channel reached an asymptote of 3 ms above +40 mV (Figure 3-4; Table 3-2).

The data were fitted the single exponential decay function presented in equation (3.1), and the voltage sensitivity was quantified through the inverse of the slope parameter "b." Similar to a time constant, 1/b describes the change in voltage required to reduce the 10-90% rise time to 1/e or ~37% of its initial value. Wild type mouse $K_v1.2$ needed approximately 25 mV to reduce the rise time to 37% of maximum. Mutant channel G4 was the only one to have a significantly smaller 1/b value, i.e. to have more voltage-sensitive activation kinetics than wild type. Seven channels were significantly less voltage sensitive, but most were not statistically different than wild type in voltage sensitivity (Table 3-2).

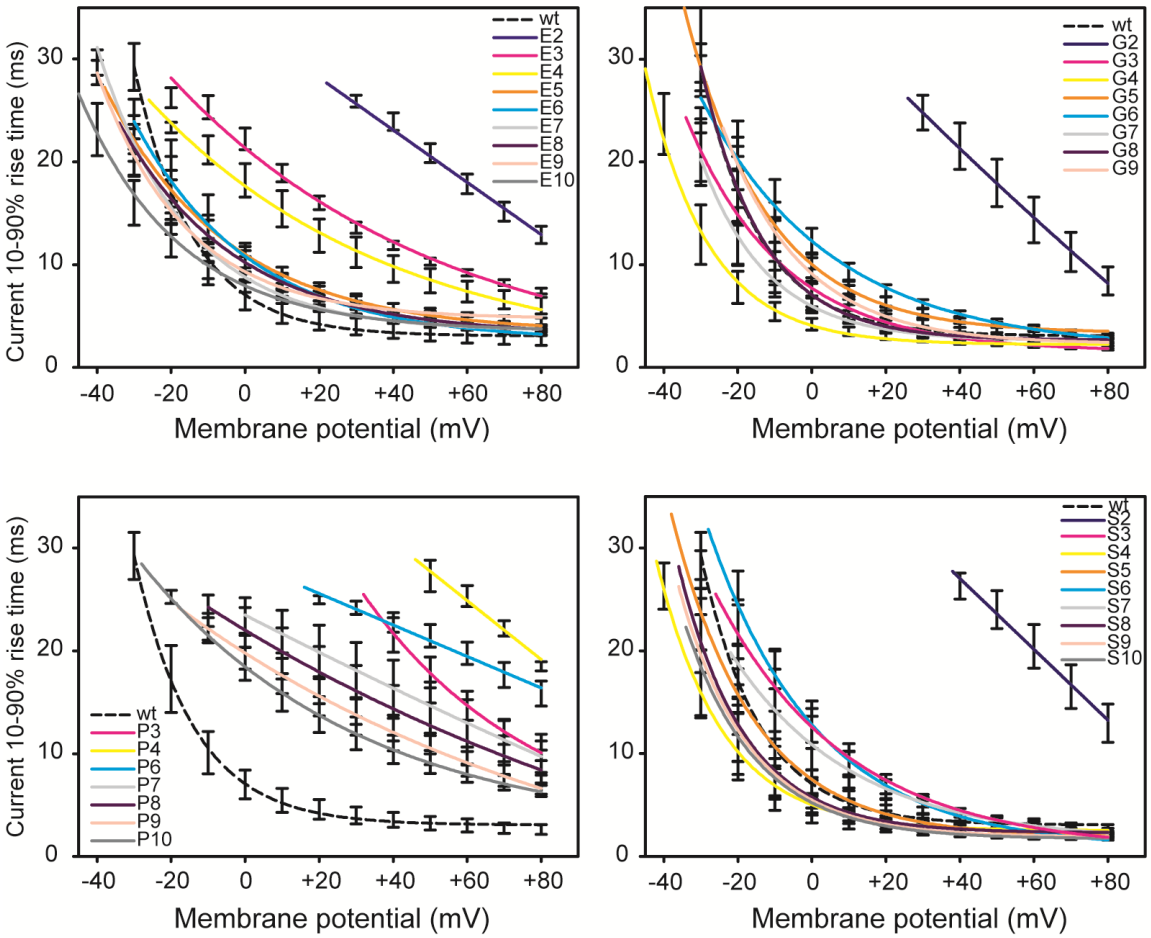

Figure 3-4. Activation kinetics of wild type mouse $K_v1.2$ and S3-S4 loop variants as a function of membrane potential. The time it took for two-electrode voltage clamp currents to rise from 10% to 90% of maximal was determined at a range of depolarizing voltages and averaged for each channel type. The mean and standard error were fitted to single exponential decay functions (solid lines) producing a slope factor that describes the voltage sensitivity of the activation kinetics. When inversed, the slope factor equals the change in voltage required to reduce the rise time to 1/e of the initial value (see Table 3-2).

	1/b (mV/e)	sem	n	p-value
Mmu1.2 wt	24.9	2.4	8	
TEV-	32.0	2.0	9	0.034
TEV+	25.1	1.1	9	0.920
E2	288119.4	56114.8	12	0.001
E3	68.9	6.1	9	0.000
E4	79.0	18.8	8	0.013
E5	32.5	4.8	7	0.161
E6	30.4	2.2	9	0.107
E7	23.3	1.4	9	0.578
E8	36.6	2.1	9	0.002
E9	26.0	3.3	5	0.787
E10	24.1	2.7	7	0.833
G2	98183.9	51131.1	11	0.123
G3	21.1	3.2	7	0.354
G4	13.9	1.8	8	0.002
G5	21.0	1.5	9	0.181
G6	31.7	2.6	9	0.077
G7	33.5	4.7	9	0.134
G8	24.1	1.7	9	0.802
G9	23.7	1.8	9	0.703
G10				
P2				
P3	9353.1	9313.1	9	0.362
P4	139158.8	24571.1	8	0.000
P5				
P6	305585.2	37919.6	6	0.000
P7	142908.7	72788.3	9	0.085
P8	25107.4	16658.9	6	0.103
P9	17142.7	17055.5	9	0.361
P10	61.9	21.6	10	0.147
S2	147323.7	33131.1	9	0.001
S3	31.3	3.5	8	0.149
S4	30.1	4.0	11	0.327
S5	25.8	1.5	11	0.744
S6	23.8	1.7	9	0.713
S7	26.3	0.9	9	0.557
S8	24.2	1.7	9	0.808
S9	23.6	1.6	9	0.663
S10	21.8	1.9	10	0.330

Table 3-2. Voltage sensitivity of activation kinetics in wild type *Mus musculus* $K_v1.2$ and S3-S4 loop variants. 1/b values, or the mV change needed to cause an e-fold decrease in 10-90% current rise time, were determined from the activation phase of individual TEVC recordings on *X. laevis* oocytes expressing the channels. The 10-90% rise time was plotted as a function of stimulating voltage and fitted with a single exponential decay function. The parameter b was inversed and averaged among several cells.. Standard errors of the mean and n values are presented. To create the mutant channels, A275 to A287 of the native $K_v1.2$ S3-S4 linker was replaced with homopolymeric repeats of 2 to 10 glutamate (E2-E10), glycine (G2-G10), proline (P2-P10), and serine (S2-S10). G10 was not successfully cloned and P2 and P5 did not express robust currents. TEV mutants are versions of mouse $K_v1.2$ with an engineered TEV protease site in the S3-S4 linker. TEV- channels were not treated with the protease, while TEV+ channels were treated overnight. P-values are two-tailed, as determined by a Student's t-test.

Taking a "snapshot" look at a single voltage helped illuminate the population of channels with slowed activation kinetics (Figure 3-5). During a pulse to +80 mV, channels with residues of 2 or those made of proline stand out prominently (Figure 3-5A). However, from the steady-state analyses it is clear that different channels are in different points of their activation curves at +80 mV. S4 channels would be fully activated, whereas there may be some P3 channels not yet open. We "normalized" this effect by looking at the 10-90% at each channel'sV_{50} voltage (Figure 3-5B). This generally served to reduce the variance in rise time, but the 2 loops and proline loops were still the most extremely shifted and significantly slower than wild type K_v1.2. There were a few other minor differences in statistical significance, but the overall pattern was similar between the two "snapshot" analyses.

Deactivation Kinetics

The behavior of channel ensembles during closing was investigated by delivering a 50 ms pulse to +60 mV, then repolarizing to tail voltages ranging from -70 to -10 mV in 5 mV steps (Figure 3-6A). We assumed a reversal potential of -80 mV to convert tail currents (Figure 3-6B) to conductance and fitted the resulting data to double exponential decay functions (Figure 3-6C), producing a fast and a slow time constant at each voltage step. In wild type mouse K_v1.2, the fast time constant was ~ 1 ms at a tail step of -50 mV (Figure 3-7A-D), and accounted for ~70% of the total deactivation rate, similar to most other channels (Figure 3-7, inset).

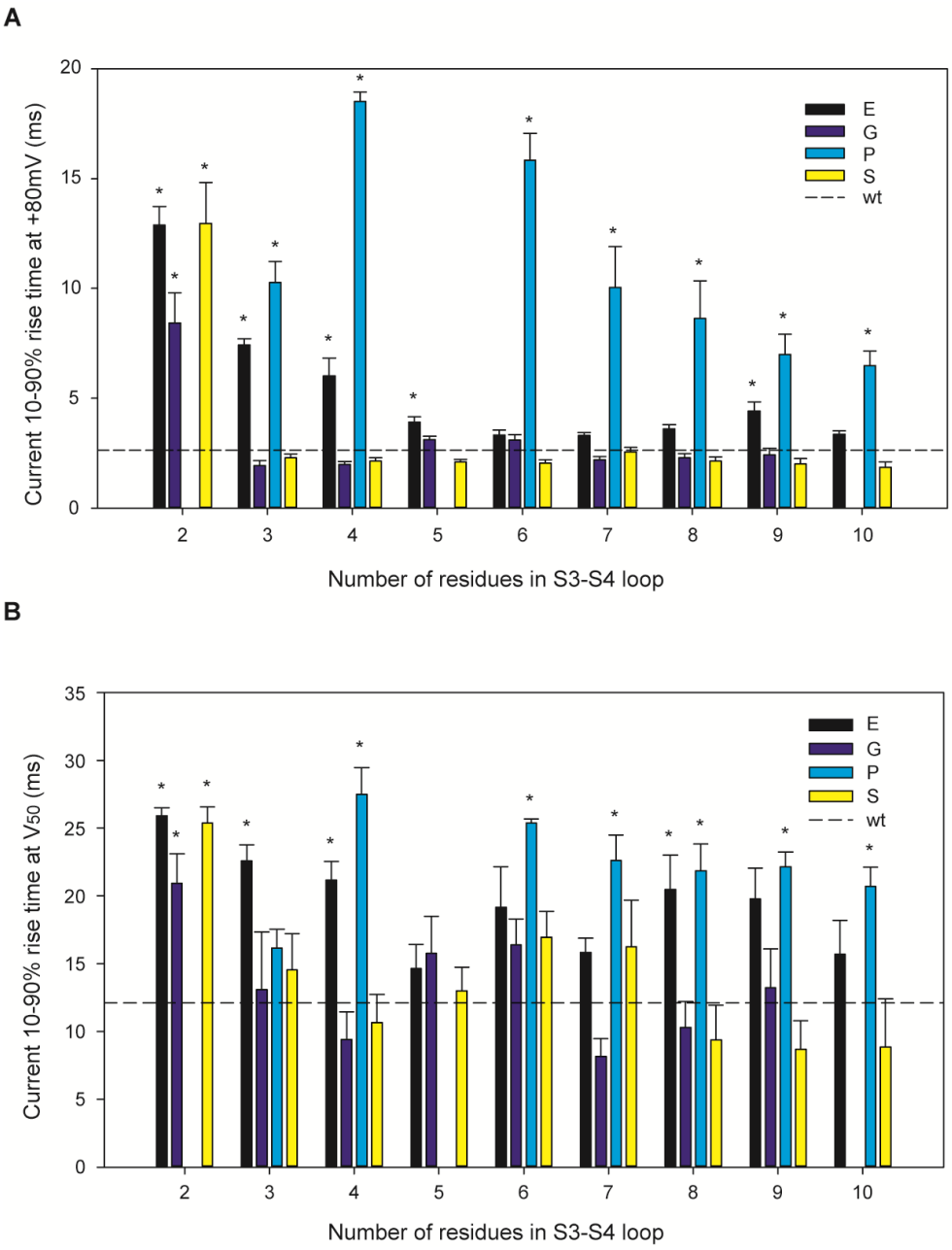

Figure 3-5. Activation kinetics of wild type mouse $K_v1.2$ and S3-S4 loop variants during currents elicited by a single voltage. A, The 10-90% rise time for currents measured during an +80 mV pulse for assorted mutated versions of mouse $K_v1.2$ with S3-S4 linkers of glutamate (black bars), glycine (blue bars), proline (cyan bars), or serine (yellow bars). The mean for wild type $K_v1.2$ was 2.6 +/- 0.5 ms (dashed line). B, The 10-90% rise time for currents measured during the voltage nearest the V_{50} of each particular channel. The mean rise time for wild type $K_v1.2$ was 12.1 +/- 2.7 ms (dashed line). For both panels, bars are shown mean + s.e.m., and asterisks denote statistical significance as determined by a two-tailed, pairwise Student's t-test (α=0.05) against wild type mouse $K_v1.2$.

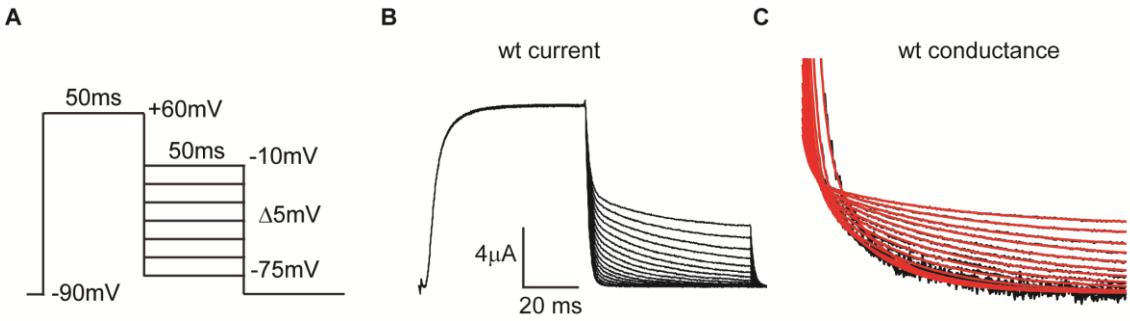

Figure 3-6. Deactivation kinetics for wild type mouse $K_v1.2$. A, The TEVC protocol used to elicit currents from oocytes expressing $K_v1.2$ and the various S3-S4 linker mutants. The oocytes were depolarized to +60 mV for 50 ms before stepping to a range of tail voltages. We were interested in the kinetics of closing at the various voltage steps. This voltage protocol was sufficient to fully open the wild type channel and most of the mutants, except those with linkers of two residues, plus P3 and P4 (see Figure 3-2). For these channels, deactivation rates may be overestimated due to some of the channels still being closed at +60 mV. B, TEVC trace from one oocyte expressing wild type mouse $K_v1.2$, stimulated with the protocol in the previous panel. This trace, like all other recordings, was collected at 10 kHz and filtered at 1kHz with leak subtraction. C, Conductance (black lines) calculated from the tail currents in the previous panel, assuming a potassium reversal potential of -80 mV. Conductance traces were fitted with double exponential decay functions (red lines), and were divided into fast and slow components. The first millisecond was ignored during fitting to avoid the stimulus artifact.

For the majority of channels, the time course of deactivation was determined largely (60-70%) by the fast time constant. The fast tau did not vary appreciably over the range of voltages for wild type mouse $K_v1.2$ or the loop variants (not shown), except those with 2 residues in the linker, which showed a positive correlation between the fast tau and voltage (i.e. at more positive tail steps, deactivation happened more slowly). Thus, they were not fitted with exponential functions like the activation time constants in the previous section (Figure 3-4). The slow time constants did vary with voltage (not shown), but the relationships were often complex and could not be fitted with polynomial or exponential functions. Since the fast tau accounted for the majority of the deactivation current kinetics in most channels (Figure 3-7, inset line graphs), we did not do any further analysis on the slow time constants. However, channels G4 and S4 were more influenced by the slow tau than the other channels, so we opted to show the values of the slow tau for these two mutants (Figure 3-7, inset bar graphs). They were significantly different than wild type mouse $K_v1.2$, but adding one more residue dropped the slow tau to values not significantly different from wild type.

Cleaving the S3-S4 Loop

The next step after determining the energetic and kinetic changes introduced by the S3-S4 loop mutations was to calculate individual loop energies for comparison to the MD simulations. To do this we used an indirect method: we enzymatically cleaved the linker of the TEV loop mutant as it was expressed in oocytes, thus producing a functional channel that had no energetic contribution

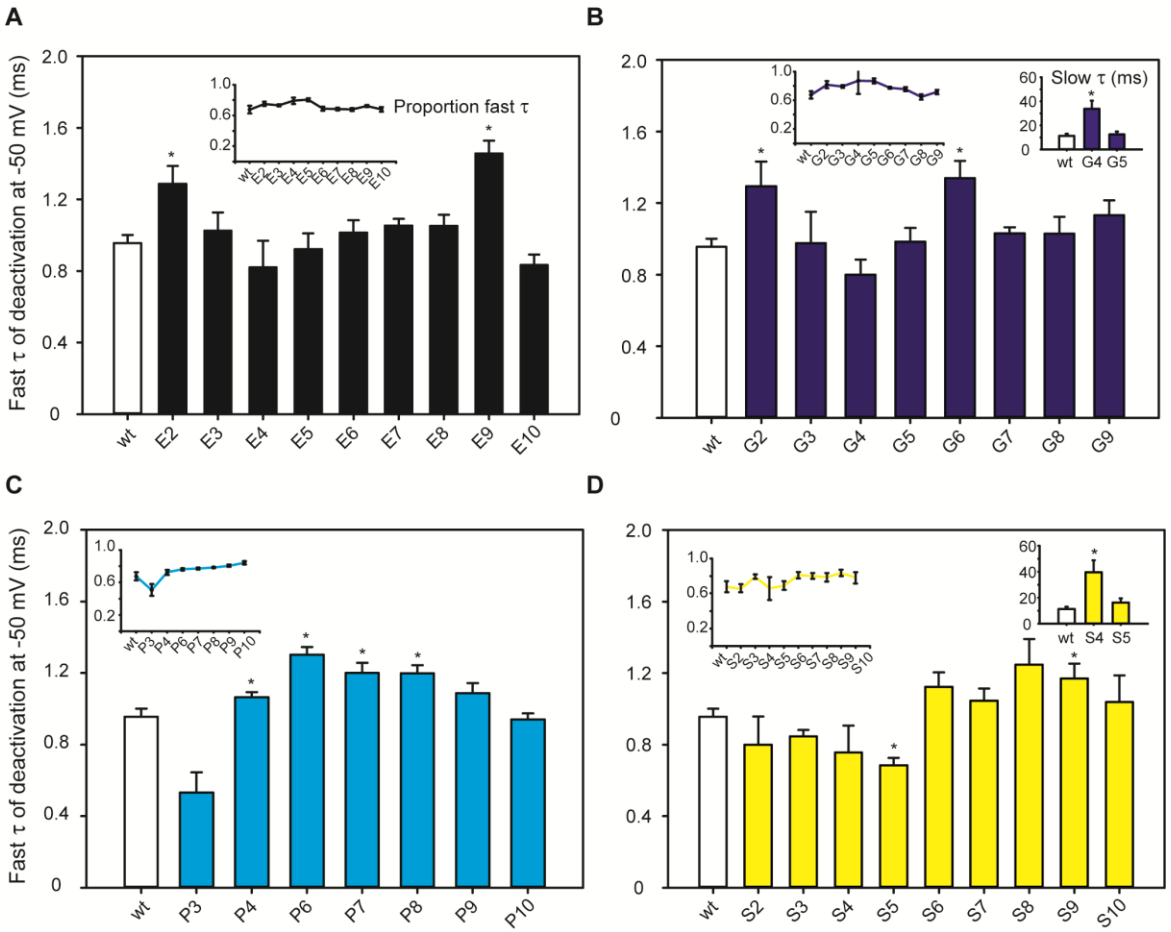

Figure 3-7. Fast component of deactivation for wild type mouse $K_v1.2$ and S3-S4 loop variants as measured from tail conductance. A-D, The fast time constant (Fast τ) is presented for wild type mouse $K_v1.2$ (white bars) and versions with linkers consisting of glutamate (black bars), glycine (blue bars), proline (cyan bars), or serine (yellow bars). Inset line graphs show, the influence of the fast component relative to the slow component in determining the time course of tail conductance, plotted for each channel at the -50 mV tail step. Channels G4 and S4 had closing rates only 50-60% determined by the fast tau. Inset bar graphs display the slow tau for G4 and S4 channels, which was ~4 times slower than wild type. All bars shown are mean + s.e.m. and asterisks denote statistical significance as determined by a two-tailed, pairwise Student's t-test (α=0.05) against wild type $K_v1.2$.

from the S3-S4 linker. Assuming that the loops function independently of the rest of the channel (i.e. they only interact with the rest of the channel through their shared peptide bonds), subtracting the ΔG of a channel without loops from the ΔG of a channel with loops should yield the contribution to the total free energy difference between the open and closed states of the channel by the loops alone (Figure 3-8). To accomplish this goal, we engineered a recognition site for TEV protease in the N-terminal region of the S3-S4 linker (Figure 3-8). TEV protease is a highly specific enzyme that cleaves under a wide range of conditions, and we expressed the "TEV" mutant channels in oocytes that were continuously exposed to the protease in solution for 18-24 hours post-injection. Two-electrode voltage clamp recordings and subsequent analysis of currents showed that TEV mutants treated with the enzyme had a significantly more positive V_{50}, at -7.5 mV ($p = 0.009$), compared to -13.3 mV for wild type $K_v1.2$ and -14.7 mV for the untreated TEV mutant channels, suggesting the protease treatment removed the linkers (Figure 3-9). The activation kinetics of digested and undigested TEV mutants were no different from wild type ($p>0.05$), but the TEV mutation did cause a significant increase in the fast tau of deactivation from ~1 ms in wild type to over 2 ms in both TEV mutants (Figure 3-10). Furthermore, in the untreated and treated TEV mutants, deactivation was largely governed by the slow time constant, which was not the case for mouse $K_v1.2$ wild type, the untreated TEV mutant (Figure 3-10), or any other loop variant (not shown).

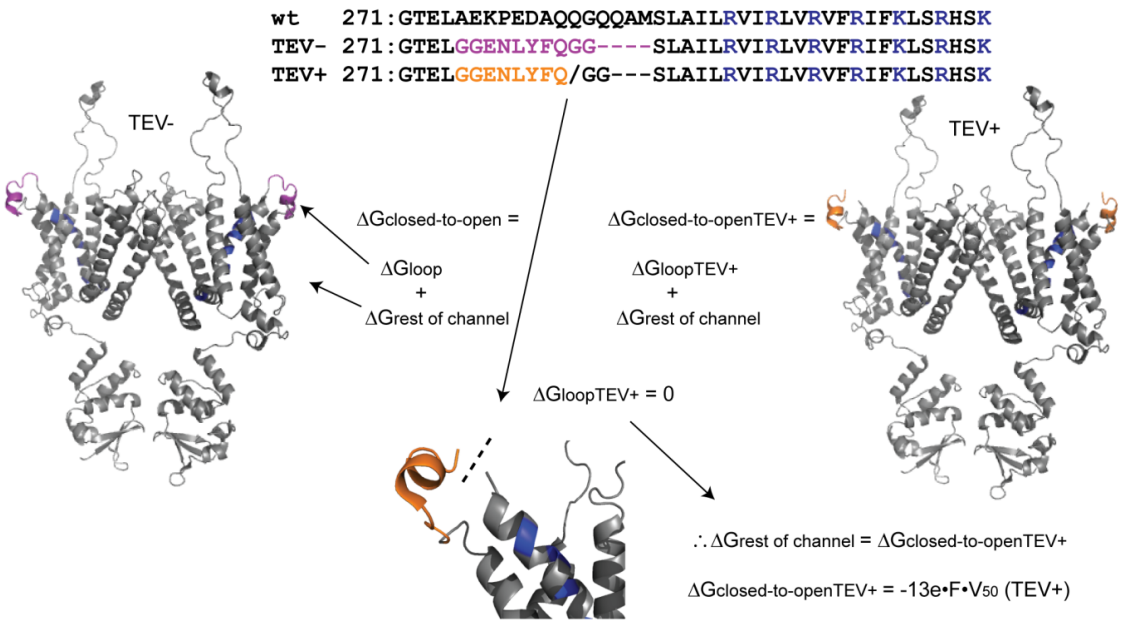

Figure 3-8. An overview of the TEV mutants and the Gibbs free energy formalism used to find the loop contribution. Versions of mouse $K_v1.2$ were engineered to contain a TEV protease sites in the S3-S4 linker, as shown in purple (uncleaved) and orange (cleaved). The free energy of an entire channel ($\Delta G_{closed\ to\ open}$) can be broken down into the free energy of the S3-S4 loops (ΔG_{loops}), and that of the rest of the channel ($\Delta G_{rest\ of\ the\ channel}$). We eliminated ΔG_{loops} by enzymatically cleaving the loops with TEV protease, and therefore the $\Delta G_{closed\ to\ open}$ in the TEV+ channel is equal to $\Delta G_{rest\ of\ the\ channel}$. This value can be taken to be the same in all the other mutants, as they are identical in sequence aside from the loop The molecular models displayed are that of rat $K_v1.2$ (3LUT; Chen et al., 2010), which is identical in sequence to mouse $K_v1.2$. All side chains and two subunits were removed for clarity. In both models the seven basic residues of S4 are indicated in blue.

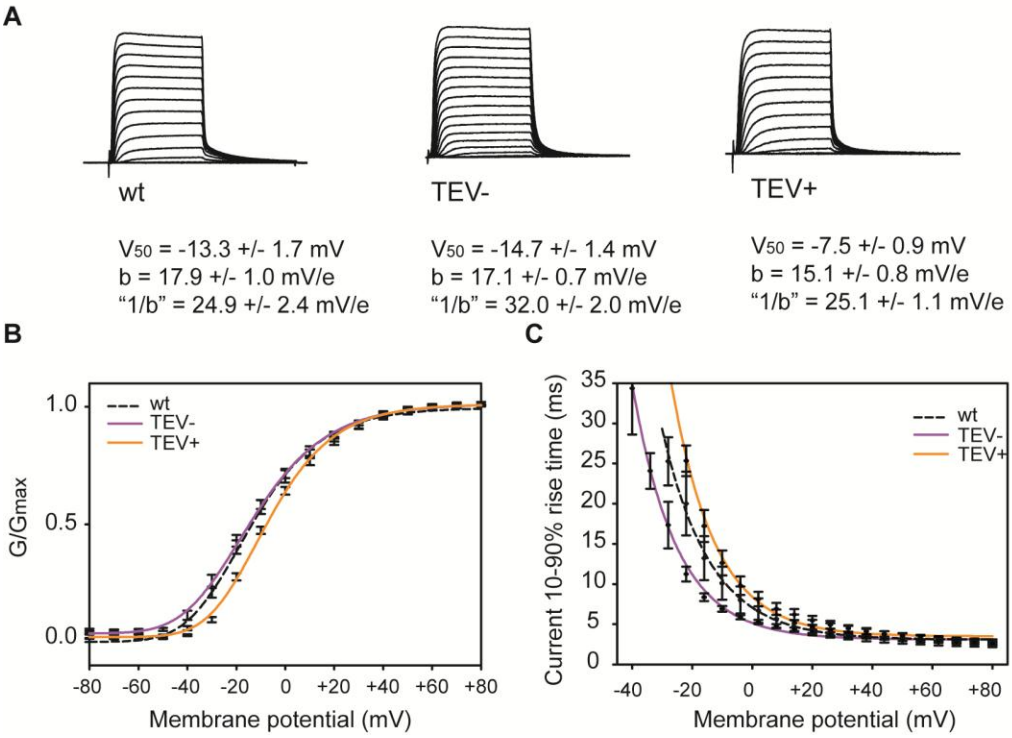

Figure 3-9. Activation properties of the mouse $K_v1.2$ TEV mutant channel both untreated and treated with TEV protease. A, Representative two-electrode voltage clamp currents elicited under the same conditions as those previously described (see Figure 3-1). The channel half-activation voltage and Boltzmann slope factor (b, for single subunits, in mV/e-fold change in steady-state conductance) are listed, as well as the voltage sensitivity of the activation kinetics ("1/b", in mV/e-fold drop in rise time). B, Normalized conductance-voltage relationships, averaged and fitted with fourth-order Boltzmann equations. Data points are shown +/- s.e.m.. C, 10-90% rise time of currents measured at a range of stimulating voltages and fitted to single exponential decays. Data shown are +/- s.e.m..

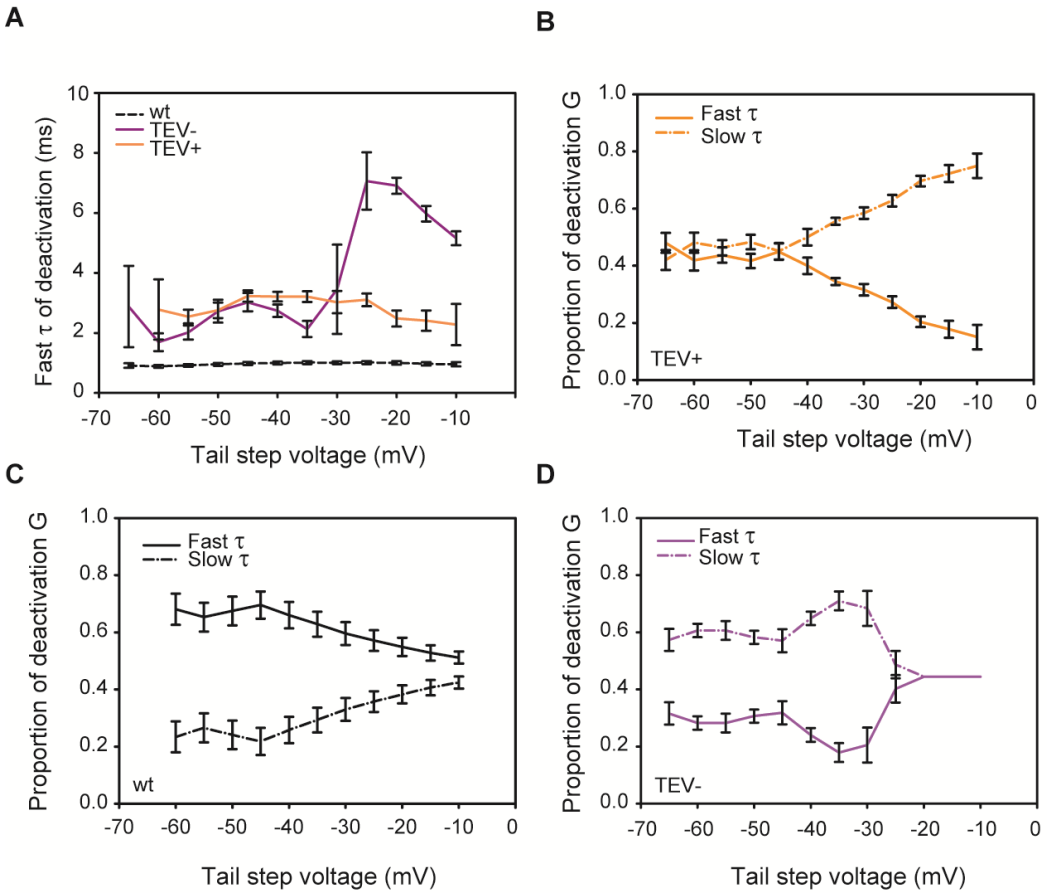

Figure 3-10. Deactivation of the mouse $K_v1.2$ TEV mutant channel both untreated and treated with TEV protease. Tail conductance at a range of voltages was fitted to a double exponential decay, producing a fast and slow time constant that contributed unequally to the total tail conductance. A, Fast time constant of deactivation (in ms) as a function of tail step voltage (in mV). The wild type channel (black dashed line) had a fast tau that was relatively insensitive to voltage and hovered around 1 ms. Replacing a portion of the S3-S4 linker with a TEV protease recognition site slowed the fast tau by 2 to 8 times, depending on the tail voltage (TEV-, solid purple line). Cleaving the loop abolished the most severe effects on the fast tau (TEV+, solid orange line) but did not restore wild type deactivation kinetics. B, The proportion of the tail conductance described by the fast and slow time constants in TEV channels treated with the protease. The two time constants contribute relatively equally at voltages where deactivation is complete (negative to -40 mV). C and D, Same as panel B, but with wild type and channels not treated with TEV protease. Over the entire range of tail voltages, wild type $K_v1.2$ deactivation kinetics are mostly determined by the fast time constant, whereas untreated TEV channels are mostly determined by the slow time constant. Data are shown +/- s.e.m. and lines do not represent fitted functions.

Molecular Dynamics Simulations

Simulating individual, untethered loops in water and determining the Gibbs free energy (kJ/mol) as a function of loop end-to-end distance produced concave curves with a single minimum for wild type mouse $K_v1.2$ and each of the S3-S4 loop variants (Figure 3-11). Many of the energy profiles of the loop variants differed from wild type $K_v1.2$ in both the position along the x-axis and the steepness of the curves. Loops of two and three residues, as well as proline homopolymers, showed the most steep free energy profiles while glycine loops produced energy profiles shallower than wild type.

Two important pieces of information were gleaned from these energy profiles. First, for each loop there was one end-to-end distance that was most energetically favored over the others during the course of the simulation. Since each curve was normalized to its own free energy minimum, the most energetically stable distance corresponded to the distance on the x-axis at the minimum of the curve. We compared these favored end-to-end distances to the V_{50} values for each loop type to see which distances led to more negatively- or positively-shifted steady state activation (Table 3-3). The most notable result was that loops most stable at or near 1.3 nm, the predicted distance between S3 and S4 in the open state, caused positive shifts to the V_{50} of mouse $K_v1.2$. Loops G2, S2, S3, and S9 all had distances of minimum free energy between 1.23 and 1.34 nm. The 3LUT model shows S3 and S4 to be 1.37 nm apart. Channel S9 was the outlier of this group, as it did not have a V_{50} significantly different from wild type while the other three mutants caused shifts ranging from +10 to +50 mV. Channels with V_{50} values

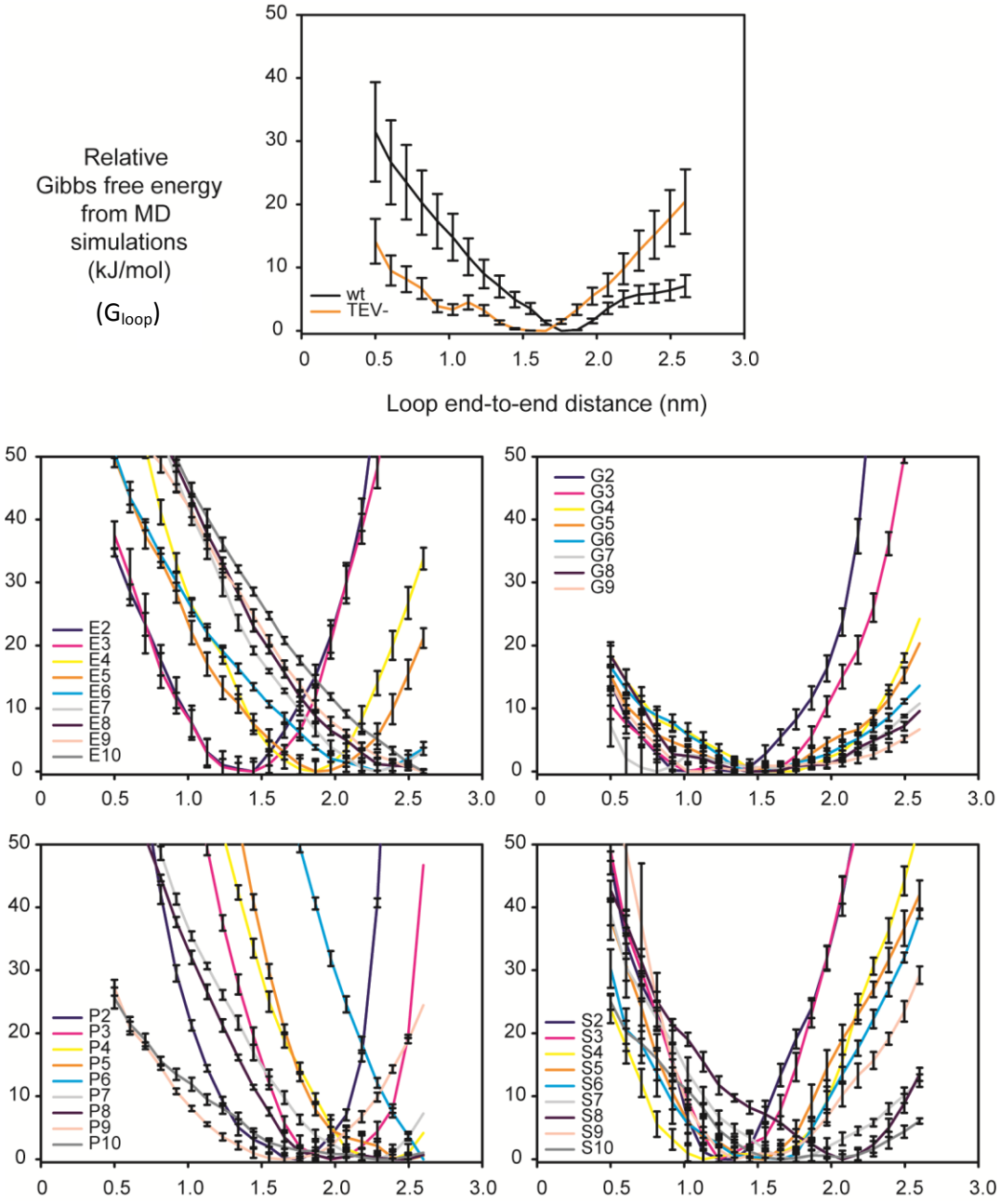

Figure 3-11. The relative Gibbs free energy of simulated $K_v1.2$ S3-S4 loop sequences as a function of end-to-end distance. The simulated loops included the wild type $K_v1.2$ linker, residues G271 to M288 inclusive, and a version of the linker with an engineered TEV protease site (upper panel). The homopolymeric loops had the form GTEL-x-M, where x represents repeats of 2 to 10 glutamate (E2-E10), glycine (G2-G10), proline (P2-P10), or serine (S2-S10). Loops were equilibrated before sampling the conformation in an aqueous environment at regular intervals. Relative energies were calculated using the Bennett acceptance ratio method (Bennett, 1976). Gibbs free energy values were multiplied by four to compare with energies derived from whole channels. Data are shown +/- s.e.m. and lines do not represent fitted functions.

Mutant	MD Minimum	V_{50} (mV)
G7	0.815	-10.73
G3	1.025	-15.16
S4	1.130	-22.49
G9	1.130	-9.20
S3	1.235	-3.27
S9	1.340	-14.22
G2	1.340	41.96
S2	1.340	42.89
G6	1.445	-10.73
G8	1.445	-9.63
E3	1.445	-1.62
E2	1.445	29.07
S5	1.550	-16.08
G4	1.655	-23.79
TEV	1.655	-14.75
G5	1.655	-13.89
S10	1.655	-13.71
P9	1.655	-9.68
S6	1.655	-7.66
S7	1.760	-14.27
Mmu1.2 wt	1.760	-13.25
E5	1.865	-13.91
E4	1.865	-9.17
P3	1.970	54.28
S8	2.075	-14.55
E7	2.285	-22.08
E6	2.285	-19.77
P10	2.285	-6.14
P7	2.285	2.60
P4	2.285	33.78
P8	2.495	1.06
E8	2.600	-28.46
E9	2.600	-28.31
E10	2.600	-28.29
P6	2.600	12.62

Table 3-3. End-to-end distances (in nm) of simulated loops that correspond to the lowest energy state, and their actual V_{50} values. The native S3-S4 linker of mouse $K_v1.2$, corresponding to residues A275 to A287, was simulated in an aqueous environment using GROMACS. Homopolymeric repeats of glutamate (E2-E10), glycine (G2-G10), proline (P2-P10), and serine (S2-S10) were also simulated, producing a free energy profile that related end-to-end distance of the loop to the relative free energy. Listed here are the end-to-end distances that were most energetically favored by each loop during the MD simulation. The homopolymeric loops were cloned into $K_v1.2$ and electrophysiologically characterized, with the half-activation voltage listed here.

significantly more negative had distances of minimum free energy most typically over 2 nm, but G4 and S4 were most stable at 1.65 and 1.13 nm, respectively (Table 3-3). Secondly, when bringing the two ends of the loop together, or pulling them away from each other, the ends go from being distance A apart to distance B apart. Distances A and B translate to x-axis coordinates on the free energy profile, with each having a corresponding y-value. The change in free energy (ΔG) associated with the loop going between those two conformations is equal to the difference on the y-axis between the two points. Thus, for every pair of end-to-end distances, a single ΔG can be calculated. However, for any single ΔG value, there are multiple pairs of distances that could have produced that difference. We calculated and compared these distances for all the channels.

S3-S4 Loop End-to-End Distances

We determined ΔG_{loop} by enzymatically cleaving the S3-S4 linker of $K_v1.2$ *in vitro* and comparing it to ΔG values for channels with intact loops (Figure 3-8; Table 3-4); the next step was to find the multiple pairs of theoretical distances that could have produced the real ΔG values for each loop. There were two related goals in this analysis. The first was to find the change in distance that most closely matched the energetic contributions of all of the loops. The second was to identify actual closed state distances and open state distances, which might vary between families of loops.

	ΔG(c->o) (kJ/mol)	sem	ΔG (loop) (kJ/mol)	sem
Mmu1.2 wt	-16.6	2.2	-7.2	2.5
TEV-	-18.5	1.8	-9.1	2.1
TEV+	-9.4	1.1	0.0	1.6
E2	36.5	1.9	45.9	2.2
E3	-2.0	1.7	7.4	2.0
E4	-11.5	1.9	-2.1	2.2
E5	-17.4	1.8	-8.0	2.1
E6	-24.8	2.5	-15.4	2.8
E7	-27.7	1.5	-18.3	1.9
E8	-35.7	2.7	-26.3	2.9
E9	-35.5	2.2	-26.1	2.5
E10	-35.5	1.8	-26.1	2.2
G2	52.6	3.3	62.0	3.5
G3	-19.0	1.8	-9.6	2.2
G4	-29.8	1.5	-20.4	1.9
G5	-17.4	1.8	-8.0	2.2
G6	-13.5	1.7	-4.0	2.0
G7	-13.5	1.5	-4.0	1.9
G8	-12.1	1.5	-2.7	1.9
G9	-11.5	1.0	-2.1	1.5
G10				
P2				
P3	68.1	2.4	77.5	2.7
P4	42.4	3.3	51.8	3.5
P5				
P6	15.8	4.6	25.2	4.7
P7	3.3	4.0	12.7	4.1
P8	1.3	3.5	10.7	3.6
P9	-12.1	2.4	-2.7	2.6
P10	-7.7	1.4	1.7	1.8
S2	53.8	9.2	63.2	9.3
S3	-4.1	1.9	5.3	2.2
S4	-28.2	1.3	-18.8	1.8
S5	-20.2	2.1	-10.8	2.4
S6	-9.6	1.8	-0.2	2.1
S7	-17.9	3.4	-8.5	3.6
S8	-18.3	3.3	-8.8	3.5
S9	-17.8	2.3	-8.4	2.6
S10	-17.2	2.7	-7.8	2.9

Table 3-4. The Gibbs free energy between closed and open states in mouse $K_v1.2$ and loop variants, and the contribution of the S3-S4 loop to this energy. The Gibbs free energy difference (in kJ/mol) between closed and open states was determined by the relation $\Delta G = -13*F*V_{50}$, with F equal to the Faraday constant, and V_{50} being the half activation voltage as measured from *X. laevis* oocytes expressing the channels. The contribution of the S3-S4 loop to this energy difference was calculated for all channels by subtracting the ΔG from the cleaved TEV channel (TEV+), which had the energetic contribution of the S3-S4 linker removed. Standard errors shown here were propagated through from the V_{50} values listed in Table 3-1.

Calculating the ΔG of the loops alone (ΔG_{loop}) from electrophysiological data produced energy values ranging from -18 to +62 kJ/mol assuming 13 units of charge per channel (Table 3-4). Our next step was to use the MD simulation G_{loop} values (Figure 3-11) to determine the most likely open and closed state distances between the S3 and S4 helices. The assumption here is that the simulated loops behave similarly to the loops in real, expressed channels, and the ΔG_{loop} values are comparable in both situations.

To find the open state and closed state distances that could have produced the ΔG_{loop} values, we took each curve from Figure 3-11 and found all possible energy differences in that curve (i.e. subtracted $y_1 - y_2$ for all pairs of x values). This produced a matrix of "simulated" ΔG_{loop} values, which we then subtracted from the experimentally derived ΔG_{loop} values from Table 3-4. The resulting parameter, ΔΔG, was plotted as a 3-dimensional surface (Figure 3-12). The x- and y-axes of the 3-D surface corresponded to closed and open state distances, respectively, while the z-axis showed the difference between simulated and electrophysiological data. We were interested in the contour of this surface at $z = 0$, the plane at which simulated energies exactly matched experimental energies (Figure 3-12A).

Since the V_{50} values used to calculate the Gibbs free energy had associated standard errors, and the data generated during the MD simulations also had standard errors, this variance had to be propagated through to the final comparisons. This meant that instead of plotting a single 3-dimensional surface for each loop, two surfaces were created. The propagated error for each data point

was added and subtracted to each point, marking the upper and lower estimates of the z-data. The plane at z = 0 was still the relevant point of comparison, but in the end each loop had two semi-parallel sets of contours, with the area between the lines representing points where simulated energies exactly matched experimental data, within statistical error (Figure 3-12B).

The most likely pairs of end-to-end distances were identified by combining the contours from many channels on a single graph and finding an area that was encompassed most completely by the contour boundaries of the different loops (Figure 3-13). To simplify matters, we grouped the contours by residue type. We did not include channels that had significantly different G-V Boltzmann slope factors compared to wild type $K_v1.2$ (i.e. channels E2, E10, P4, P8, P9, S2, and S7). The Boltzmann slope factor is not a direct measure of gating charge, but does give clues in this direction. If the gating charge is altered, equation (3.3) cannot be relied upon to produce a valid measure of Gibbs free energy. Lacking any formal calculation of gating charge in these channels, we struck them from the final contour analysis.

The glutamate channels produced the most convergent set of contours (Figure 3-13, top left), with all but E3 coming together in a region that suggests a closed state distance of 1.3 to 1.4 nm, and an open state distance between S3 and S4 of between 2.1 and 2.3 nm. Glycine mutants had a wide swath of overlapping contours on the right side of the graph, but also had a narrow region where G2,

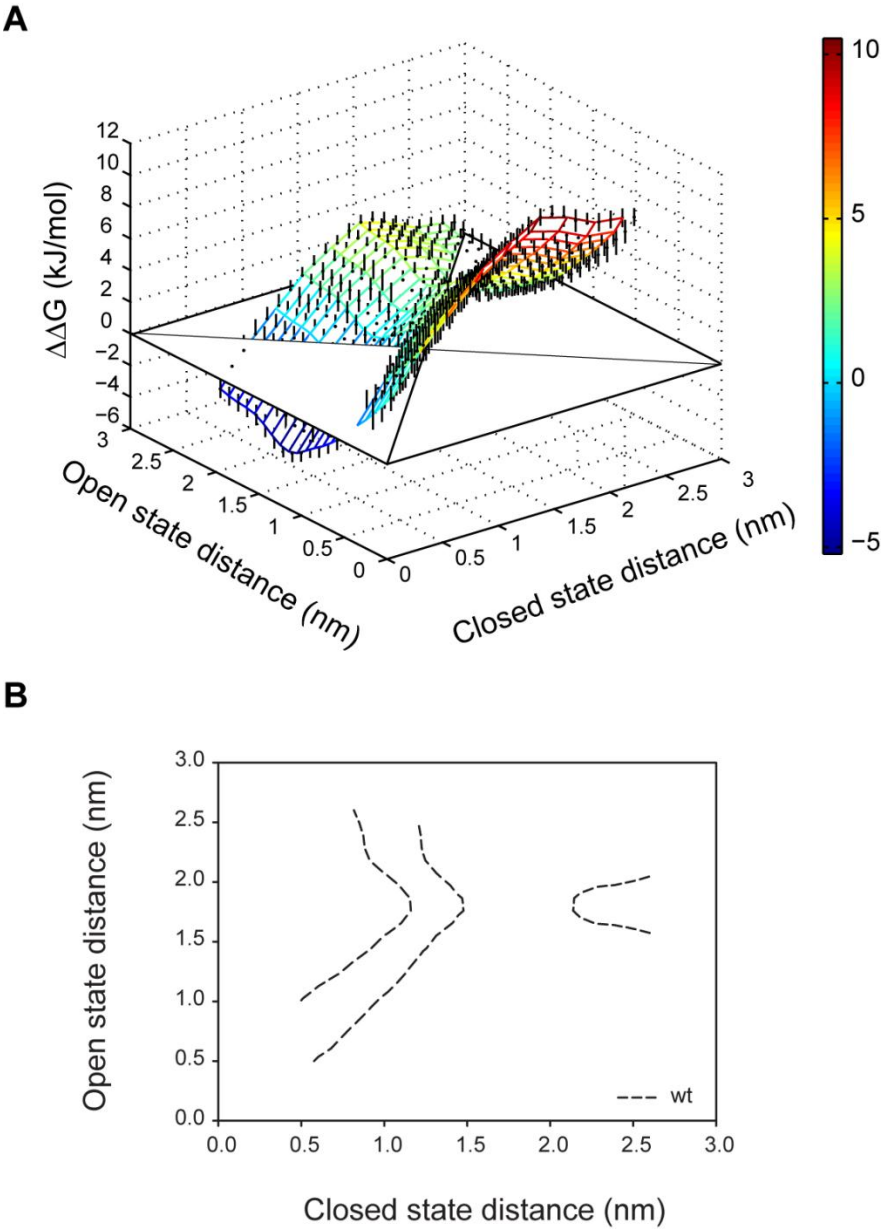

Figure 3-12. Comparison of experimentally-derived and simulation-derived Gibbs free energy values for the S3-S4 linker of wild type mouse $K_v1.2$. A, The difference in experimentally-derived and simulation-derived Gibbs free energy values for the wild type linker ($\Delta\Delta G$) as a function of the predicted open and closed state distance between S3 and S4. The simulation free energy profiles presented in Figure 3-11 were used to find every possible energy difference and the loop end-to-end distances that corresponded to them. These energy differences were subtracted from the ΔG_{loop} values listed in Table 3-4, and mapped against the corresponding end-to-end distances. The plane where z=0 defines open and closed state distances where the Gibbs free energy from experimental data matches exactly with those from the simulations. The 3-dimensional surface plot is shown with error bars that represent +/- s.e.m.. B, The plane at z=0 for the 3-dimensional $\Delta\Delta G$ surface plot presented in the previous panel. The contour lines represent points where the 3-dimesional surface plot (+/- s.e.m.) is intersected by the plane at z=0. Thus, the data points in the space between the two closest lines also represent distances where the experimentally-derived and simulation-derived energies exactly match.

G6, G8, and G9 overlapped (Figure 3-13, top right). This region predicts a closed state between 0.7 and 0.8 nm and an open state from 2.25 to 2.3 nm. The four proline channels that made it through to this analysis did not produce overlapping contours (Figure 3-13, bottom left). Serine mutants, on the other hand, produced two regions of interest (Figure 3-13, bottom right). One is a narrow zone suggesting a closed state ranging from 0.9 to 1.1 nm and an open state of 1.1 to 1.4 nm. However, there is another point of convergence that involves the contour lines from channels S3, S6, S8, S9, and S10. This point corresponds to a closed state distance of 1.1 nm and an open state distance of 1.8 nm between the S3 and S4 helices.

Discussion

The goal of this study was to compare the distances between the C-terminus of S3 and the N-terminus of S4 in the open and closed states, as predicted by structural models and as determined by molecular dynamics comparison with the electrophysiological behavior of a set of designed mutant channels. Replacing the mouse K_v1.2 S3-S4 linker with a wide range of homopolymeric linkers provided an interesting array of channels on which to base those comparisons. Before discussing these comparisons in detail, it is worth mentioning that, generally speaking, our electrophysiological results agreed well with related, previously published results from the *D. melanogaster* Shaker channel (Gonzalez et al., 2000; Gonzalez et al., 2001; Mathur et al., 1997). Similar to their results, we found that replacing the S3-S4 linker altered the steady-state and kinetic

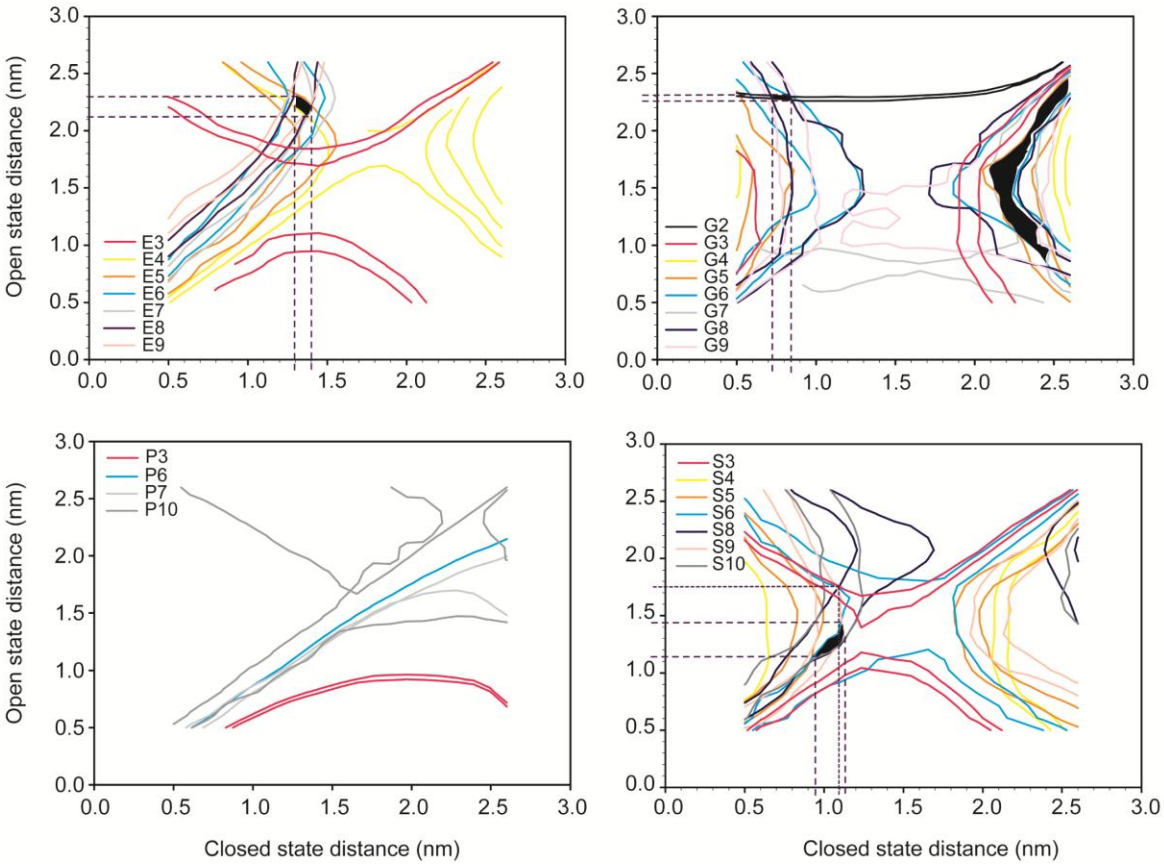

Figure 3-13. Comparison of experimentally-derived and simulation-derived Gibbs free energy values for the S3-S4 homopolymeric loops transplanted into mouse $K_v1.2$. These 2-dimensional plots represent the plane at z=0 for a 3-dimensional surface plot like that shown in Figure 3-12B, which were made for each individual loop type. The data points indicated by the contour lines (and the space between matching pairs of lines) represent pairs of end-to-end loop distances where experimental free energies exactly match up with simulated free energies. Areas on each plot that lied within the maximum number of contour boundaries are shaded in black and the corresponding open and closed state distances indicated by dashed lines.

properties of mouse $K_v1.2$ to different degrees depending on the number and character of residues in the mutated loop. They found that loops as short as three residues could restore wild-type function, and we saw this in our data in all but the proline mutants.

Glutamate Linkers Destabilize the Closed State

Mouse $K_v1.2$ channels with glutamate homopolymers in place of the S3-S4 loop displayed a striking monotonically decreasing relationship between loop length and V_{50}. These results make sense in light of the negative charge carried by glutamate residues. Under resting conditions, the oocytes expressing the channels have a negative membrane potential, meaning the interior environment is more negative than the exterior. The force on the negatively charged glutamate loops, if they fall within the transmembrane potential, would be expected to move them away from the membrane, and that force would be expected to decrease and ultimately reverse during membrane depolarization. This type of interaction would serve to destabilize the closed state in a length-dependent manner, leading to the pattern of significantly hyperpolarized V_{50} values we saw in mutants E6 through E10, but would also serve to destabilize the open state during a depolarization event. In all but one of these channels, the deactivation rates were unchanged. This suggests that the glutamate loops are not influenced by the intracellular charges in the open state. An explanation for this could be that the outward motion of S4 pushes the S3-S4 linker outside the electric field, eliminating any effects on deactivation rates.

In the one exception, E9, the fast component of deactivation was slowed by about half a millisecond, which was the most out of all the channels. This suggests that $K_v1.2$ with nine glutamate residues in the S3-S4 linker is more stable than the wild type channel in the open state. Previous studies have suggested that the S3-S4 linker at least partially adopts an alpha-helix structure (Chen et al., 2010; Gonzalez et al., 2001; Li-Smerin et al., 2000), so the increased stability conferred by a linker nine residues in length may be a function of this periodicity. Nonetheless, the combination of a destabilized closed state and stable open state would explain why E9 had the most hyperpolarized V_{50} overall.

Proline Linkers Stabilize the Closed State

In the case of proline loops, which are forced into a 75 degree pseudo-helix, restricting the dihedral bond angles of the linker backbone highly favored the closed state. V_{50} values were shifted most extremely positive and opening kinetics were most slowed in this group of channels. The longer P loops, while closer to wild type $K_v1.2$ in V_{50}, were still affected kinetically. Some even appeared to make the closing transition more difficult. Short P loops, P3 and P4, did not share this trait; they had strongly accelerated closing kinetics. The requirement that S4 be flexible agrees with some models of activation that propose, in addition to an upward motion, a rotation of the S4 helix away from the central axis of the protein in response to membrane depolarization (Lewis et al., 2008; Pathak et al, 2007; Yarov-Yarovoy et al., 2006).

Short Loops Stabilize the Closed State or Destabilize the Open State

Channels with linkers of only two residues were severely depolarized in their steady-state activation curves, and stood out in every group of channels when looking at kinetic data. The positive shift in V_{50} combined with slower activation rates indicates that the closed conformation is favored in these channels compared to wild type. In addition, the strong increase in deactivation rates indicates that the open state has been destabilized. The two effects likely combined to create the extremely positive V_{50} values in E2, G2, and S2, which were +40 to +60 mV higher than the wild type channel, and to P2, which did not activate in the voltage range we tested. Previous mutations made on the jellyfish channel jShak1 suggested that reducing the already short S3-S4 loop in this channel caused steric clashing between the two helices (Klassen et al., 2008), and this is likely what is occurring in the shortest loops tested here.

The most notable aspect of the short loops is that, during MD simulation most of them manifested the most stable at an end-to-end distance near 1.3 nm, which is the measured distance between the S3 and S4 helices in the original $K_v1.2$ crystal structure (Long et al., 2005). Of these four mutant channels, all but S9 had strongly shifted positive V_{50} values and significantly faster slow time constants of deactivation, strongly suggesting that an end-to-end distance of 1.3 nm does not represent the true open state of $K_v1.2$.

G4 and S4 Loops Stabilize the Open State

The glycine and serine groups of channels were quite similar in profile with respect to changes in V_{50} and opening and closing kinetics. In both sets, the longer loops generally did not differ from wild type in V_{50} but were slowed in deactivation kinetics, indicating a slight stabilization of the open state. The most prominent channels in these sets, however, were those with loops of four. The steady-state activation curves of G4 and S4 were shifted significantly more negative on the voltage axis compared to wild type, indicating these mutations destabilized the closed state or stabilized the open state. The drastic increase in the slow time constant of deactivation in these two channels points to the latter scenario. If the open state is highly favored, the transitions going back to the closed state would be expected to happen more slowly. These channels stood alone in the magnitude of increase in the slow tau of deactivation - when going from +60 mV to -50 mV, the slow tau rose by more than 20 ms for both of these channels. The proportion of the tail conductance described by the slow tau also increased in these channels, nearing 50% in some individual experiments, compared to the ~30% in wild type and most of the other mutant other channels. Interestingly, jShaw1, a cnidarian K_v3 channel we previously cloned and characterized (Sand et al., 2011), has a naturally short S3-S4 linker and activates ~40 mV more negative than homologous mouse K_v3 channels. It also has a slow tau of deactivation that is 15-20 ms slower than that of the mouse channels, suggesting a similar mechanism of open state stabilization in this and the G4 and S4 mutant $K_v1.2$ channels (incidentally, the most stable MD distances for G4 and

S4 loops were 1.655 nm and 1.13 nm, respectively). As mentioned above with respect to the stable open state of E9 mutants, the proposed alpha-helical structure of the S3-S4 linker (Gonzalez et al., 2001; Li-Smerin et al., 2000) could explain why loops of four, but not three or five, had a more favorable opening transition: one complete turn in an alpha helix takes approximately 3.5 amino acids, so a linker of four residues would not place any additional torsional energy to the activation process.

S4 Moves 0.6 to 1.5 nm Relative to S3 During Activation

In the original rat K_v1.2 crystal structure (PDB ID: 2A79) (Long et al., 2005) and the normal mode refinement of that data (PDB ID: 3LUT) (Chen et al., 2010), the atomic distance between the alpha-amino and alpha-carboxyl groups corresponding to the loops we replaced in this study is 1.37 nm. This is presumed to be the fully activated state, since the pore is open. The K_v1.2-2.1 "paddle chimera" (Long et al., 2007), which had the S3 and S4 of K_v2.1 on a K_v1.2 background, showed an equivalent distance of 1.52 nm. The most complete model of a closed K_v1.2 channel to date, by Pathak and others (Pathak et al., 2007), predicts a distance of 1.45 nm between S3 and S4 in the closed state. So, in these models, the distance between S3 and S4 only changes by a maximum of 0.15 nm when comparing the closed state to the open state.

Our results do not support such a modest relative motion between these two helices during channel activation. The regions of greatest overlap for glutamate and glycine mutant channel contours (Figure 3-13A, B) suggest that the S4 helix

moves 0.6 to 1.5 nm relative to S3 during activation. The results for the serine mutants were more ambiguous, but one of the two regions of convergence in this group of channels supports a 0.6 nm relative motion. Also, when looking at the molecular dynamics simulation data, loops that were stable at higher end-to-end distances often had more negative V_{50} values than wild type $K_v1.2$, supporting the notion that activation involves moving the helices apart, and in particular, that the helices are further apart in the fully activated state than they are in the closed state.

To this last point, the fact that all of the relevant regions of overlap on the contour graphs were in the upper left half of the graphs suggests that the S3 and S4 helices move apart during activation (i.e. open state > closed state). If this is true, then either the original $K_v1.2$ crystal structure does not represent the true open state of the channel, or the Pathak et al. (2007) closed model failed to accurately predict the $K_v1.2$ closed state. It is likely that both of these statements are true. This would lend support to other experimental evidence that suggests that $K_v1.2$ was crystallized in a conformation known as the "relaxed" state, which occurs after the voltage sensors have been activated for extended periods (Lewis et al., 2008; Villalba-Galea et al., 2008).

On the Structural Models of K_v Gating

Our results have bearing on the three structural models of K_v gating currently under debate. In the "paddle" model (Jiang et al., 2003a; Jiang et al., 2003b), the S3-S4 loop forms part of a modular "paddle motif" with the cytoplasmic half of

S3 (or S3b) and the charge-bearing S4 helix. The paddle in this model moves as a unit, with the S3 and S4 helices moving very little relative to each other but a great distance through the lipid bilayer, from a position parallel to the membrane in the closed state to perpendicular in the open state in the bacterial channel KvAP. In this paradigm, giving K_v1.2 shorter S3-S4 linkers would likely favor channel opening, since fewer residues would have to traverse through the inhospitable, hydrophobic bilayer during opening. Electrophysiological evidence presented here shows that this is not the case. Regarding the relative movement of S3 and S4, we have presented evidence, though not conclusive, that these two helices move apart during activation. There was one region of overlap in the serine group of mutants that could be interpreted as support for the paddle model, as the open and closed state distances are essentially equal. However, the bulk of the results presented here support the extracellular ends of these two helices moving apart from each other.

The two other structural models of K_v gating are similar, but predict different degrees of relative movement between S3 and S4 during activation. The transporter model, also called the focused field model (Ahern and Horn, 2005; Starace and Bezanilla, 2004), says that little overall S4 motion is needed to move the gating charges across the electric field of the lipid bilayer, provided the field is focused across a narrower region like an aqueous crevice. The sliding helix model (Catterall, 1986; DeCaen et al., 2009; Papazian et al., 1995; Tao et al., 2010), however, predicts that S4 slides up during activation through a successive stabilization of the gating charges by surrounding residues. This model predicts a

greater relative motion between S3 and S4. Given that the focused field model predicts an overall motion of S4 of less than 0.5 nm, our data is more in line with a sliding motion, where S3 and S4 go from about 1 nm apart in the closed state to over 2 nm apart in the fully activated conformation.

Conclusion

Through a combination of site-directed mutagenesis, molecular dynamics simulations, and free energy calculations, we have investigated the effect of altering the length and composition of the S3-S4 loop of the mouse $K_v1.2$ channel and estimated the atomic distance between the S3 and S4 helices in the closed and open states. Predicted distances from glutamate and glycine mutants point to a true closed state that resembles crystal structures of $K_v1.2$ presumed to be in the open, activated state. Our data also point to an open state where the S3 and S4 helices are more than 2 nm apart. Our data in general do not support the paddle model of gating, in that it suggests some degree of relative movement between the helices. The findings presented here are more in line with the sliding helix model, (although with some rotation of S4 included), as the distances suggested by free energy comparisons are larger than the modest S4 movements predicted in the transporter model of voltage-dependent gating. With some refinement, this type of free energy comparison could yield atomistic details of K_v channels in their native, functional state, which is useful both in validating existing structural data from model channels and in determining structure-function relationships in channels that have not been crystallized.

Literature Cited

Aggarwal, S. K. and MacKinnon, R. (1996). Contribution of the S4 segment to gating charge in the Shaker K+ channel. *Neuron* **16**, 1169-1177.

Ahern, C. A. and Horn, R. (2005). Focused electric field across the voltage sensor of potassium channels. *Neuron* **48**, 25-29.

Baumgartner, W., Islas, L. and Sigworth, F. J. (1999). Two-microelectrode voltage clamp of Xenopus oocytes: Voltage errors and compensation for local current flow. *Biophysical Journal* **77**, 1980-1991.

Bennett, C.H. (1976). Efficient estimation of free-energy differences from monte-carlo data. *Journal of Compuational Physics* **22**, 245-268.

Bezanilla, F. (2008). How membrane proteins sense voltage. *Nature Reviews Molecular Cell Biology* **9**, 323-332.

Bjelkmar, P., Niemela, P. S., Vattulainen, I. and Lindahl, E. (2009). Conformational Changes and Slow Dynamics through Microsecond Polarized Atomistic Molecular Simulation of an Integral Kv1.2 Ion Channel. *Plos Computational Biology* **5**.

Catterall, W. A. (1986). Molecular properties of voltage-sensitive sodium-channels. *Annual Review of Biochemistry* **55**, 953-985.

Catterall, W. A. (2010). Ion channel voltage sensors: structure, function, and pathophysiology. *Neuron* **67**, 915-928.

Chen, X. R., Wang, Q. H., Ni, F. Y. and Ma, J. P. (2010). Structure of the full-length Shaker potassium channel Kv1.2 by normal-mode-based X-ray crystallographic refinement. *Proceedings of the National Academy of Sciences of the United States of America* **107**, 11352-11357.

DeCaen, P. G., Yarov-Yarovoy, V., Sharp, E. M., Scheuer, T. and Catterall, W. A. (2009). Sequential formation of ion pairs during activation of a sodium channel voltage sensor. *Proceedings of the National Academy of Sciences of the United States of America* **106**, 22498-22503.

Delemotte, L., Tarek, M., Klein, M. L., Amaral, C. and Treptow, W. (2011). Intermediate states of the Kv1.2 voltage sensor from atomistic molecular dynamics simulations. *Proceedings of the National Academy of Sciences of the United States of America* **108**, 6109-6114.

Delemotte, L., Treptow, W., Klein, M. L. and Tarek, M. (2010). Effect of sensor domain mutations on the properties of voltage-gated ion channels: molecular dynamics studies of the potassium channel Kv1.2. *Biophysical Journal* **99**, L72-L74.

Dominguez, I., Itoh, K. and Sokol, S. Y. (1995). Role of glycogen-synthase kinase 3-beta as a negative regulator of dorsoventral axis formation in Xenopus embryos. *Proceedings of the National Academy of Sciences of the United States of America* **92**, 8498-8502.

Dougherty, W. G., Cary, S. M. and Parks, T. D. (1989). Molecular genetic analysis of a plant-virus polyprotein cleavage site - a model. *Virology* **171**, 356-364.

Freites, J. A., Tobias, D. J. and White, S. H. (2006). A voltage-sensor water pore. *Biophysical Journal* **91**, L90-L92.

Gagnon, D. G. and Bezanilla, F. (2010). The contribution of individual subunits to the coupling of the voltage sensor to pore opening in Shaker K channels: effect of ILT mutations in heterotetramers. *Journal of General Physiology* **136**, 555-568.

Gannon, F., Neilan, J. and Powell, R. (1988). Current Protocols in Molecular Biology (Ausubel, F.M.). *Nature* **333**, 309-310.

Gonzalez, C., Rosenman, E., Bezanilla, F., Alvarez, O. and Latorre, R. (2000). Modulation of the Shaker K+ channel gating kinetics by the S3-S4 linker. *Journal of General Physiology* **115**, 193-207.

Gonzalez, C., Rosenmann, E., Bezanilla, F., Alvarez, O. and Latorre, R. (2001). Periodic perturbations in Shaker K+ channel gating kinectics by deletions in the S3-S4 linker. *Biophysical Journal* **80**, 867.

Grigoriev, N. G., Spafford, J. D. and Spencer, A. N. (1999). Modulation of jellyfish potassium channels by external potassium ions. *Journal of Neurophysiology* **82**, 1728-1739.

Haddad, G. A. and Blunck, R. (2011). Mode shift of the voltage sensors in Shaker K+ channels is caused by energetic coupling to the pore domain. *Journal of General Physiology* **137**, 455-472.

Hess, B., Kutzner, C., van der Spoel, D. and Lindahl, E. (2008). GROMACS 4: Algorithms for highly efficient, load-balanced, and scalable molecular simulation. *Journal of Chemical Theory and Computation* **4**, 435-447.

Hille, B. (2001). Ion Channels of Excitable Membranes. Sunderland, MA, USA: Sinauer Associates, Inc.

Hodgkin, A. L. and Huxley, A. F. (1952). A quantitative description of membrane current and its application to conduction and excitation in nerve. *Journal of Physiology-London* **117**, 500-544.

Horne, A. J., Peters, C. J., Claydon, T. W. and Fedida, D. (2010). Fast and slow voltage sensor rearrangements during activation gating in Kv1.2 channels detected using tetramethylrhodamine fluorescence. *Journal of General Physiology* **136**, 83-99.

Hoshi, T., Zagotta, W. N. and Aldrich, R. W. (1994). Shaker potassium channel gating I. Transitions near the open state. *Journal of General Physiology* **103**, 249-278.

Huang, Q. Q., Harvey, C. M., Paterson, A. R. P., Cass, C. E. and Young, J. D. (1993). Functional expression of Na+-dependent nucleoside transport systems of rat intestine in isolated oocytes of *Xenopus laevis* - demonstration that rat jejenum expresses the purine-selective system N1 (CIF) and a 2nd, novel system N3 having broad specificity

for purine and pyrimidine nucleosides. *Journal of Biological Chemistry* **268**, 20613-20619.

Jiang, Y. X., Lee, A., Chen, J. Y., Ruta, V., Cadene, M., Chait, B. T. and MacKinnon, R. (2003a). X-ray structure of a voltage-dependent K+ channel. *Nature* **423**, 33-41.

Jiang, Y. X., Ruta, V., Chen, J. Y., Lee, A. and MacKinnon, R. (2003b). The principle of gating charge movement in a voltage-dependent K+ channel. *Nature* **423**, 42-48.

Jogini, V. and Roux, B. (2007). Dynamics of the Kv1.2 voltage-gated K(+) channel in a membrane environment. *Biophysical Journal* **93**, 3070-3082.

Khalili-Araghi, F., Jogini, V., Yarov-Yarovoy, V., Tajkhorshid, E., Roux, B. and Schulten, K. (2010). Calculation of the gating charge for the Kv1.2 voltage-activated potassium channel. *Biophysical Journal* **98**, 2189-2198.

Klemic, K. G., Durand, D. M. and Jones, S. W. (1998). Activation kinetics of the delayed rectifier potassium current of bullfrog sympathetic neurons. *Journal of Neurophysiology* **79**, 2345-2357.

Laine, M., Lin, M. C. A., Bannister, J. P. A., Silverman, W. R., Mock, A. F., Roux, B. and Papazian, D. M. (2003). Atomic proximity between S4 segment and pore domain in shaker potassium channels. *Neuron* **39**, 467-481.

Lee, S. Y., Lee, A., Chen, J. Y. and MacKinnon, R. (2005). Structure of the KvAP voltage-dependent K+ channel and its dependence on the lipid membrane. *Proceedings of the National Academy of Sciences of the United States of America* **102**, 15441-15446.

Lewis, A., Jogini, V., Blachowicz, L., Laine, M. and Roux, B. (2008). Atomic constraints between the voltage sensor and the pore domain in a voltage-gated K+ channel of known structure. *Journal of General Physiology* **131**, 549-561.

Li-Smerin, Y. Y., Hackos, D. H. and Swartz, K. J. (2000). Alpha-helical structural elements within the voltage-sensing domains of a K+ channel. *Journal of General Physiology* **115**, 33-49.

Long, S. B., Campbell, E. B. and MacKinnon, R. (2005). Crystal structure of a mammalian voltage-dependent Shaker family K+ channel. *Science* **309**, 897-903.

Long, S. B., Tao, X., Campbell, E. B. and MacKinnon, R. (2007). Atomic structure of a voltage-dependent K+ channel in a lipid membrane-like environment. *Nature* **450**, 376-U3.

Mathur, R., Zheng, J., Yan, Y. Y. and Sigworth, F. J. (1997). Role of the S3-S4 linker in Shaker potassium channel activation. *Journal of General Physiology* **109**, 191-199.

Miledi, R. and Parker, I. (1984). Chloride current induced by the injection of calcium into *Xenopus* oocytes. *Journal of Physiology-London* **357**, 173-183.

Papazian, D. M., Shao, X. M., Seoh, S. A., Mock, A. F., Huang, Y. and Wainstock, D. H. (1995). Electrostatic interactions of S4 voltage sensor in Shaker K+ channel. *Neuron* **14**, 1293-1301.

Patapati, K. K. and Glykos, N. M. (2011). Three force fields' views of the 3_{10} helix. *Biophysical Journal* **101**, 1766-1771.

Pathak, M. M., Yarov-Yarovoy, V., Agarwal, G., Roux, B., Barth, P., Kohout, S., Tombola, F. and Isacoff, E. Y. (2007). Closing in on the resting state of the shaker K+ channel. *Neuron* **56**, 124-140.

Payandeh, J., Scheuer, T., Zheng, N. and Catterall, W. A. (2011). The crystal structure of a voltage-gated sodium channel. *Nature* **475**, 353-U104.

Sack, J. T. and Aldrich, R. W. (2006). Binding of a gating modifier toxin induces intersubunit cooperativity early in the Shaker K channel's activation pathway. *Journal of General Physiology* **128**, 119-132.

Sack, J. T., Aldrich, R. W. and Gilly, W. F. (2004). A gastropod toxin selectively slows early transitions in the Shaker K channel's activation pathway. *Journal of General Physiology* **123**, 685-696.

Sand, R. M., Atherton, D. M., Spencer, A. N. and Gallin, W. J. (2011). jShaw1, a low-threshold, fast-activating Kv3 from the hydrozoan jellyfish *Polyorchis penicillatus. The Journal of Experimental Biology* **214**, 3124-3137

Sands, Z. A. and Sansom, M. S. P. (2007). How does a voltage sensor interact with a lipid bilayer? Simulations of a potassium channel domain. *Structure* **15**, 235-244.

Schoppa, N. E. and Sigworth, F. J. (1998). Activation of Shaker potassium channels I. Characterization of voltage-dependent transitions. *Journal of General Physiology* **111**, 271-294.

Schow, E. V., Freites, J. A., Gogna, K., White, S. H. and Tobias, D. J. (2010). Down-state model of the voltage-sensing domain of a potassium channel. *Biophysical Journal* **98**, 2857-2866.

Schwaiger, C. S., Bjelkmar, P., Hess, B. and Lindahl, E. (2011). 3_{10} helix conformation facilitates the transition of a voltage sensor S4 segment toward the down state. *Biophysical Journal* **100**, 1446-1454.

Seoh, S. A., Sigg, D., Papazian, D. M. and Bezanilla, F. (1996). Voltage-sensing residues in the S2 and S4 segments of the Shaker K+ channel. *Neuron* **16**, 1159-1167.

Smith-Maxwell, C. J., Ledwell, J. L. and Aldrich, R. W. (1998). Uncharged S4 residues and cooperativity in voltage-dependent potassium channel activation. *Journal of General Physiology* **111**, 421-439.

Starace, D. M. and Bezanilla, F. (2004). A proton pore in a potassium channel voltage sensor reveals a focused electric field. *Nature* **427**, 548-553.

Swartz, K. J. (2004). Towards a structural view of gating in potassium channels. *Nature Reviews Neuroscience* **5**, 905-916.

Tao, X., Lee, A., Limapichat, W., Dougherty, D. A. and MacKinnon, R. (2010). A gating charge transfer center in voltage sensors. *Science* **328**, 67-73.

Tombola, F., Pathak, M. M. and Isacoff, E. Y. (2006). How does voltage open an ion channel? *Annual Review of Cell and Developmental Biology* **22**, 23-52.

Treptow, W. and Tarek, M. (2006). Environment of the gating charges in the Kv1.2 Shaker potassium channel. *Biophysical Journal* **90**, L64-L66.

Treptow, W., Tarek, M. and Klein, M. L. (2009). Initial response of the potassium channel voltage sensor to a transmembrane potential. *Journal of the American Chemical Society* **131**, 2107-2110.

Villalba-Galea, C. A., Sandtner, W., Starace, D. M. and Bezanilla, F. (2008). S4-based voltage sensors have three major conformations. *Proceedings of the National Academy of Sciences of the United States of America* **105**, 17600-17607.

Yarov-Yarovoy, V., Baker, D. and Catterall, W. A. (2006). Voltage sensor conformations in the open and closed states in ROSETTA structural models of K+ channels. *Proceedings of the National Academy of Sciences of the United States of America* **103**, 7292-7297.

Zagotta, W. N., Hoshi, T., Dittman, J. and Aldrich, R. W. (1994). Shaker potassium channel gating II. Transitions in the activation pathway. *Journal of General Physiology* **103**, 279-319.

Chapter 4: Searching for the BrMT Binding Site in the K_v1.2 Voltage Sensor

Introduction

Voltage-gated potassium (Kv) channels regulate the flow of potassium ions across the membrane of neurons and muscle cells and are critical to the proper function of these excitable tissues (Hille, 2001). K_v proteins are comprised of four individual subunits, each with six transmembrane helices, which assemble in the membrane to form a central, potassium-selective pore gated by changes in electrical potential (Long et al., 2005). The pore domain, consisting of helices S5 through S6, is well characterized but the transitions that occur within the voltage-sensing domain, made up of helices S1 through S4 and associated linkers, during channel opening and closing are not clear. It is known that the S4 helix carries the positive residues that sense voltage changes (Aggarwal and MacKinnon, 1996; Seoh et al., 1996), and that the helix moves in the extracellular direction during activation, but the exact mechanism is the subject of debate (Catterall, 2010; Swartz, 2004; Tombola et al., 2006).

Much of our early knowledge about voltage-gated ion channels can be attributed to the strategic use of channel modulating agents, an extremely diverse class of compounds that can be as large as the ~5kDa venom peptides from snakes and invertebrates (Mouhat et al., 2008; Swartz, 2007) or as small as a magnesium ion (Guiet-Bara et al., 2007). The discovery and utilization of pore-blocking compounds (Figure 4-1) in particular shed much light on the structure of the pore domain in K_v and other ion channels. For example, pioneering studies with the

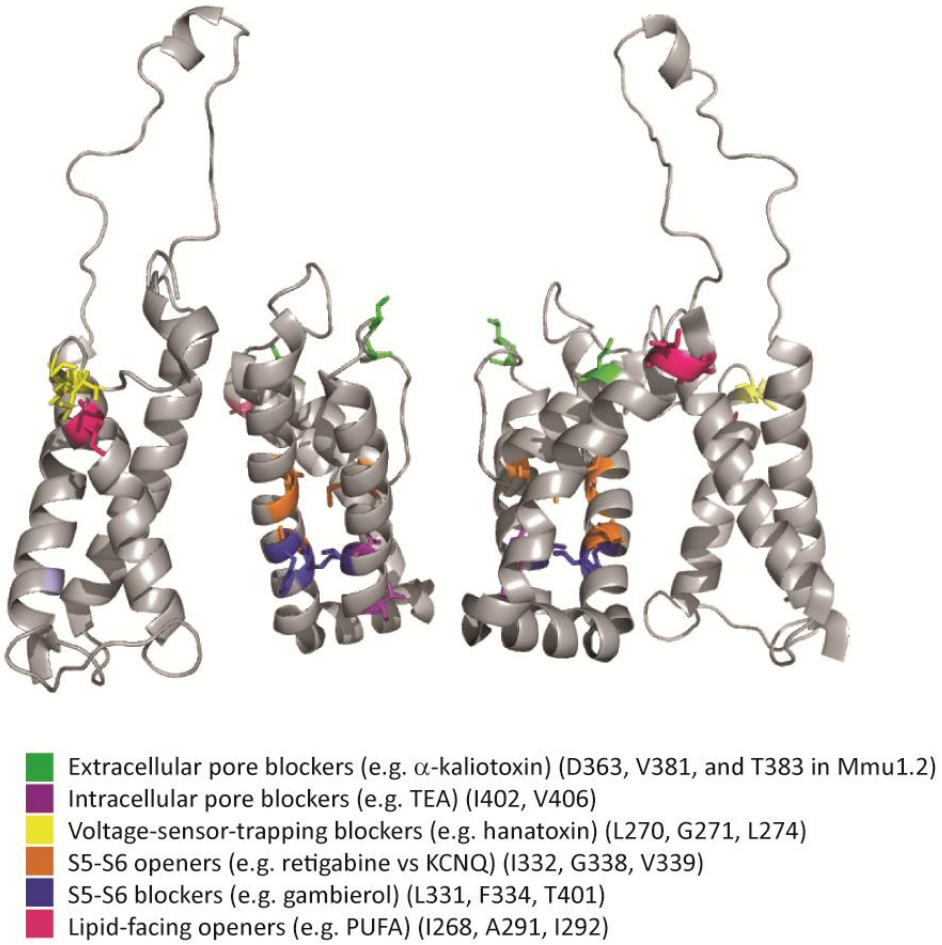

Figure 4-1. Known binding sites of K_v channel blockers and openers modeled onto the refined rat $K_v1.2$ crystal structure (3LUT) (Chen et al., 2010). The rat $K_v1.2$ channel is represented as a grey ribbon and shown side on, with the extracellular compartment above and the intracellular below. The equivalent of two subunits have been removed for clarity, with the voltage sensing domains (outer helices) interacting with the pore domains (inner helices) of adjacent subunits. Binding sites are displayed as sticks and are shaded according to the legend shown. Traditional pore blockers physically occlude the ion conduction pathway, visible down the middle of the protein, whereas gating modifiers alter channel function in an allosteric fashion.

quaternary ammonium compound tetraethylammonium chloride (TEA) (Armstrong and Binstock, 1965) confirmed that K_v channels conduct K^+ through pores rather than by a transporter mechanism (Armstrong, 1966; Armstrong, 1969). Further data from TEA derivatives of various chain lengths suggested that K_v pores have a wide inner chamber and narrower portion capable of passing dehydrated K+ ions (Armstrong, 1971), later termed the selectivity filter (Mackinnon and Yellen, 1990). Studying the action of local anesthetics on voltage-gated sodium channels (Hille, 1977) showed that the inner pore of Na_v channels had a similar structure to K_v channels (Catterall, 1987; Ragsdale et al., 1994; Starmer et al., 1984). The scorpion toxin Charybdotoxin, called α-KTx 1.1 under the kaliotoxin family nomenclature (Tytgat et al., 1999), was useful in determining features of the outer vestibule of K_v channels, and that they were similar to Ca^{2+}-activated K^+ channels (Mackinnon et al., 1988; Stampe et al., 1994).

In contrast with the surplus of pore blocking compounds, there are relatively few agents that have been found to interfere with the voltage sensing domain of K_v channels. The tarantula venom peptide hanatoxin was the first identified "gating modifier," shown through electrophysiological assays to bind to the voltage sensors when the channel was in the closed state (Swartz and Mackinnon, 1995), putting an additional energetic load for the S4 helix to overcome during activation (Phillips et al., 2005). Scanning mutagenesis revealed residues L270, G271, L274 (in rat K_v1.2 nomenclature) in the S3 helix to be the primary points of interaction for hanatoxin (Swartz and MacKinnon, 1997a; Swartz and MacKinnon, 1997b),

placing it at the C-terminal end of the S3 helix (also called S3b), and at the start of the extracellular S3-S4 linker (Figure 4-1). The S3b-linker-S4 region is called the "voltage sensor paddle" by some who consider it to move as a unit during channel activation (Jiang et al., 2003b), and studies with hanatoxin have been used to support this model of gating (Alabi et al., 2007; Lee et al., 2003).

Since the discovery of hanatoxin, over 300 ion channel peptide toxins have been identified with the same "inhibitory cysteine knot" structural motif (Gracy et al., 2008); those specific for K_v channels include the K_v4-specific heteropoda toxins (Sanguinetti et al., 1997; Zarayskiy et al., 2005) and the K_v2- and K_v4-specific jingzhao-toxins (Chen et al., 2008; Liao et al., 2006), both from tarantula species.

Peptide toxins have the advantage of being highly potent and specific to certain channel types, and they also have a large surface area on which to probe toxin-channel interactions, useful for spatially mapping regions of K_v channels. However, they are difficult to obtain and synthesize, and cannot be easily modified or optimized. Small organic molecules offer these opportunities, but again, relatively few have been found to target K_v channels. Gambierol is one, found to bind in the S5-S6 region but not in the pore (Cuypers et al., 2008; Kopljar et al., 2009). Two other small molecules serve as channel openers: retigabine (Lange et al., 2009; Tatulian et al., 2001) and polyunsaturated fatty acids (PUFA) (Borjesson and Elinder, 2011). These compounds have been shown to activate KCNQ and K_v1 channels, respectively, and the site of action has been determined (Figure 4-1). There is only one gating modifier that inhibits K_v

channels, for which the binding site has not been identified: 6-bromo-2-mercaptotryptamine, or BrMT.

BrMT (Figure 4-2) is a disulfide-linked dimer of brominated indoles sequestered in the hypobranchial gland of the marine snail *Calliostoma canaliculatum*. When threatened, this kelp-dwelling gastropod exudes defensive mucus, bright yellow in colour, which causes the tube feet of predatory starfish to retract upon contact (Bryan et al., 1997). Upon analysis of the mucus components, BrMT was found to be the active ingredient, blocking K_v1 and K_v4-mediated currents at levels of ~50% and ~80%, respectively, after *Xenopus laevis* oocytes expressing the channels were exposed to 10 μM BrMT (Kelley et al., 2003).

Much has already been determined about the mode of action of BrMT on the *Drosophila melanogaster* ShakerB channel (Sack and Aldrich, 2006; Sack et al., 2004). BrMT exerts its effects primarily through a ~10-fold slowing of activation with negligible effects on deactivation (Kelley et al., 2003; Sack and Aldrich 2006). BrMT does not diffuse through the plasma membrane and does not compete with pore blockers TEA and agitoxin (Sack and Aldrich, 2006). In addition, the graded slowing of activation is best explained by a model of fast binding (Sack et al., 2004), so the site must be fairly accessible from the external solution. Additional evidence pointed to a scheme where two molecules are bound per channel, with the binding of one negatively affecting the receptor site on the two adjacent subunits but not the one opposite, and that BrMT induces inter-subunit cooperativity upon binding, suggesting that the receptor site lies at the interface of two subunits (Sack and Aldrich, 2006).

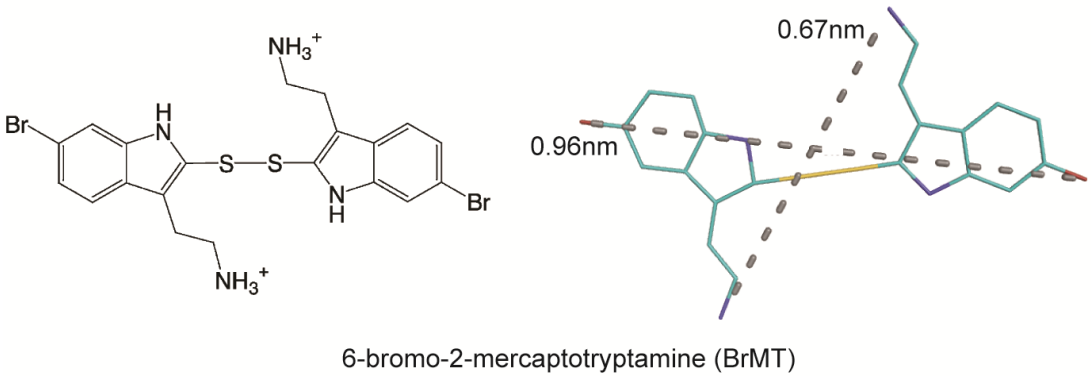

Figure 4-2. Structure of the gating modifier used in this study, 6-bromo-2-mercaptotryptamine (BrMT). This toxin is naturally found in the marine prosobranch snail *Calliostoma canaliculatum*. Left, the molecular structure of a BrMT dimer, the active form, in traditional notation. Right, a dimer of BrMT drawn as lines in PyMOL. In this fully extended conformation, BrMT measures approximately 0.96 nm from bromine to bromine and 0.67 nm from amine to amine.

The remaining piece of this story is localizing the precise binding site of BrMT. Novel receptor sites on voltage-gated ion channels are useful both in revealing structure-function relationships at the angstrom level, and in the design of therapeutic drugs. Many binding sites are not unique within channel subtypes. Clinically, it is thought that targeting specific K_v subtypes will eliminate unwanted or contradictory side effects, as seen in the efforts to produce a specific blocker of $K_v1.5$. This channel is expressed in the atria and not the ventricles of the heart, and blocking over-activity in the atrium can guard against atrial fibrillation (Ehrlich and Nattel, 2009; Yang et al., 2010). More directly, identifying the binding site would allow us to correlate the steady-state and kinetic disruptions of BrMT to the dynamics of that particular part of $K_v1.2$. In this case, the regions are the voltage sensing S4 and the S5 helix.

The goal of this work was to elucidate the molecular site of action for BrMT on mouse $K_v1.2$. We screened the toxin against wild-type mouse channels $K_v1.1$ through 1.6, mouse $K_v3.1b$ and $K_v3.2$, and the jellyfish channels jShak1 and jShaw1, and used the resulting data to search for conserved regions in BrMT-sensitive channels that were not conserved in BrMT-insensitive channels, including channels previously screened for binding activity (Kelley et al., 2003). We also performed a virtual docking of the small molecule dimer against a 3D model of the rat $K_v1.2$ channel in the closed state (Pathak et al., 2007) in order to triangulate a binding pocket and select residues for mutagenesis. This model was based on the original crystal structure of $K_v1.2$ (Long et al., 2005), and although it takes functional data into account, large membrane proteins are notoriously

difficult to simulate. Any errors in this model would mislead the docking algorithms and make less accurate predictions. However, as this model is the most recent and comprehensive estimate of the closed $K_v1.2$ channel, it was the best choice for automated docking. Prior evidence regarding the mode of action of BrMT reported by Sack and Aldrich (Sack and Aldrich, 2006) was used to constrain our choice of binding pockets to investigate experimentally. In the end, we identified three regions of interest - the S3-S4 linker, a pocket involving S308 and G329 of adjacent subunits, and a site involving F302 and K388 from adjacent subunits. The alterations we made to these sites in mouse $K_v1.2$ did not diminish the blocking ability of the toxin; nonetheless, this data should help constrain future experiments that aim to localize the receptor site of BrMT, a small molecule that likely represents a novel class of gating modifiers for the K_v1 and K_v4 subfamilies.

Materials and Methods

BrMT Isolation

Calliostoma canaliculatum (Calliostomatidae) individuals were initially collected and processed at Bamfield Marine Station (Bamfield, BC, CAN), but more snails were later obtained from a commercial source (Monterey Abalone Company; Monterey Bay, CA, USA) and shipped live to the University of Alberta (Edmonton, AB, CAN). There was no noticeable batch-to-batch variation between the different sources. Upon arrival, the snails were placed into salt water tanks with food for 1-2 weeks before being sacrificed. Snails were euthanized by a 30-60 minute treatment in 0.33M magnesium chloride. Hypobranchial glands, bright

yellow from the presence of 6-bromo-2-mercaptotryptamine (BrMT) dimer, were removed and flash frozen in glass vials immersed in a dry ice/ethanol bath and stored at -80°C until extraction. For each extraction, 30 to 50 glands were homogenized in 2 ml acidified acetone (1 ml concentrated HCl + 99 ml acetone) using a Polytron homogenizer (Kinematica, AG; Lucerne, SWZ) with fine teeth by three successive 10 second pulses at speed 5. The homogenate was centrifuged at 10 krpm for 5 minutes in glass Corex tubes at 4°C, and the yellow supernatant was collected in smaller glass test tubes. The pellet was repeatedly extracted with 2 ml acidified acetone until the supernatant no longer appeared yellow. The supernatants were pooled into a large glass Corex tube and dried under a stream of N_2 gas. The dried extract was resuspended in a 50/50 (v/v) mixture of acetonitrile (with 0.1% glacial acetic acid) and water and subject to HPLC through a Phenomenex C-18 column (10 x 250 mm, 5µm particle size) at a flow rate of 4 ml/min. BrMT was eluted in a gradient of acetonitrile (with 0.1% glacial acetic acid) that increased from 15% to 40% by 15 minutes, then to 95% from 15.01 to 20 minutes, and back down to 15% at 20.01 minutes. Absorbance at 240 nm was monitored and the BrMT fraction collected and subject to ^{1}H NMR and mass spectrometry, which suggested that >90% of the fraction was dimerized BrMT. The final dried extract was bright yellow in colour, indicating a substantial presence of dimer over monomer, as the monomer is colourless (Wolters et al., 2005). Purified BrMT was initially dissolved in dimethyl sulfoxide (DMSO; Sigma-Aldrich, Oakville, ON, CAN) as a stock solution and stored at -80°C, and diluted to aqueous working solutions in *X. laevis* physiological saline (ND96, in

mM: NaCl 96, KCl 2, $CaCl_2$ 1.8, $MgCl_2$ 1, HEPES 5) on the day of use. When initially diluting the DMSO stock solution, ND96 was added dropwise to BrMT while stirring. BrMT is degraded by light and adsorbs to plastics (Sack and Aldrich, 2006), so solutions were protected with aluminum foil and delivered by glass or Teflon tubing whenever possible. As DMSO can increase the fluidity of cellular membranes and block some ion channels (Larsen et al., 1996), efforts were taken to keep the final DMSO concentrations below 1%. When this was not possible, a control ND96 solution containing the same percentage of DMSO ("vehicle control") was delivered prior to the experiment. While no experiments were performed with BrMT monomer or a different indole compound to control for the high molarity of the BrMT solutions, we are confident that high indole content did not affect the channels, since there was at least one channel that was not at all affected by 100 µM BrMT.

Channel Cloning and Site-Directed Mutagenesis

Mouse $K_v1.1$ through $K_v1.6$, as well as $K_v3.1$ (isoform b) and $K_v3.2$, were purchased from OpenBiosystems (Huntsville, AL, USA). All open reading frames were amplified with appropriate primers for subcloning into the *X. laevis* expression vector pXT7 (Dominguez et al.,1995). Plasmids were grown in XL-1 Blue *Escherichia coli* and purified using the Qiagen Miniprep Kit (Qiagen, Mississauga, ON, CAN). The N-terminal inactivation ball of the mouse $K_v1.4$ sequence (corresponding to residues 2 through 25) was removed via PCR so that this channel would continue to conduct current during standard depolarization protocols. Plasmid constructs of all channels were linearized with either Xba I or

Sal I (Promega, Madison, Wisconsin, USA) and gel purified before transcription of capped mRNAs with the mMessage Machine T7 Kit (Ambion, Austin, Texas, USA). mRNAs were checked for quality by gel electrophoresis, and injected into *X. laevis* oocytes in 2 to 23 nl of nuclease-free water. Channels from the cnidarian *Polyorchis penicillatus*, jShak1 and jShaw1, were cloned as previously described (Jegla et al., 1995; Sand et al., 2011).

Site-directed mutagenesis of mouse K_v1.2 was accomplished via PCR. Mutagenic primers were designed using the PrimerX program, and the final amplicons containing single mutations were cut with Nsi I and Mfe I (Promega) for ligation into wild-type K_v1.2 in pXT7. To make double mutants, the Nhe I cut site positioned between the two mutation sites was utilized in a simple "cut and paste" cloning procedure. The MUSCLE multiple sequence alignment program (Edgar, 2004), located at the EBI web server (ebi.ac.uk), was used to align protein sequences. BioEdit (Hall, 1999) was used to view protein alignments and identify conserved regions, and was also used to confirm the correct nucleotide sequences of constructed mutants.

Electrophysiological and Pharmacological Analysis

BrMT was assayed on outward potassium currents recorded from *X. laevis* ooctyes expressing the various wild-type and mutant channels. Recordings were collected via two-electrode voltage clamp as previously described (Sand et al., 2011). Briefly, ovarian lobes were surgically removed from mature 1-2 year old *X. laevis* females, manually separated into 1cm clumps, and chemically

defolliculated with collagenase (Sigma-Aldrich) followed by treatment with hypertonic phosphate solution (100 mM K_2PO_4, pH 6.5 with HCl). Defolliculated oocytes were injected with 2-23nl of individual channel mRNAs dissolved in nuclease-free water and incubated for 24-48h at 18C in modified Barth's medium (MBM; in mM: NaCl 88, KCl 1, $Ca(NO_3)_2$ 0.33, $CaCl_2$ 0.41, $MgSO_4$ 0.82, $NaHCO_3$ 2.4, HEPES 10, sodium pyruvate 2.4; supplemented with 0.1 g/L penicillin G and 0.05 g/L gentamicin sulfate; pH 7.5 with Tris base) (Huang et al., 1993). Pipettes were pulled from 1.5 mm outside diameter borosilicate filament capillary tubing to 0.1-1.5 MΩ resistance when filled with 3M KCl. Recordings were made with a GeneClamp 500B amplifier (Molecular Devices) collecting at 10kHz and filtering at 1kHz, with commands delivered by a PC (Dell) running pClamp 9.0 (Molecular Devices). Leak currents were subtracted online using the P/4 procedure.

A standard two-pulse protocol was used to evaluate the effect of BrMT on the various channels. The cells were held at a -90 mV holding potential prior to a depolarization phase (from -80 to +80 mV in 10 mV increments, 100 ms in duration) followed by a 50 ms tail step to -50 mV, and a return to the holding potential. For mouse $K_v1.5$, the depolarization phase was 50 ms. To quantify the amount of BrMT block, individual traces collected after BrMT exposure were compared directly to the control or vehicle control trace collected on the same cell. Currents were elicited at or near +60 mV to fully open the channels. The last ten data points at the end of the depolarization phase were averaged in the control trace and the BrMT trace, and the fractional current determined by simple

division of these two averages. Fractional currents were measured and averaged for multiple oocytes. Conductance-voltage (G-V) relationships were determined as previously described (Sand et al., 2011). Briefly, tail currents were fitted to a double exponential decay, taking the value for inferred conductance at a time approximately 1 ms after the repolarization phase began. Normalized G-V curves were averaged and fitted with a fourth-order Boltzmann relation (Hodgkin and Huxley, 1952).

To quantify activation kinetics, the 10-90% rise time, or the time it took for currents to go from 10 to 90% of maximal, was compared before and after BrMT exposure. Rise times were measured in Clampfit 10.2 (Molecular Devices), and the ratio of rise times (BrMT/control, or the "fold-slowing") was determined and averaged for multiple oocytes.

During BrMT experiments, oocytes were subject to the voltage protocol described above in control (ND96) and/or vehicle control (ND96+DMSO) solution prior to the addition of BrMT. BrMT solutions were added to the bath manually with a Pasteur pipette or glass syringe with 3 minutes incubation time before re-running the voltage protocol. Due to its hydrophobic nature, BrMT does not easily wash out of the bath, and thus only one experiment could be run on any individual cell. Therefore, dose-response curves were generated by administering one concentration of BrMT to a single oocyte and averaging among many oocytes. Between experiments, the bath was perfused extensively with ND96 to remove residual BrMT.

When appropriate, we used a two-tailed Student's t-test, with p-values below 0.05 determining statistical significance.

Virtual Docking

Virtual docking was performed using AutoDock Vina (Trott and Olson, 2010). The closed model of rat $K_v1.2$ released by Pathak et al. (Pathak et al., 2007) served as the target receptor. This model was based on the original rat $K_v1.2$ crystal structure Protein Data Bank (PDB) file 2A79 (Long et al., 2005). The ligand was dimerized BrMT, drawn in ChemDraw 12.0 (CambridgeSoft, Cambridge, MA, USA) and converted to PDB format using MN.Convert and CORINA (Schwab, 2010). Before docking, polar hydrogen atoms were added to the $K_v1.2$ model, and all bonds that could be made flexible in the BrMT dimer were made flexible. The search space, or grid box, on the $K_v1.2$ closed model was chosen to encompass an entire quadrant of the channel, when looking at the protein from the extracellular side. Including the entire channel was not possible as it exceeded the maximum grid box volume in AutoDockTools. The final coordinates of the grid box were, in grid points (0.375 angstroms/grid point): x = 120, y = 94.397; z =-36.239. The final grid box measurements were, in grid points: x = 126; y = 106; z = 126. For each run, the search exhaustiveness was set at 8 (maximal) and the energy range at 3. A total of 10 randomly seeded runs were performed with 20 binding modes each, resulting in 200 final modes. PyMOL (Schrödinger, 2010) was used to view all PDB files, including the results from virtual docking, and to produce figure images. A tetramer of the refined rat $K_v1.2$ crystal structure, 3LUT (Chen et al., 2010) was created using PyMOL.

Results

BrMT vs. Mouse K_v1 Channels

Two-electrode voltage clamp data collected from oocytes expressing the six mouse K_v1 channels clearly showed all of them to be sensitive to 100 µM BrMT (Figure 4-3). Traces elicited by a +60 mV pulse in the presence of the toxin (Figure 4-3A, cyan lines) show a reduced level of current compared to traces collected in saline or vehicle control solution on the same cell (Figure 4-3A, black lines). Scaling the BrMT-exposed traces to match the steady-state level of current of the control traces revealed the extent of kinetic slowing of the channels by BrMT (Figure 4-3A, inset).

BrMT block was quantified by calculating the fractional current, or the current at the end of a 100 ms pulse to +60 mV (except mouse K_v1.5, which was measured at the end of a 50 ms pulse). Within the mouse K_v1 group, K_v1.1 was blocked the most by 100 µM BrMT, with current reduced to 28% of control, whereas mouse K_v1.3 was least affected with 74% of current available under the influence of the toxin (Figure 4-3B). The amount of kinetic slowing was quantified by the ratio of 10-to-90% rise times (in BrMT/in vehicle control). BrMT slowed the rise of current in all mouse K_v1 channels, to the extent that they did not reach a plateau during the 100 ms pulse, taking sometimes over 800 ms to 1 s to reach a steady state (not shown). Therefore, the 10-90% rise time in BrMT is an underestimation of the actual rise time, and thus the ratio (rise time in BrMT/rise time in vehicle control) will also be an underestimation of the severity of the kinetic effects induced by BrMT. Nonetheless, it can still indicate which channels BrMT is

affecting more than others. Using this analysis, mouse K_v1.1, 1.3, 1.4nt, and 1.6 were all slowed by a factor of ~4, whereas mouse K_v1.2 and 1.5 were slowed by a factor of ~7 during the activation of currents elicited by a +60 mV pulse (Figure 4-3C).

To get a sense of how BrMT differentially affected the voltage sensitivity of activation in the mouse K_v1 subfamily, we derived normalized conductance-voltage (G-V) relationships of the six wild type channels from isochronal tail currents before and after exposure to 100 µM BrMT (Figure 4-4). The resulting data were well fitted by fourth-order Boltzmann relations (Figure 4-4A, lines). Overall, BrMT treatment caused all six channels to open at more positive potentials and, once open, to respond less sharply to changes in voltage. After exposure to the toxin, all of the G-V curves were shifted in the positive direction on the voltage axis and the linear portion of the curve was obviously less steep (with the exception of mouse K_v1.4nt, which appeared to have a similar slope in BrMT) (Figure 4-4A). The G-V shifts were quantified by the ΔV_{50} (V_{50} in BrMT - V_{50} in control), which showed that the changes in voltage dependence induced by BrMT ranged from +10 in K_v1.3 to +35 mV in K_v1.1 (Figure 4-4B).

The change in Boltzmann slope factor was also quantified and showed K_v1.6 and K_v1.4nt to be the least affected by BrMT in this respect, while K_v1.5 required an additional ~9 mV to cause an e-fold change in conductance after incubation with the toxin (Figure 4-4C). Mouse K_v1.4nt was the only channel to reach maximum

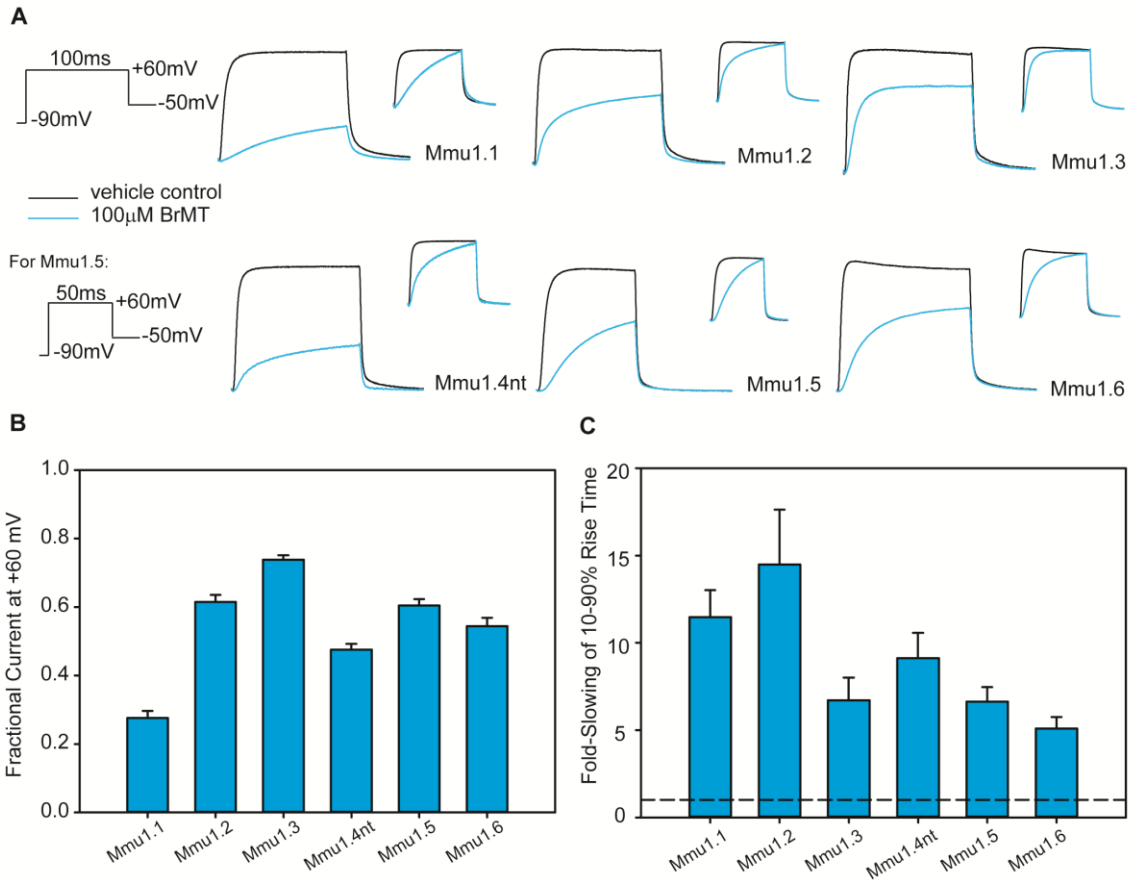

Figure 4-3. BrMT inhibits mouse $K_v1.1$ through $K_v1.6$. A, Example two-electrode voltage clamp traces in control solution (black lines) and in 100 µM BrMT (cyan lines). Cells were exposed to a range of stimulating voltages (from -80 to +80 mV in 10 mV steps) but only the sweep from +60 mV is shown. The depolarization phase lasted 100 ms, except mouse $K_v1.5$, which was 50 ms. Control currents ranged from 7 to 14 µA at steady-state, but are shown scaled to the same maximum for comparison. For all six channels, the maximal current during the pulse was reduced and opening kinetics were slowed (inset). B, The fractional current at the end of the pulse for all six channels after a 3 minute exposure to 100 µM BrMT. C, Slowing of activation kinetics by 100 µM BrMT. The ratio of the 10-90% rise time in BrMT to that during the control trace was calculated for individual experiments and averaged. As currents did not reach maximum in BrMT, these are an under-representation of the true kinetic slowing. Dotted line represents a ratio of unity, i.e. no kinetic slowing. For B and C, bars are shown mean + s.e.m., with n values from 3 to 10.

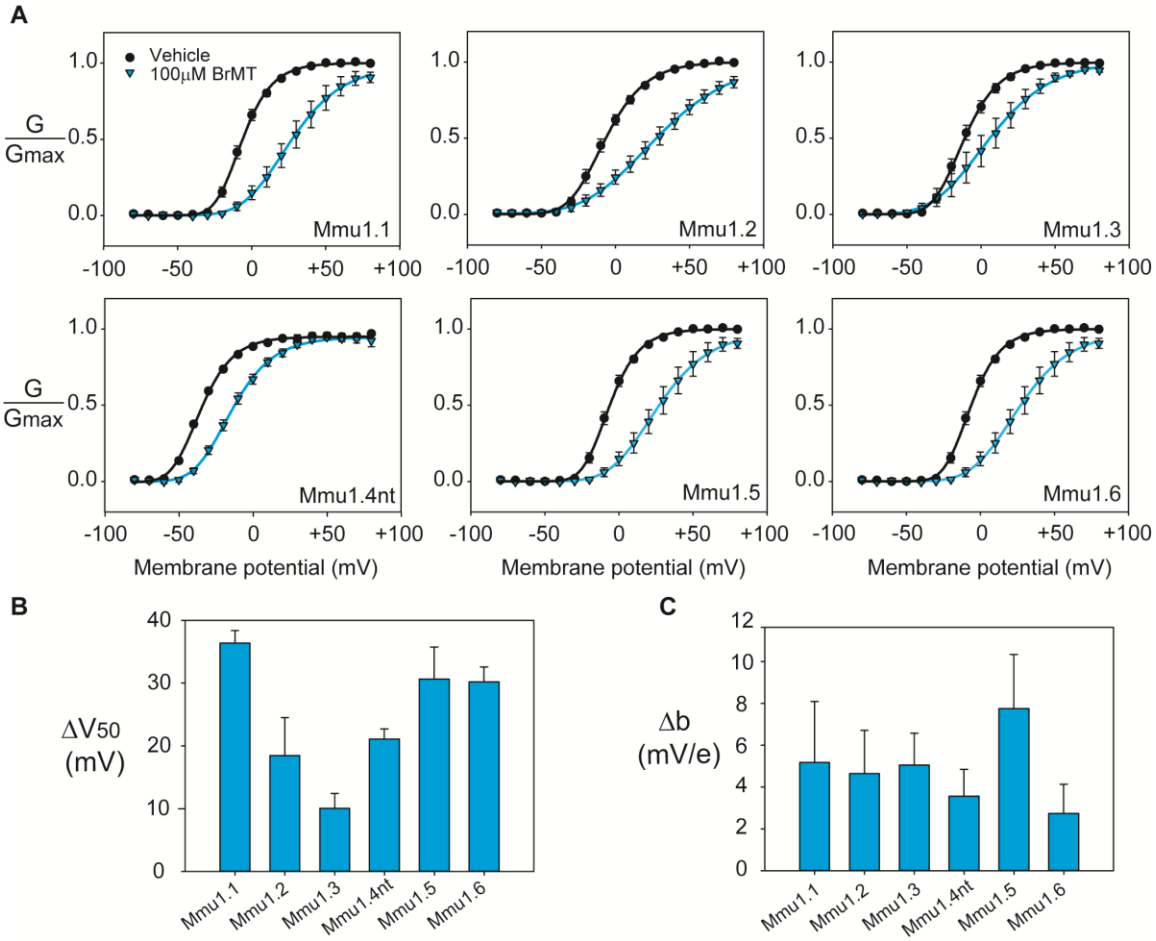

Figure 4-4. BrMT shifts steady-state activation properties of mouse K_v1.1 through 1.6. A, Normalized conductance-voltage (G-V) relationships as measured from isochronal tail currents in control solution (black circles) and in 100 μM BrMT (cyan triangles). Data were fitted with fourth-order Boltzmann relations (lines) to find the midpoint voltage (V_{50}) of the curve, as well as the slope factor (b). All six mouse channels activated at more positive voltages and had less steep sigmoid curves under the influence of BrMT. B, The shift on the voltage axis of the normalized G-V relationships. The V_{50} value recorded in control conditions was subtracted from the V_{50} measured in BrMT for individual experiments and averaged. C, The change in slope factor of the normalized G-V curves after incubation with BrMT. The slope in control solution was subtracted from the slope in BrMT for individual experiments and averaged. For panels B and C, bars are shown mean + s.e.m., with n values ranging from 3 to 10.

conductance in the presence of 100 µM BrMT in the voltage range we tested, which was -80 to +80 mV (Figure 4-4A).

BrMT vs. S3-S4 Linker Mutants

The loop sequence connecting the third and fourth transmembrane helices in K_v channels (Figure 4-5) is extracellular and contains the binding site for peptide gating modifier toxins (Figure 4-1). Therefore, we looked at whether changing the S3-S4 linker of mouse K_v1.2 would affect the ability of BrMT to exert its blocking effects. For the work presented in Chapter 3 of this thesis, in which we estimated the distance between the S3 and S4 helices in the closed and open state, we created mutated versions of K_v1.2 in which thirteen residues of the S3-S4 loop (A275 to A287) were replaced with homopolymeric stretches of, among others, glycine; for this study, we used the "G4" mutant, the one with four glycines in place of the thirteen residues in the S3-S4 linker. We also made versions of K_v1.2 with the homologous loop sequences from the other mouse K_v1 subtypes swapped in (Figure 4-5).

All mouse K_v1.2 loop variants were susceptible to BrMT action (Figure 4-6). TEVC traces from oocytes expressing the channels show inhibition patterns similar to wild type mouse K_v1.2 (Figure 4-6A). The K_v1 loop mutants were reduced to values ranging from 51% of control with the loop from K_v1.5 to 70% with the loop from K_v1.4. The mutant with a loop of four glycines had a fractional current of 69% after 3 minutes incubation with the toxin (Figure 4-6B) and the

activation kinetics were slowed 3.7-fold (Figure 4-6C). For the chimeric loop variants, activation kinetics were slowed from 5.2-fold (in Loop 1.5) to 10.9-fold (in Loop 1.1) (Figure 4-6C).

To fully characterize BrMT on the wild type mouse K_v1 channels and the $K_v1.2$ S3-S4 loop variants, we collected dose-response data at tenfold concentration differences ranging from 1 µM to 1 mM, and if needed, 2 mM (Figure 4-7). The resulting data were well fitted by 4-parameter logistic functions (Figure 4-7A), with the exception of mouse $K_v1.3$, which did not reach a plateau level of block at high BrMT concentrations. For the wild type channels, this analysis generated half-inhibitory concentration (IC_{50}) values that ranged from ~18 µM in $K_v1.1$ to over 300 mM in $K_v1.3$ (Figure 4-7B, white bars). For the loop variants, IC_{50} values ranged from 86 µM in Loop 1.1 to 184 µM in Loop 1.6 (Figure 4-7B, striped bars). Overall, when comparing mouse $K_v1.2$ to the loop mutants and the other wild type K_v1 channels, data for the mutants resembles BrMT action on $K_v1.2$ more than the loop donor channel, both in terms of IC_{50} (Figure 4-7B, cyan bars) and in fractional current measured at +60 mV (Figure 4-7C, cyan bars).

BrMT vs. S308 and G329 Mutants

The second choice for a BrMT binding site was located by aligning the sequences from channels that had been screened up to that point for BrMT inhibition and identifying conserved regions using BioEdit. Previously screened channels

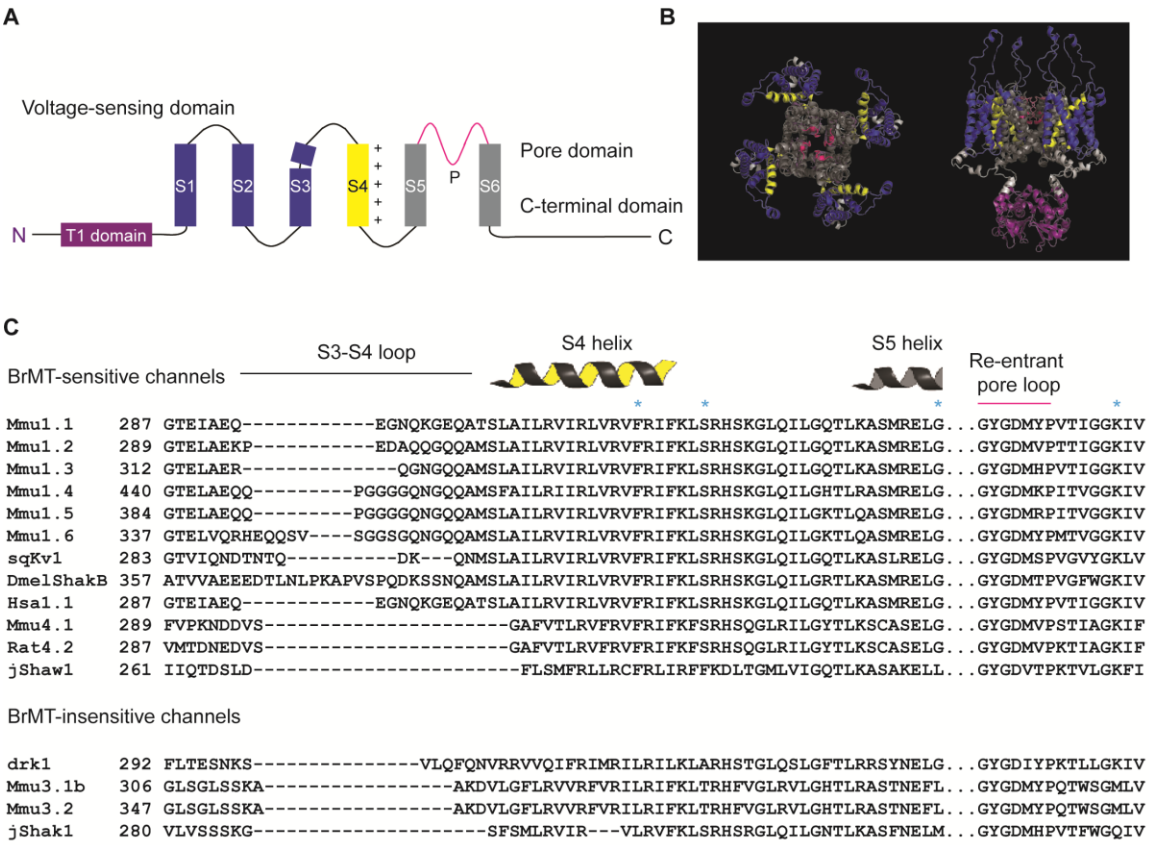

Figure 4-5. K_v structure and sequence alignment A, Schematic of the structure of one K_v subunit. The N-terminus in some channels has an inactivation particle (not shown) prior to the T1 domain. The T1 domain (purple) allows subunits to assemble into tetramers. The voltage-sensing domain (blue/yellow) is comprised of helices S1 through S4 and associated loops. The voltage sensor (yellow) is the S4 helix, which has positively charged residues at every third position; four pore domains (grey) join centrally to make the pore, with the pore loop (pink) forming the K+ selectivity filter. B, The 3LUT 3-D structure of rat $K_v1.2$ in ribbon form. Left, view from the extracellular side. Right, view from the side. C, MUSCLE alignment of the channels in this study, along with those from Kelley et al. (2003). Only selected regions are shown. Blue asterisks indicate sites we targeted for mutagenesis to abolish BrMT sensitivity.

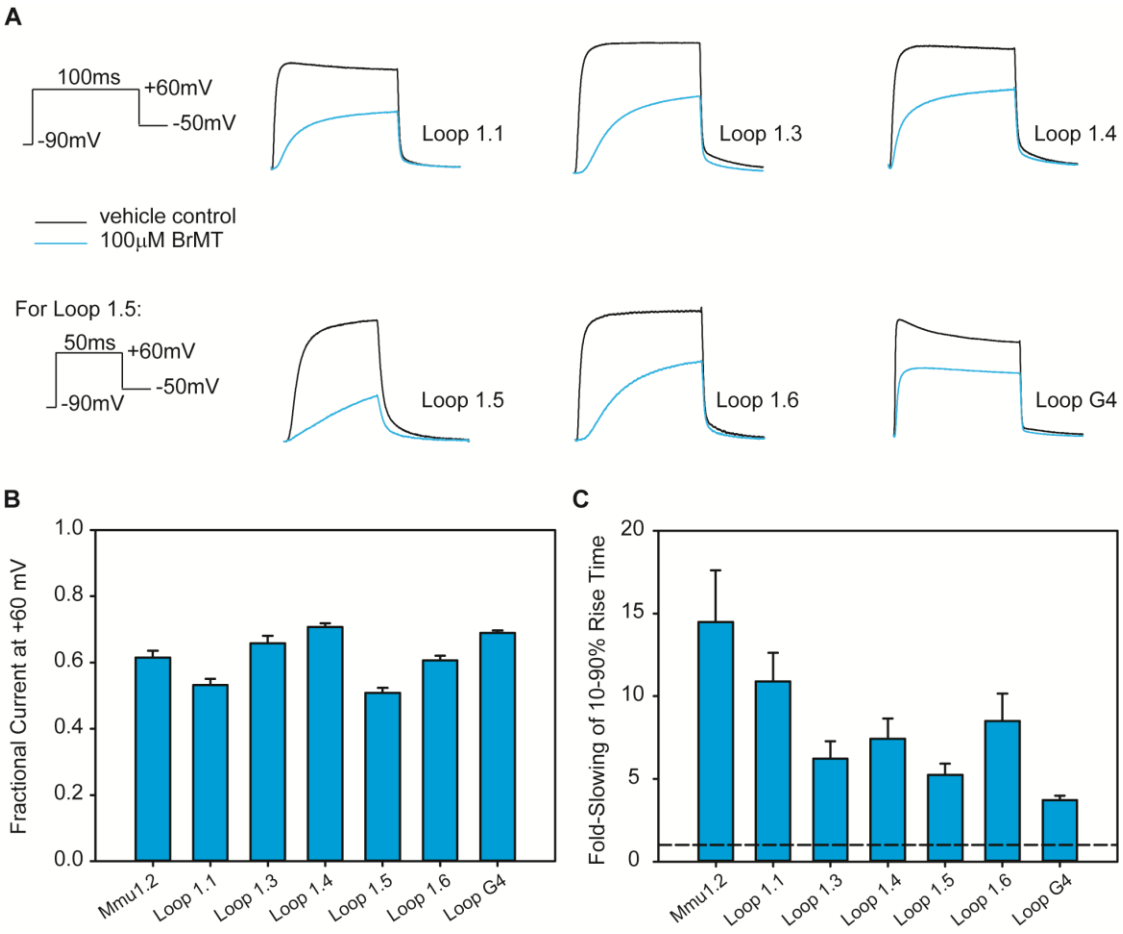

Figure 4-6. BrMT inhibits mouse $K_v1.2$ with the A275 to A287 of the S3-S4 linker replaced. A, Representative two-electrode voltage clamp traces in control solution (black lines) and in 100 μM BrMT (cyan lines). Cells were exposed to a range of voltages (from -80 to +80 mV in 10 mV steps) but only the sweep from +60 mV is shown. The depolarization phase lasted 100 ms, except Loop 1.5, which was 50 ms. Control currents ranged from 7 to 20 μA at steady-state, but are shown scaled to the same approximate maximum. B, Fractional current at the end of the pulse in 100 μM BrMT. C, Slowing of activation kinetics in 100 μM BrMT. The ratio of the 10-90% rise time in BrMT to that during the control trace was calculated for individual experiments and averaged. As the currents did not reach maximum in BrMT, these values are an under-representation of the true kinetic slowing. Dotted line represents a ratio of unity, i.e. no kinetic slowing. For panels B and C, bars are shown mean + s.e.m., with n values ranging from 3 to 9.

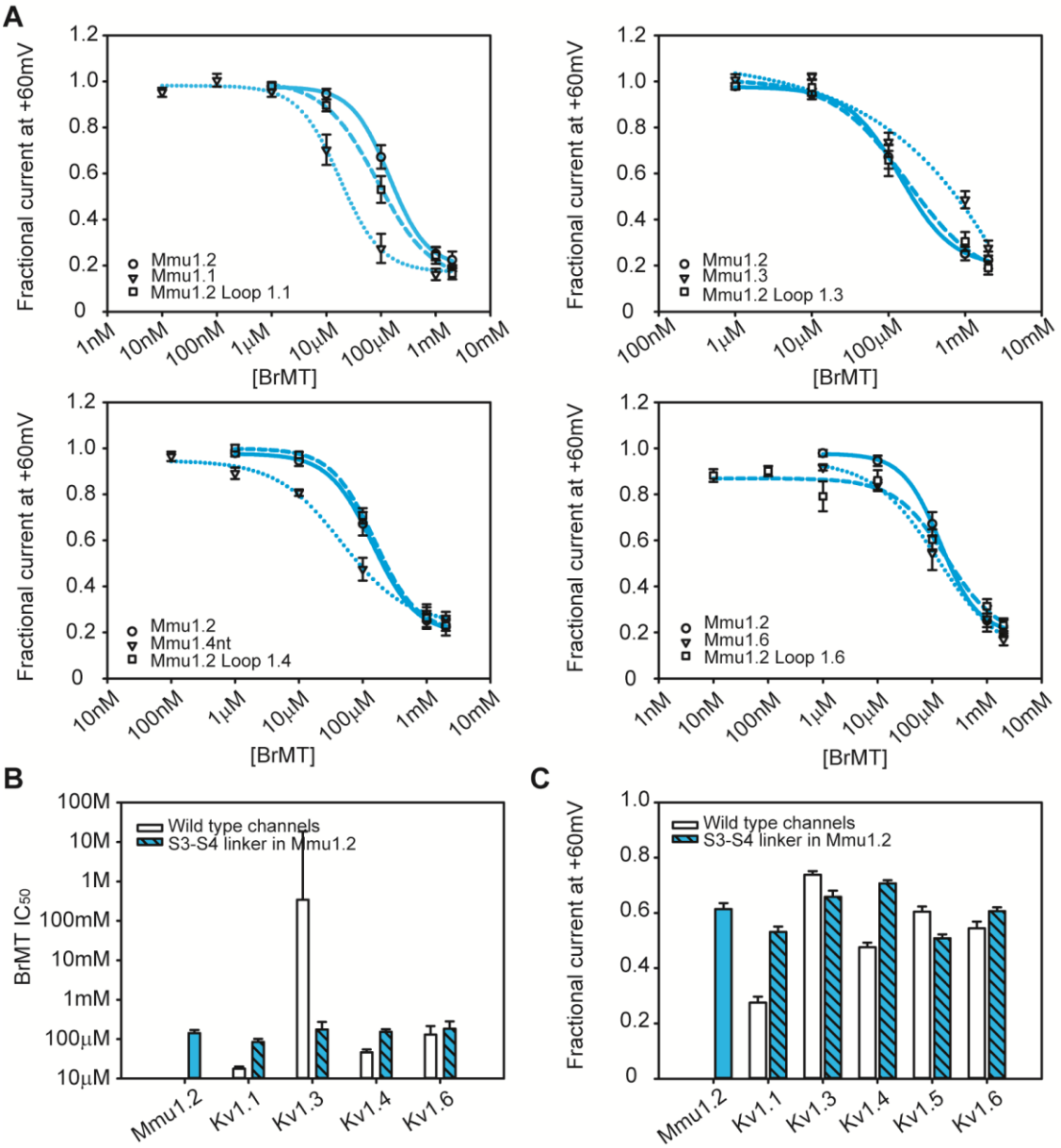

Figure 4-7. Replacing the S3-S4 linker of mouse $K_v1.2$ does not change the quality of BrMT block. A, Dose-response curves for BrMT against wild type mouse $K_v1.1$ through 1.6, as well as against versions of mouse $K_v1.2$ with residues A275 to A287 replaced with homologous residues from the other K_v1 channels. Each graph shows the fractional current measured at the end of a +60 mV pulse in 100 µM BrMT, plotted against BrMT concentration. During experiments, each cell was exposed to only a single concentration of BrMT. Data for the wild type mouse $K_v1.2$ (circles, solid lines), the other wild type K_v1 channel (triangles, dotted lines) and the associated mouse $K_v1.2$ loop variant (squares, dashed lines) are shown. The lines represent fits to 4-parameter logistic equations. B, The mid-point concentration (IC_{50}) of the curves in the previous panel for wild type mouse $K_v1.2$ (cyan, solid bar), the other wild type K_v1 channels (white bars), and the loop variants (striped cyan bars). Bars are shown + s.e.m. with the standard errors determined through the logistic fits. C, Fractional current at the end of a 100 ms pulse to +60 mV, in the presence of 100 µM BrMT. Labeling is the same as in the previous panel.

(Kelley et al., 2003) were included in the alignment (Figure 4-5). Those that were previously shown to be sensitive included sqKv1 from *Loligo opalescens*; the B isoform of Shaker from *Drosophila melanogaster*; K_v1.1 from *Homo sapiens*; K_v4.1 from *Mus musculus*; and K_v4.2 from *Rattus norvegicus.* Channels that were not sensitive were drk1 (K_v2.1) from *Rattus norvegicus* and K_v3.1 from *Mus musculus*. These channels were aligned with the 6 mouse K_v1 channels tested in this study, and conserved regions among BrMT-sensitive channels were defined as sequences of three or more residues that matched 100% in amino acid identity.

Ten such regions were found, one in the S1 region, one in the selectivity filter, and the rest in the S4, S5, and S6 helices. Upon mapping the latter regions onto the closed model of K_v1.2, two conserved residues stood out: S308 and G329 (Figure 4-5C). In the 3D closed model, S308 from one subunit creates a binding pocket with G329 from the adjacent subunit (Figure 4-8). In drk1, a BrMT-insensitive channel, the residue which aligns with S308 is an alanine, and in mouse K_v3.1 threonine (Figure 4-5C); therefore, we mutated S308 in mouse K_v1.2 to alanine and threonine with the goal of significantly reducing or abolishing BrMT efficacy. At the second residue of interest, G329, mouse K_v3.1 contains a leucine, so we created the G329L mutant with the same goal in mind.

Injection of S308T mRNA into oocytes did not produce measurable currents, but S308A and G329L were expressed (Figure 4-9). After treatment with 100 µM BrMT, oocytes expressing S308A and G329L mutants had reduced current

(Figure 4-9A). S308A currents dropped to 65% of control, compared to 55% for G329L and 61% for wild type mouse K_v1.2 (Figure 4-9B). Activation kinetics for S308A were slowed by a factor of 7.8 compared to 10.7 for G329L and 14.5 for K_v1.2 (Figure 4-9C). None of these differences were statistically significant ($p > 0.05$).

BrMT vs. K_v3 and Cnidarian Channels

To get a more informative alignment on which to base binding site predictions, four more channels were added to the analysis: mouse K_v3.1, mouse K_v3.2, and two cnidarian channels, jShak1 and jShaw1, which group in the K_v1 and K_v3 subfamilies respectively. Previous results (Kelley et al., 2003) suggested that BrMT binds only to K_v1 and K_v4 subtypes, but we found that incubation with 100 µM BrMT produced a small blocking effect on the two mouse K_v3 channels expressed in *X. laevis* oocytes (Figure 4-10A). Fractional current at +60 mV was 86% and 87% of control for mouse K_v3.1 and K_v3.2, respectively (Figure 4-10B), compared to 61% for mouse K_v1.2. However, activation kinetics were largely unchanged for the mouse K_v3 channels after the addition of BrMT, with the 10-90% rise time only being slowed 1.2 times for mouse K_v3.1 and 1.1 times for K_v3.2 (Figure 4-10C). This could mean that BrMT blocks the pore in these channels rather than interfering with the gating process, but more experiments would be needed to state this conclusively.

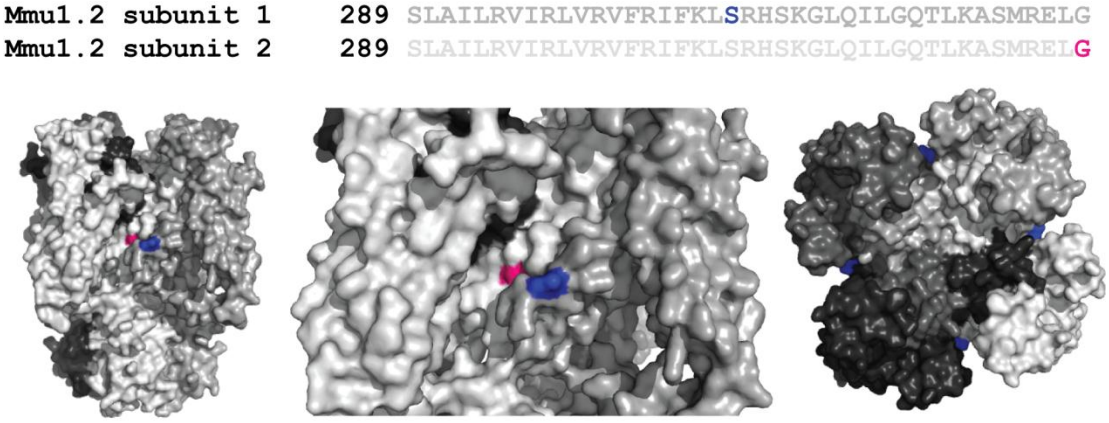

Figure 4-8. The S308/G329 binding pocket mapped onto a closed model of rat $K_v1.2$. These positions were the same in channels with BrMT sensitivity, and different in channels not blocked by the toxin. The serine at position 308 (blue) interacts with the glycine at position 329 (pink) on an adjacent subunit. This binding pocket satisfies the condition that the site include residues from two or more subunits (middle image; subunits in shades of grey) and that it is accessible from the extracellular face (rightmost image). To test this hypothesis, we changed S308 to threonine and alanine, and G329 to leucine in mouse $K_v1.2$. The closed model of rat $K_v1.2$ developed by Pathak and others (Pathak et al., 2007) is shown here in as a surface. Images were created in PyMOL.

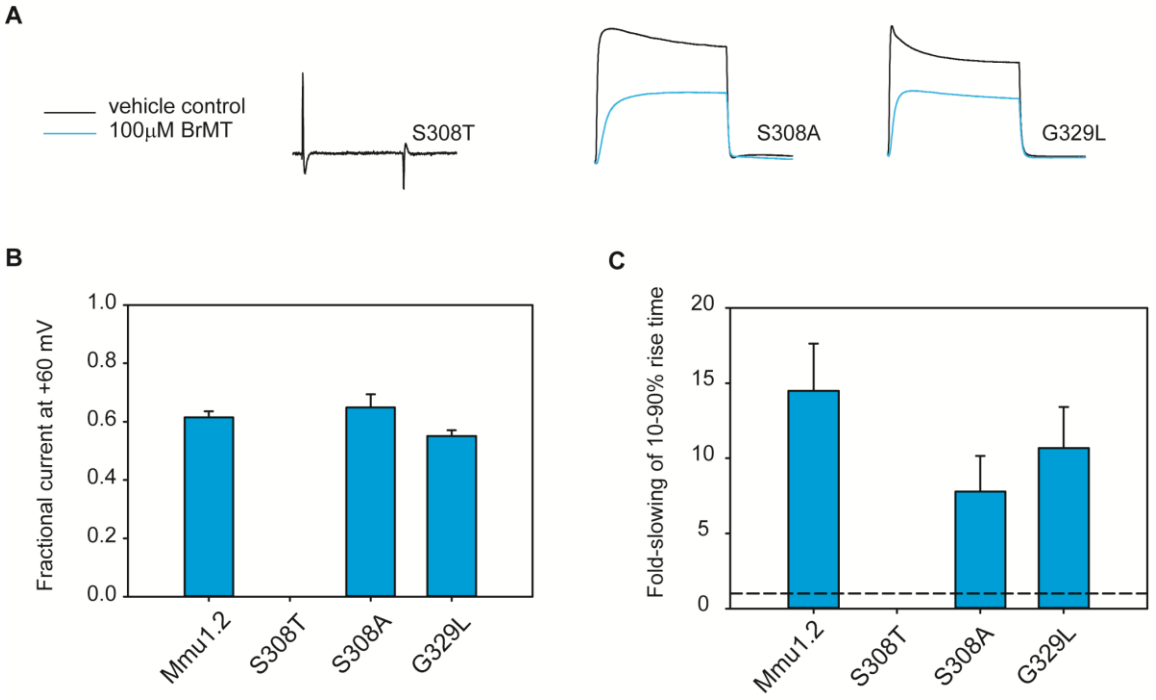

Figure 4-9. S308 and G329 mutations did not abolish BrMT activity against mouse $K_v1.2$. A, Representative two-electrode voltage clamp traces for S308T, S308A, and G329L mutant channels in control solution (black lines) and in 100 μM BrMT (cyan lines). Cells were exposed to a range of voltages (from -80 to +80 mV in 10 mV steps) but only the sweep from +60 mV is shown. The depolarization phase lasted 100 ms. Control currents ranged from 18 to 20 μA at steady-state, but are shown scaled to the same approximate maximum. S308T either did not form functional channels or was not expressed. B, Fractional current at the end of the pulse in 100 μM BrMT. The mutants showed fractional block not significantly different than wild type $K_v1.2$ ($p = 0.448$, 0.0948). C, Slowing of activation kinetics in 100 μM BrMT. The ratio of the 10-90% rise time in BrMT to that during the control trace was calculated for individual experiments and averaged. For the wild type, currents did not reach maximum in BrMT, so the ratio is an under-representation of the true kinetic slowing. These mutants were not slowed significantly more than wild type $K_v1.2$ ($p = 0.208$, 0.463). Dotted line represents a ratio of unity, i.e. no kinetic slowing. For panels B and C, bars are shown mean + s.e.m., with n values ranging from 3 to 9.

The jellyfish channels jShak1 and jShaw1 had opposite effects than expected with the snail toxin. The K_v1 channel jShak1 was completely insensitive to 100 µM BrMT (Figure 4-10A), with a fractional current of 98% (Figure 4-10B), and was not kinetically slowed, with a of rise time ratio of 1.0 (Figure 4-10C). jShaw1, on the other hand, was reduced to 57% of control (Figure 4-10B) and was slowed 2.3-fold during activation (Figure 4-10C).

BrMT vs. F302 and K388 Mutants

Adding the jShaw1 sequence to the alignment of BrMT-sensitive channels reduced the number of conserved regions from 10 to 5, but in each case the residues could also be found in two or more BrMT-insensitive channels, and so were not suitable candidates for mutagenesis. At this point, rather than visually searching for individual residues that correlated with BrMT activity in the various channels, we employed a computational approach: virtual receptor-ligand docking using AutoDock Vina. A 3-dimensional model of mouse $K_v1.2$ in the closed state served as the receptor and a flexible dimer of BrMT served as the ligand (see Materials and Methods for details).

In total, 200 conformations (or binding modes) were identified for BrMT on the closed $K_v1.2$ model. Since the entire surface of the channel was effectively accessible to the ligand, many of the suggested binding modes were in locations that could be excluded based on prior functional evidence (Sack and Aldrich, 2006). For example, those in the central cavity (inner vestibule) (31/200 modes; -5.46 mean binding energy) or near the tetramerization domain (27/200; -5.09)

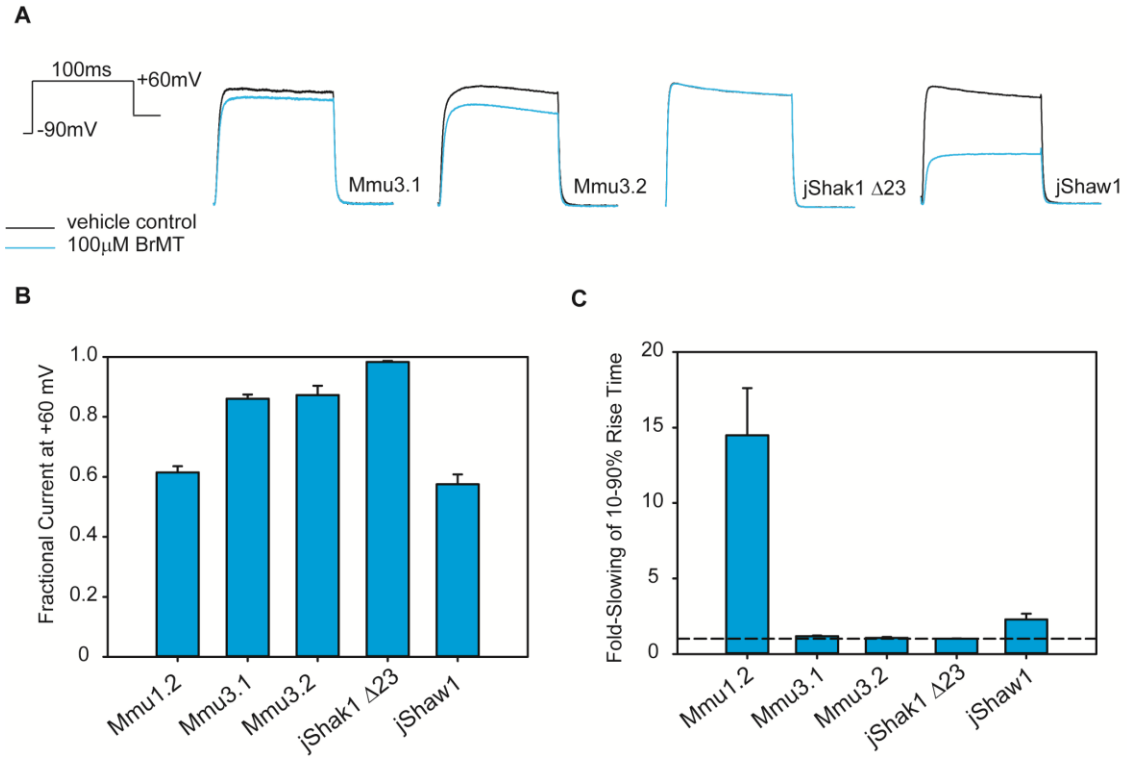

Figure 4-10. BrMT does not block mouse K_v3 channels or a jellyfish K_v1. A, Representative two-electrode voltage clamp traces for mouse $K_v3.1$, $K_v3.2$, and *Polyorchis penicillatus* jShak1 (with inactivation removed) and jShaw1, in control solution (black lines) and in100 μM BrMT (cyan lines). Cells were exposed to a range of stimulating voltages (from -80 to +80 mV in 10 mV steps) but only the sweep from +60 mV is shown. The depolarization phase lasted 100 ms. B, Fractional current at the end of the pulse in 100 μM BrMT. Wild type mouse $K_v1.2$ is shown for comparison. C, Slowing of activation kinetics in the four channels by 100 μM BrMT. Wild type mouse $K_v1.2$ is shown for comparison. The ratio of the 10-90% rise time in BrMT to that during the control trace was calculated for individual experiments and averaged. Dotted line represents a ratio of unity, i.e. no kinetic slowing. For panels B and C, bars are shown mean + s.e.m., with n values ranging from 3 to 9.

were excluded as possibilities since BrMT was shown not to diffuse through the membrane (Sack et al., 2004). Modes that were associated with only the S3, S4, or S1-S2 loop from one subunit (68/200; -5.02) were also disregarded in favor of sites that bridged two or more subunits (74/200; -5.41). The way that BrMT affects currents suggests that it is inducing cooperativity, in that it causes normally independently-acting subunits to activate all at once, albeit more slowly than in unbound channels (Sack and Aldrich, 2006).

Of all the 200 binding modes, the pocket with the most favorable binding energy bridged two adjacent subunits (Figure 4-11). The binding residues included F302 and K388, which reside on the S4 and S6 helices of adjacent subunits, respectively. Looking at the alignment (Figure 4-5), the four BrMT-insensitive channels have a leucine in place of F302. K388 is no different in drk1, but is a glutamine in jShak1, which was the most BrMT-insensitive channel we tested. Therefore, we chose to make F302L and K388Q single and double mutants in mouse $K_v1.2$ and test them for BrMT sensitivity.

While the molecular cloning of the mutants was successful, injecting K388Q mRNA, as well as the F302L+K388Q double mutant mRNA, did not produce measurable currents in *X. laevis* oocytes (not shown). F302L channels, on the other hand, did express viable currents (Figure 4-12A). After exposure to 100 µM BrMT, F302L channels were blocked to levels 73% of control (Figure 4-12B), a statistically significant difference ($p = 0.009$). Activation kinetics were slowed by

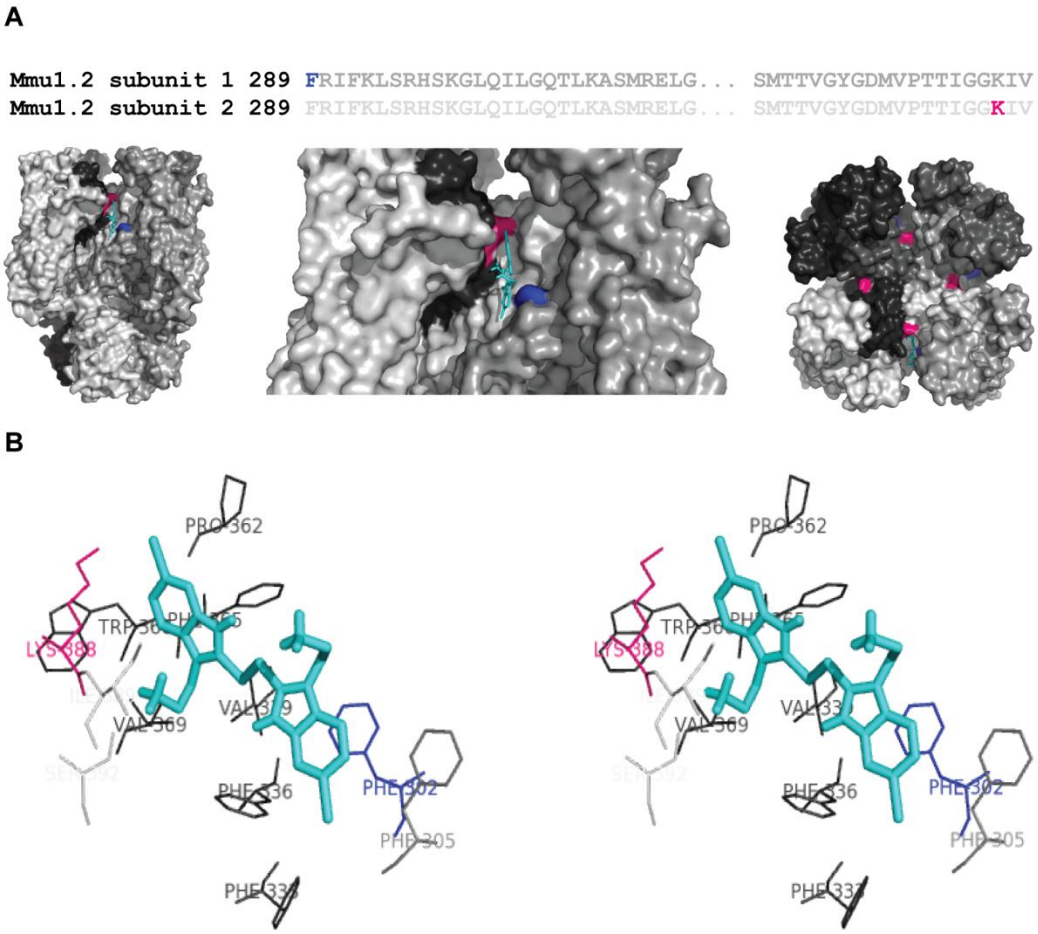

Figure 4-11. The most favorable BrMT binding site on a closed model of rat $K_v1.2$ as predicted through virtual docking. A, Phenylalanine at position 302 in one subunit (blue) creates a pocket with, among other residues, the lysine at position 388 (pink) in the adjacent subunit. This binding site is clearly at the face of two, likely three subunits (grey shades in 3-D surface models), and is accessible from the extracellular face (rightmost model). B, The ligand BrMT (cyan, sticks) is shown docked in the lowest energy position predicted after 200 runs of AutoDock Vina (Trott and Olson, 2010), using the Pathak et al. (2007) closed model of rat $K_v1.2$ as the target receptor. The binding pocket contains 8 other residues within 0.42 nm of bound BrMT (stereo image), which are shaded by subunit as in panel A. Residues are labeled according to rat/mouse $K_v1.2$ numbering. Images created in PyMOL.

a factor of 5.9 (Figure 4-12C), which was not significantly different than wild type (p = 0.103).

Discussion

The goal of this study was to identify specific amino acids in mouse K_v1.2 that interact with the gating modifier toxin BrMT. We hypothesized that one of three different sites were involved, the S3-S4 linker, the S308/G329 pocket, and the F302/K388 pocket, but our results did not decisively support these residues being involved in BrMT binding. However, several useful and interesting findings can still be drawn from the experimental data.

A Common Binding Site for BrMT on K_v1.1 Through 1.6

The mouse K_v1 subfamily of channels are highly conserved in sequence, and, presumably, also in structure. Assaying BrMT on this group of channels was an attempt to find one or more K_v1 channels that were not blocked by the toxin, an outcome which would have been advantageous in finding residues of interest through sequence comparison. However, micromolar concentrations of BrMT blocked each of mouse K_v1.1 through K_v1.6, suggesting that the site of action for this toxin resides in one of the many common structural elements of the K_v1 subfamily.

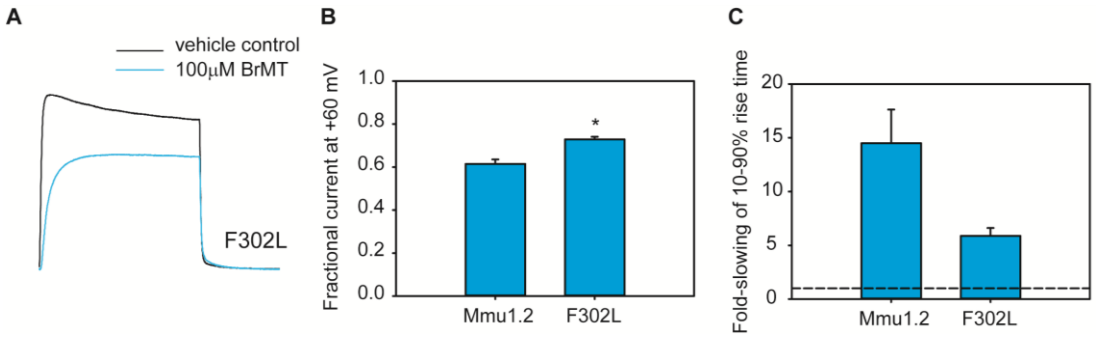

Figure 4-12. Mouse $K_v1.2$ F302L mutant channels are blocked by 100 µM BrMT. A, , Representative two-electrode voltage clamp traces for mouse $K_v1.2$ F302L in control solution (black lines) and after a 3 minute incubation with 100 µM BrMT (cyan lines). Cells were exposed to a range of stimulating voltages (from -80 to +80 mV in 10 mV steps) but only the sweep from +60 mV is shown. The depolarization phase lasted 100 ms. Control currents shown here is 16 µA at steady-state. B, The fractional current at the end of the depolarizing pulse for F302L channels after a 3 minute exposure to 100 µM BrMT. Wild type mouse $K_v1.2$ is shown for comparison. F302 was blocked about 10% less than mouse $K_v1.2$, and this difference was statistically significant ($p = 0.009$). C, Slowing of activation kinetics in F302 by 100 µM BrMT. Wild type mouse $K_v1.2$ is shown for comparison. The ratio of the 10-90% rise time in BrMT to that during the control trace was calculated for individual experiments and averaged. F302 was less affected in activation kinetics compared to $K_v1.2$ but this difference was not significant ($p = 0.103$). Dotted line represents a ratio of unity, i.e. no kinetic slowing. For panels B and C, bars are shown mean + s.e.m., with n values ranging from 3 to 6.

This pharmacological similarity between K_v1 members has been established (Gutman et al., 2005; Harmar et al., 2009), and has led to difficulties in finding or designing drugs that bind to only one K_v1 subtype. For example, $K_v1.3$ has been implicated in the effector memory T-cell activation involved in autoimmune disorders like multiple sclerosis (Rangaraju et al., 2009) and inflammatory skin disorders like psoriasis (Nguyen et al., 2010), but small molecule blockers of $K_v1.3$ often do not select between K_v1 subfamily members (Hanner et al., 1999; Schmitz et al., 2005). Therefore in retrospect, while the potential reward in performing this assay was great, it was not the most informative set of channels on which to test BrMT. Expanding the assay to channels far removed from mouse, in this case the cnidarian jShak1 and jShaw1 from *Polyorchis penicillatus*, greatly narrowed the number of candidate receptor residues.

BrMT Data Supports a Role Reversal for Cnidarian K_v1 and K_v3 Channels

The cnidarian K_v1 channel jShak1 was unaffected by BrMT while the conspecific K_v3 jShaw1 experienced the same amount of current reduction and kinetic slowing as mouse K_v1 targets. This observation supports earlier evidence of a functional role reversal from these two channels (Sand et al., 2011). In our characterization of jShaw1, we pointed out that the cnidarian K_v3 has qualities more aligned with vertebrate K_v1 channels - a negative V_{50} and fast opening kinetics - while jShak1 has a more positive V_{50} (Jegla et al., 1995) like those measured from the vertebrate K_v3 subfamily. The fact that BrMT binds to the K_v1-like jellyfish channel, then, suggests that this functional similarity between

jShaw1 and mammalian K_v1 channels is rooted in structural elements, and one of these common features contains the binding site for BrMT.

BrMT Interaction with F302 and K388 Cannot Be Ruled Out

Our results showed that changing the phenylalanine at position 302 in mouse $K_v1.2$ to leucine did not alter BrMT binding efficacy. This residue, along with K388, was in the most energetically favored binding site predicted by automated docking. The data for K388 was inconclusive. There are a few possible explanations for these results: 1) the mutation at position 302 was not severe enough to significantly diminish the binding pocket; 2) this was not the correct binding pocket and we performed too few or too poorly optimized docking runs; or 3) there were faults in the initial receptor and/or ligand models. We will address these sources of error in turn.

To address the first point, although the data on its face points to F302 not being in the receptor site, there are more definitive mutations we could have introduced at that position. The reason we changed F302 to a leucine was its presence in the channels that were not sensitive to BrMT, but phenylalanine residues take up ~190 cubic angstroms, and leucine ~167 cubic angstroms (Jena Library, IMB). Altering F302 to alanine would have reduced the volume to ~89 cubic angstroms, thereby confirming more strongly the role of this residue in BrMT binding. Changing K388 to residues other than glutamine may have also produced measurable current, thereby allowing a conclusive answer for that position. There is also prior evidence through the ILT mutant of Shaker that the uncharged

residues in S4 are responsible for the cooperative actions during activation. BrMT was shown to induce cooperativity early in the activation pathway of *D. melanogaster* ShakerB (Sack and Aldrich, 2006), and F302 aligns directly between the isoleucine and leucine of the ILT positions. Therefore, if BrMT did bind to F302 that could explain the characteristic inducing of cooperativity measured from channels treated with the toxin. However, the residues that align with I, L, and T would also make good targets for mutagenesis and automated docking in future efforts to localize the BrMT receptor site.

Secondly, it is almost certainly true that performing more randomly seeded docking runs would increase the quantity and quality of the predicted BrMT binding pockets. We manually performed 10 randomly seeded runs of 20 docking events each. This could easily be increased by orders of magnitude if the job submission and data collection were automated with the aid of python-based script, the language AutoDock Vina uses. Another way in which the runs could be optimized would be to reduce the search space on the receptor protein and run multiple randomly seeded runs on targeted areas. We searched essentially the whole channel, resulting in the prediction of many irrelevant, i.e. intracellular, binding sites.

Lastly, the target protein in this study was rat $K_v1.2$, which has an associated crystal structure (Long et al., 2005) and a more recent refinement of that structure (Chen et al., 2010). The channel in its crystallized form has an open pore, although there is some debate as to whether the voltage sensors are in the fully activated state or some post-activated, relaxed conformation (see Chapter 3 of this

thesis). Regardless, because of convincing previous evidence that this toxin binds to one or more of the channel closed states (Kelley et al., 2003; Sack and Aldrich, 2006; Sack et al., 2004), we could not use these crystal-based models of $K_v1.2$ as targets for BrMT virtual docking. Thus, we sought a closed model of the channel. This is, of course, not trivial, since much of the controversy surrounding the voltage sensing domain boils down to where the S4 helix resides in the closed conformation. Closed channels are essentially invisible to traditional electrophysiological assays that detect ionic current, and in most cases cannot be crystallized, i.e. many channels are open at 0 mV. To further knowledge on these unseen conformations, some have employed molecular dynamics (MD) simulations to visualize the transitions between the crystallized state and the fully deactivated, closed state (Pathak et al., 2007; Yarov-Yarovoy et al., 2006). We chose the Pathak et al. closed model for our docking experiments. In simulating the $K_v1.2$ channel they used the Yarov-Yarovoy model as the starting point, but also took into account fluorophore emission data from the Shaker channel voltage sensor.

The fact that the F302L mutation did not affect BrMT sensitivity could point to flaws in the Pathak et al. closed model of $K_v1.2$. The most obvious limitation of this model is the lack of inter-helical loop sequences. In the original 2A79 crystal structure, the naturally flexible loops were crystallized in many different conformations and were not resolved, being replaced instead by homopolymeric stretches of alanine (Long et al., 2005). The gating modifier hanatoxin is known to bind near the S3-S4 loop, so this area was of interest to us. The mutagenesis

data we reported here conclusively shows that residues A275 to A287 of the S3-S4 linker do not contain the binding site, but the residues that align exactly with the hanatoxin binding residues lie outside this region. Therefore we cannot definitely say that BrMT does not share a receptor site with hanatoxin (a simple co-inhibition experiment could not be performed as there were no known commercial sources of hanatoxin at the time these experiments were run). The fact that the Pathak closed model is based on data that was deficient in this region adds to the uncertainty about discounting this region as a binding area.

Conclusion

Despite the doubt surrounding the involvement of the S3-S4 linker, we believe that the true binding pocket of BrMT on K_v1 channels is one that actively adjoins two subunits, producing the cooperativity seen in previous published works (Sack and Aldrich, 2006) and matching the data presented here. The physical distance is too great for a BrMT dimer to join the S3-S4 linker to an adjacent subunit, and so any future efforts would focus on making a wider range of mutations at F302 and K388, as well as the other residues identified in that particular binding pocket (I389, S392, F305, F333, F336, P362, F365, W366). Another strategy could take into account the two BrMT functional groups capable of forming salt bridges; two positively charged amines would react with negatively charged amino acids in a stabilizing fashion. Locating an appropriate site on $K_v1.2$ with the right distance between negatively charged residues could narrow down the search space. On the computational side, given the limited knowledge about the structure of closed K_v channels, it may be that finding the BrMT binding site by sequence comparison

and more time consuming “alanine-scanning” mutagenesis (changing many consecutive residues to alanine) will shed some light on the unknown conformations of the deactivated S4 helix. Mapping which residues can bind to such a small molecule could serve as a molecular caliper between S4 and likely the S5 or S6 of an adjacent subunit, which would validate or refute existing models of $K_v1.2$ in the closed state and help constrain future models. Therefore, while we did not determine where BrMT binds on mouse $K_v1.2$ channels, we can exclude several sites with a fair amount of certainty, and use the knowledge gained from these experiments to narrow in on the correct receptor site.

Literature Cited

Aggarwal, S. K. and MacKinnon, R. (1996). Contribution of the S4 segment to gating charge in the Shaker K+ channel. *Neuron* **16**, 1169-1177.

Alabi, A. A., Bahamonde, M. I., Jung, H. J., Il Kim, J. and Swartz, K. J. (2007). Portability of paddle motif function and pharmacology in voltage sensors. *Nature* **450**, 370-U2.

Armstrong, C. M. (1966). Time course of TEA+-induced anomalous rectification in squid giant axons. *Journal of General Physiology* **50**, 491-503.

Armstrong, C. M. (1969). Inactivation of potassium conductance and related phenomena caused by quaternary ammonium ion injection in squid axons. *Journal of General Physiology* **54**, 553-575.

Armstrong, C. M. (1971). Interaction of tetraethylammonium ion derivatives with potassium channels of giant axons. *Journal of General Physiology* **58**, 413-437.

Armstrong, C. M. and Binstock, L. (1965). Anomalous rectification in squid giant axon injected with tetraethylammonium chloride. *Journal of General Physiology* **48**, 859-870.

Borjesson, S. I. and Elinder, F. (2011). An electrostatic potassium channel opener targeting the final voltage sensor transition. *Journal of General Physiology* **137**, 563-577.

Bryan, P. J., McClintock, J. B. and Hamann, M. (1997). Behavioral and chemical defenses of marine prosobranch gastropod Calliostoma canaliculatum in response to sympatric seastars. *Journal of Chemical Ecology* **23**, 645-658.

Catterall, W. A. (1987). Common modes of drug action on Na+ channels - local anesthetics, antiarrhythmics and anticonvulsants. *Trends in Pharmacological Sciences* **8**, 57-65.

Catterall, W. A. (2010). Ion channel voltage sensors: structure, function, and pathophysiology. *Neuron* **67**, 915-928.

Chen, J., Deng, M., He, Q., Meng, E., Jiang, L., Liao, Z., Rong, M. and Liang, S. (2008). Molecular diversity and evolution of cystine knot toxins of the tarantula Chilobrachys jingzhao. *Cellular and Molecular Life Sciences* **65**, 2431-2444.

Chen, X. R., Wang, Q. H., Ni, F. Y. and Ma, J. P. (2010). Structure of the full-length Shaker potassium channel Kv1.2 by normal-mode-based X-ray crystallographic refinement. *Proceedings of the National Academy of Sciences of the United States of America* **107**, 11352-11357.

Cuypers, E., Abdel-Mottaleb, Y., Kopljar, I., Rainier, J. D., Raes, A. L., Snyders, D. J. and Tytgat, J. (2008). Gambierol, a toxin produced by the dinoflagellate

Gambierdiscus toxicus, is a potent blocker of voltage-gated potassium channels. *Toxicon* **51**, 974-983.

Edgar, R. C. (2004). MUSCLE: multiple sequence alignment with high accuracy and high throughput. *Nucleic Acids Research* **32**, 1792-1797.

Ehrlich, J. R. and Nattel, S. (2009). Novel approaches for pharmacological management of atrial fbrillation. *Drugs* **69**, 757-774.

Gracy, J., Le-Nguyen, D., Gelly, J. C., Kaas, Q., Heitz, A. and Chiche, L. (2008). KNOTTIN: the knottin or inhibitor cystine knot scaffold in 2007. *Nucleic Acids Research* **36**, D314-D319.

Guiet-Bara, A., Durlach, J. and Bara, M. (2007). Magnesium ions and ionic channels: activation, inhibition or block - a hypothesis. *Magnesium Research* **20**, 100-106.

Gutman, G. A., Chandy, K. G., Grissmer, S., Lazdunski, M., McKinnon, D., Pardo, L. A., Robertson, G. A., Rudy, B., Sanguinetti, M. C., Stuhmer, W. et al. (2005). International Union of Pharmacology. LIII. Nomenclature and molecular relationships of voltage-gated potassium channels. *Pharmacological Reviews* **57**, 473-508.

Hall, T. A. (1999). BioEdit: a user-friendly biological sequence alignment editor and analysis program for Windows 95/98/NT, vol. 41, pp. 95-98. Nucleic Acids Symposium Series.

Hanner, M., Schmalhofer, W. A., Green, B., Bordallo, C., Liu, J., Slaughter, R. S., Kaczorowski, G. J. and Garcia, M. L. (1999). Binding of correolide to K(v)1 family potassium channels - Mapping the domains of high affinity interaction. *Journal of Biological Chemistry* **274**, 25237-25244.

Harmar, A., Hills, R., Rosser, E., Jones, M., Buneman, O., Dunbar, D., Greenhill, S., Hale, V., Sharman, J., Bonner, T. et al. (2009). IUPHAR-DB: the IUPHAR database of G protein-coupled receptors and ion channels. *Nucleic Acids Research* **37**, D680-D685.

Hille, B. (1977). Local anesthetics - hydrophilic and hydrophobic pathways for drug-receptor reaction. *Journal of General Physiology* **69**, 497-515.

Hille, B. (2001). Ion Channels of Excitable Membranes. Sunderland, MA, USA: Sinauer Associates, Inc.

Hodgkin, A. L. and Huxley, A. F. (1952). A quantitative description of membrane current and its application to conduction and excitation in nerve. *Journal of Physiology-London* **117**, 500-544.

Huang, Q. Q., Harvey, C. M., Paterson, A. R. P., Cass, C. E. and Young, J. D. (1993). Functional expression of Na(+)-dependent nucleoside transport systems of rat intestine in isolated oocytes of *Xenopus laevis*. Demonstration that rat

jejunum expresses the purine-selective system N1 (CIF) and a second, novel system N3 having broad specificity for purine and pyrimidine nucleosides. *Journal of Biological Chemistry* **268**, 20613-20619.

Jegla, T., Grigoriev, N., Gallin, W. J., Salkoff, L. and Spencer, A. N. (1995). Multiple Shaker potassium channels in a primitive metazoan. *Journal of Neuroscience* **15**, 7989-7999.

Jiang, Y. X., Ruta, V., Chen, J. Y., Lee, A. and MacKinnon, R. (2003). The principle of gating charge movement in a voltage-dependent K+ channel. *Nature* **423**, 42-48.

Kelley, W. P., Wolters, A. M., Sack, J. T., Jockusch, R. A., Jurchen, J. C., Williams, E. R., Sweedler, J. V. and Gilly, W. F. (2003). Characterization of a novel gastropod toxin (6-bromo-2-mercaptotryptamine) that inhibits shaker K channel activity. *Journal of Biological Chemistry* **278**, 34934-34942.

Kopljar, I., Labro, A. J., Cuypers, E., Johnson, H. W. B., Rainier, J. D., Tytgat, J. and Snyders, D. J. (2009). A polyether biotoxin binding site on the lipid-exposed face of the pore domain of K_v channels revealed by the marine toxin gambierol. *Proceedings of the National Academy of Sciences of the United States of America* **106**, 9896-9901.

Lange, W., Geissendorfer, J., Schenzer, A., Grotzinger, J., Seebohm, G., Friedrich, T. and Schwake, M. (2009). Refinement of the binding site and mode of action of the anticonvulsant retigabine on KCNQ K+ channels. *Molecular Pharmacology* **75**, 272-280.

Larsen, J., Gasser, K. and Hahin, R. (1996). An analysis of dimethylsulfoxide-induced action potential block: A comparative study of DMSO and other aliphatic water soluble solutes. *Toxicology and Applied Pharmacology* **140**, 296-314.

Lee, H. C., Wang, J. M. and Swartz, K. J. (2003). Interaction between extracellular hanatoxin and the resting conformation of the voltage-sensor paddle in K_v channels. *Neuron* **40**, 527-536.

Liao, Z., Yuan, C. H., Deng, M. C., Li, J., Chen, J. J., Yang, Y. J., Hu, W. J. and Liang, S. P. (2006). Solution structure and functional characterization of Jingzhaotoxin-XI: A novel gating modifier of both potassium and sodium channels. *Biochemistry* **45**, 15591-15600.

Long, S. B., Campbell, E. B. and MacKinnon, R. (2005). Crystal structure of a mammalian voltage-dependent Shaker family K+ channel. *Science* **309**, 897-903.

Mackinnon, R., Reinhart, P. H. and White, M. M. (1988). Charybdotoxin block of Shaker K+ channels suggests that different types of K+ channels share common structural features. *Neuron* **1**, 997-1001.

Mackinnon, R. and Yellen, G. (1990). Mutations affecting TEA blockade and ion permeation in voltage-activated K+ channels. *Science* **250**, 276-279.

Mouhat, S., Andreotti, N., Jouirou, B. and Sabatier, J. M. (2008). Animal toxins acting on voltage-gated potassium channels. *Current Pharmaceutical Design* **14**, 2503-2518.

Nguyen, W., Howard, B. L., Neale, D. S., Thompson, P. E., White, P. J., Wulff, H. and Manallack, D. T. (2010). Use of Kv1.3 blockers for inflammatory skin conditions. *Current Medicinal Chemistry* **17**, 2882-2896.

Pathak, M. M., Yarov-Yarovoy, V., Agarwal, G., Roux, B., Barth, P., Kohout, S., Tombola, F. and Isacoff, E. Y. (2007). Closing in on the resting state of the shaker K+ channel. *Neuron* **56**, 124-140.

Phillips, L. R., Milescu, M., Li-Smerin, Y. Y., Mindell, J. A., Kim, J. I. and Swartz, K. J. (2005). Voltage-sensor activation with a tarantula toxin as cargo. *Nature* **436**, 857-860.

Ragsdale, D. S., McPhee, J. C., Scheuer, T. and Catterall, W. A. (1994). Molecular determinants of state-dependent block of Na+ channels by local anesthetics. *Science* **265**, 1724-1728.

Rangaraju, S., Chi, V., Pennington, M. W. and Chandy, K. G. (2009). Kv1.3 potassium channels as a therapeutic target in multiple sclerosis. *Expert Opinion on Therapeutic Targets* **13**, 909-924.s

Sack, J. T. and Aldrich, R. W. (2006). Binding of a gating modifier toxin induces intersubunit cooperativity early in the Shaker K channel's activation pathway. *Journal of General Physiology* **128**, 119-132.

Sack, J. T., Aldrich, R. W. and Gilly, W. F. (2004). A gastropod toxin selectively slows early transitions in the Shaker K channel's activation pathway. *Journal of General Physiology* **123**, 685-696.

Sand, R. M., Atherton, D. M., Spencer, A. N. and Gallin, W. J. (2011). jShaw1, a low-threshold, fast-activating K(v)3 from the hydrozoan jellyfish Polyorchis penicillatus. *Journal of Experimental Biology* **214**, 3124-3137.

Sanguinetti, M. C., Johnson, J. H., Hammerland, L. G., Kelbaugh, P. R., Volkmann, R. A., Saccomano, N. A. and Mueller, A. L. (1997). Heteropodatoxins: Peptides isolated from spider venom that block Kv4.2 potassium channels. *Molecular Pharmacology* **51**, 491-498.

Schmitz, A., Sankaranarayanan, A., Azam, P., Schmidt-Lassen, K., Homerick, D., Hansel, W. and Wulff, H. (2005). Design of PAP-1, a selective small molecule Kv1.3 blocker, for the suppression of effector memory T cells in autoimmune diseases. *Molecular Pharmacology* **68**, 1254-1270.

Schrödinger, L. (2010). The PyMOL Molecular Graphics System, Version 1.3r1.

Schwab CH. (2010). Conformations and 3D pharmacophore searching. *Drug Discovery Today: Technologies* **7**:e245-e253.

Seoh, S. A., Sigg, D., Papazian, D. M. and Bezanilla, F. (1996). Voltage-sensing residues in the S2 and S4 segments of the Shaker K+ channel. *Neuron* **16**, 1159-1167.

Stampe, P., Kolmakovapartensky, L. and Miller, C. (1994). Intimations of K+ channel structure from a complete functional map of the molecular surface of charybdotoxin. *Biochemistry* **33**, 443-450.

Starmer, C. F., Grant, A. O. and Strauss, H. C. (1984). Mechanisms of use-dependent block of sodium channels in excitable membranes by local anesthetics. *Biophysical Journal* **46**, 15-27.

Swartz, K. J. (2004). Towards a structural view of gating in potassium channels. *Nature Reviews Neuroscience* **5**, 905-916.

Swartz, K. J. (2007). Tarantula toxins interacting with voltage sensors in potassium channels. *Toxicon* **49**, 213-230.

Swartz, K. J. and Mackinnon, R. (1995). An inhibitor of the Kv2.1 potassium channel isolated from the venom of a Chilean tarantula. *Neuron* **15**, 941-949.

Swartz, K. J. and MacKinnon, R. (1997a). Hanatoxin modifies the gating of a voltage-dependent K+ channel through multiple binding sites. *Neuron* **18**, 665-673.

Swartz, K. J. and MacKinnon, R. (1997b). Mapping the receptor site for hanatoxin, a gating modifier of voltage-dependent K+ channels. *Neuron* **18**, 675-682.

Tatulian, L., Delmas, P., Abogadie, F. C. and Brown, D. A. (2001). Activation of expressed KCNQ potassium currents and native neuronal M-type potassium currents by the anti-convulsant drug retigabine. *Journal of Neuroscience* **21**, 5535-5545.

Tombola, F., Pathak, M. M. and Isacoff, E. Y. (2006). How does voltage open an ion channel? *Annual Review of Cell and Developmental Biology* **22**, 23-52.

Trott, O. and Olson, A. J. (2010). Software news and update AutoDock Vina: Improving the speed and accuracy of docking with a new scoring function, efficient optimization, and multithreading. *Journal of Computational Chemistry* **31**, 455-461.

Tytgat, J., Chandy, K. G., Garcia, M. L., Gutman, G. A., Martin-Eauclaire, M. F., van der Walt, J. J. and Possani, L. D. (1999). A unified nomenclature for short-chain peptides isolated from scorpion venoms: alpha-KTx molecular subfamilies. *Trends in Pharmacological Sciences* **20**, 444-447.

Wolters, A. M., Jayawickrama, D. A. and Sweedler, J. V. (2005). Comparative analysis of a neurotoxin from *Calliostoma canaliculatum* by on-line capillary isotachophoresis/H-1 NMR and diffusion H-1 NMR. *Journal of Natural Products* **68**, 162-167.

Yang, Q. A., Fedida, D., Xu, H. J., Wang, B. H., Du, L. P., Wang, X. J., Li, M. Y. and You, Q. D. (2010). Structure-based virtual screening and electrophysiological evaluation of new chemotypes of Kv1.5 channel blockers. *ChemMedChem* **5**, 1353-1358.

Yarov-Yarovoy, V., Baker, D. and Catterall, W. A. (2006). Voltage sensor conformations in the open and closed states in ROSETTA structural models of K+ channels. *Proceedings of the National Academy of Sciences of the United States of America* **103**, 7292-7297.

Zarayskiy, V. V., Balasubramanian, G., Bondarenko, V. E. and Morales, M. J. (2005). Heteropoda toxin 2 is a gating modifier toxin specific for voltage-gated K+ channels of the Kv4 family. *Toxicon* **45**, 431-442.

Chapter 5: Conclusions and General Discussion

Capturing the dynamics of voltage-dependent gating in K_v channels is best accomplished through a variety of methods and approaches. In this thesis, the problem was tackled in three ways, each revealing new information about K_v channels.

First, by harnessing the natural variation of protein sequences in the animal kingdom, the K_v3 family was shown to be more functionally diverse than previously known. jShaw1, the first cnidarian K_v3 sequence to be published, grouped phylogenetically within the K_v3 subfamily but had activation properties more akin to a mammalian K_v1 channel, activating at more negative voltages than is typical with mammalian K_v3 channels and with more rapid kinetics. The unusually negative opening threshold of jShaw1 was the most interesting property, but unraveling the mechanism will require further study. In some models of K_v channel activation, the pore "wants" to be open, but is held closed by the deactivated voltage sensors. In this vein, the voltage sensors of jShaw1 do not "hold" the pore closed as effectively as other K_v3 channels. As mentioned in Chapter 2, the absolute number of charged residues in S4 alone does not determine the opening threshold or V_{50}. Having fewer charges in S4 would logically make the voltage sensors more resistant to activation as the increase in positive charge inside the cell would exert less repulsive force on the S4 helices. jShaw1 has fewer charges than the two mouse K_v3 channels, and activates more readily. Therefore, there must be another mechanism that makes the voltage sensors more primed to activate.

K_v channel activation can be broken down into two phases: the independent movement of the four voltage sensors (which can be measured as gating current), followed by the concerted opening of the entire channel pore (measured by ionic current). Testing these two phases separately (i.e. measuring the gating current) would shed light on the mechanism behind the negative threshold of jShaw1. Gating currents can be measured by expressing a version of the channel that does not conduct ionic current and depolarizing the cell. If the number of channels in the cell is known, the gating charge can also be derived. For macroscopic currents like those measured from oocytes, the limiting slope method (Almers, 1978) provides a reliable estimate of the gating charge. This is accomplished by plotting log G/G_{max} and finding the slope at the limit of the curve. This could be done for jShaw1 and the mouse K_v3 channels to see if a change in gating charge underlies the negative threshold of jShaw1. Another useful technique would be to attach fluorphores to the extracellular end of the S4 helix to look at the timing of voltage sensor activation compared to channel opening. Such voltage-clamp fluorimetry experiments would clarify whether the voltage sensor movements or the concerted channel opening step, or both, were happening at more negative voltages than mouse K_v3 channels.

Finally, data presented in Chapter 4 showed that jShaw1 was inhibited by BrMT, and displayed more K_v1-like behavior since BrMT typically acts on K_v1 and K_v4 channels. This interesting cnidarian channel will be useful in future comparative structure-function studies aimed at locating the BrMT binding site or other K_v1

blockers with undetermined modes of action, as it does not have a high sequence similarity to K_v1 channels.

Data presented in Chapter 3 showed that replacing 13 residues in the mouse $K_v1.2$ S3-S4 linker with four glycines or four serines made the open state very stable, and shifted the half-activation voltages more negative. Looking back at jShaw1 in light of this data (Figure 2-2), it can be seen that jShaw1 has a very short S3-S4 linker, about 4 or 5 amino acids compared to the mouse K_v3 channels which have around 10, and it has a V_{50} shifted approximately -20 mV. However, wild type mouse $K_v1.2$ has a relatively long linker and activates at a negative voltage, so clearly length is not the only determinant of voltage-dependent gating. A plethora of evidence was presented in Chapter 3 that would support that statement. For example, there are more negative charges in the mouse $K_v1.2$ linker than in the mouse K_v3 linkers, and given the result that negative glutamate loops de-stabilized the closed state, these extra negative charges could be contributing to the more hyperpolarized V_{50} of mouse $K_v1.2$ compared to mouse K_v3 channels.

The most generally applicable finding from the work presented in this thesis is that structural studies on membrane proteins must be complemented by functional evidence when looking at dynamic behaviors like voltage-dependent gating. Crystal structures of K_v channels, in addition to being generated in unnatural conditions, at best represent one frame among millions of possible conformations. Collecting functional data from channels embedded in membranes provides a way to test whether crystallographers are lucky enough to have captured the protein in a stable, native state. Using voltage clamp electrophysiology, mutagenesis, and

pharmacology, the problems associated with adding heavy fluorescent probes or cross-linking agents can be avoided as well.

The data presented in Chapter 3 supports the idea that the voltage sensors in the rat $K_v1.2$ crystal structure (Chen et al., 2010; Long et al., 2005) are not in the fully activated state. The best estimates of the relative movement between S3 and S4 produced through free energy comparisons suggest the two helices move substantially more apart than what is predicted by current open and closed state models. If the crystallized voltage sensors are not fully activated, but the pore is open, they could be in the postulated "relaxed" state, which occurs during long depolarization events (Haddad and Blunck, 2011; Villalba-Galea et al., 2008). Or, the crystallized voltage sensors could be closer to the resting conformation. However given the extremely low open probability for the pore with resting voltage sensors (Schoppa and Sigworth, 1998), this is unlikely – unless, of course, the conditions of crystallization are so severe they negate such functional evidence, which should not be discounted as a possibility.

The findings regarding the S3-S4 distance and the $K_v1.2$ crystal structure have implications on the data collected in Chapter 4. The gating modifier BrMT binds to closed channels, and so a model of the closed $K_v1.2$ (Pathak et al., 2007) was used for automated docking to identify potential binding sites. This closed model was based on the original rat $K_v1.2$ crystal structure (Long et al., 2005), so if this crystal structure is inaccurate, then the closed model will also be flawed. Searching for a BrMT binding site in this way is therefore necessarily limited to the quality of the most current closed models. A new consensus model for the

closed K_v1.2 channel was released very recently (Vargas et al., 2011), but the published coordinates consist only of the VSD helices. BrMT would be best docked onto a whole channel, but this new model could nonetheless be useful if the toxin binds to the S4 helix in any way. It would also be interesting to dock BrMT with the presumed "open" Kv1.2 crystal structures, and test the binding sites produced by those searches. If a receptor pocket was successfully located, it would point to the voltage sensors being in, or closer to, the resting conformation.

In conclusion, fully comprehending the ability of voltage sensors to respond to membrane potential is important for many reasons: to understand protein function, to appreciate channel dysfunction, to manipulate channels for medicinal gain, or to isolate and use voltage sensors in as building blocks in synthetic biological systems. Voltage-gated potassium channel proteins are the most practical platform on which to investigate the structure-function relationships that underlie this useful property. Methods like comparative analysis, site-directed mutagenesis and Gibbs free energy comparisons, and the use of pharmacological agents are straightforward and provide an examination of channels expressed in living cells, a vital functional correlate that should accompany any structural study on membrane proteins.

Literature Cited

Almers, W. (1978). Gating currents and charge movements in excitable membranes. *Reviews of Physiology, Biochemistry, and Pharmacology*. **82**, 96-190.

Chen, X. R., Wang, Q. H., Ni, F. Y. and Ma, J. P. (2010). Structure of the full-length Shaker potassium channel Kv1.2 by normal-mode-based X-ray crystallographic refinement. *Proceedings of the National Academy of Sciences of the United States of America* **107**, 11352-11357.

Haddad, G. A. and Blunck, R. (2011). Mode shift of the voltage sensors in Shaker K+ channels is caused by energetic coupling to the pore domain. *Journal of General Physiology* **137**, 455-472.

Long, S. B., Campbell, E. B. and MacKinnon, R. (2005). Crystal structure of a mammalian voltage-dependent Shaker family K+ channel. *Science* **309**, 897-903.

Pathak, M. M., Yarov-Yarovoy, V., Agarwal, G., Roux, B., Barth, P., Kohout, S., Tombola, F. and Isacoff, E. Y. (2007). Closing in on the resting state of the shaker K+ channel. *Neuron* **56**, 124-140.

Schoppa, N. E. and Sigworth, F. J. (1998). Activation of Shaker potassium channels I. Characterization of voltage-dependent transitions. *Journal of General Physiology* **111**, 271-294.

Villalba-Galea, C. A., Sandtner, W., Starace, D. M. and Bezanilla, F. (2008). S4-based voltage sensors have three major conformations. *Proceedings of the National Academy of Sciences of the United States of America* **105**, 17600-17607.

Vargas, E., Bezanilla, F., and Roux, B. (2011). In search of a consensus model of the resting state of a voltage-sensing domain. *Neuron* **72**, 713-720.